

**Analysis and numerical study of inertia-gravity waves
generated by convection in the tropics.**

by

Stephanie Evan

B.S., Reunion Island University, 2004

M.S., University Paul Sabatier Toulouse III, 2005

A thesis submitted to the
Faculty of the Graduate School of the
University of Colorado in partial fulfillment
of the requirements for the degree of
Doctor of Philosophy
Department of Atmospheric and Oceanic Sciences

2011

This thesis entitled:
Analysis and numerical study of inertia-gravity waves generated by convection in the tropics.
written by Stephanie Evan
has been approved for the Department of Atmospheric and Oceanic Sciences

Dr. M. Joan Alexander

Dr. John J. Cassano

Dr. Jimy Dudhia

Dr. David Noone

Dr. Cora Randall

Date _____

The final copy of this thesis has been examined by the signatories, and we find that both the content and the form meet acceptable presentation standards of scholarly work in the above mentioned discipline.

Evan, Stephanie (Ph.D., Atmospheric Sciences)

Analysis and numerical study of inertia-gravity waves generated by convection in the tropics.

Thesis directed by Dr. M. Joan Alexander

Gravity waves transport momentum and energy upward from the troposphere and by dissipation affect the large-scale structure of the middle atmosphere. An accurate representation of these waves in climate models is important for climate studies, but is still a challenge for most global and climate models. In the tropics, several studies have shown that mesoscale gravity waves and intermediate scale inertia-gravity waves play an important role in the dynamics of the upper atmosphere. Despite observational evidence for the importance of forcing of the tropical circulation by inertia-gravity waves, their exact properties and forcing of the tropical stratospheric circulation are not fully understood. In this thesis, properties of tropical inertia-gravity waves are investigated using radiosonde data from the 2006 Tropical Warm Pool International Cloud Experiment (TWP-ICE), the European Centre for Medium-Range Weather Forecasts (ECMWF) dataset and high-resolution numerical experiments.

Few studies have characterized inertia-gravity wave properties using radiosonde profiles collected on a campaign basis. We first examine the properties of intermediate-scale inertia-gravity waves observed during the 2006 TWP-ICE campaign in Australia. We show that the total vertical flux of horizontal momentum associated with the waves is of the same order of magnitude as previous observations of Kelvin waves. This constitutes evidence for the importance of the forcing of the tropical circulation by intermediate-scale inertia-gravity waves.

Then, we focus on the representation of inertia-gravity waves in analysis data. The wave event observed during TWP-ICE is also present in the ECMWF data. A comparison between the characteristics of the inertia-gravity wave derived with the ECMWF data to the properties of the wave derived with the radiosonde data shows that the ECMWF data capture similar structure for this wave event but with a larger vertical wavelength. The Weather Research and Forecasting

(WRF) modeling system is used to understand the representation of the wave event in the ECMWF data. The model is configured as a tropical channel with a high top at 1 hPa. WRF is used with the same horizontal resolution (~ 40 km) as the operational ECMWF in 2006 while using a finer vertical grid-spacing than ECMWF. Different experiments are performed to determine the sensitivity of the wave structure to cumulus schemes, initial conditions and vertical resolution. We demonstrate that high vertical resolution would be required for ECMWF to accurately resolve the vertical structure of inertia-gravity waves and their effect on the middle atmosphere circulation.

Lastly we perform WRF simulations in January 2006 and 2007 to assess gravity wave forcing of the tropical stratospheric circulation. In these simulations a large part of the gravity wave spectrum is explicitly simulated. The WRF model is able to reproduce the evolution of the mean tropical stratospheric zonal wind when compared to observational data and the ECMWF reanalysis. It is shown that gravity waves account for 60% up to 80% of the total wave forcing of the tropical stratospheric circulation. We also compute wave forcing associated with intermediate-scale inertia-gravity waves. In the WRF simulations this wave type represents $\sim 30\%$ of the total gravity wave forcing. This suggests that intermediate-scale inertia-gravity waves can play an important role in the tropical middle-atmospheric circulation. In addition, the WRF high-resolution simulations are used to provide some guidance for constraining gravity wave parameterizations in coarse-grid climate models.

Dedication

To Domi, Dani and Françoise.

Acknowledgements

First and foremost, I wish to express my sincere gratitude to my supervisor, Dr Joan Alexander, who has supported me throughout my thesis with her patience and knowledge while allowing me the room to work in my own way. I really appreciated her encouragement and effort and without her, this thesis would not have been completed.

I also wish to thank Dr Jimy Dudhia for his help and general advice on the WRF simulations. I am grateful to Orion Poplawski for his assistance with all types of technical problems. Thank you to Laurie Conway for her support with administrative issues.

A special acknowledgement goes to my office mate, Alison Grimsdell, for contributing to such a pleasant working environment.

Thank you to my friends in Boulder, especially Ding and Ludovic, for all the dinners, good times and road trips ! Thank you to my friends in France, for being my surrogate family while I was in Toulouse and for all the good memories. I also thank my parents for being supportive every step of my studies and my brothers, Frederic and Thomas, for keeping me grounded.

And last but not least, thank you to Jerome for his support during these past years and for all he means to me.

Contents

Chapter	
1	Introduction 1
1.1	Tropical waves and their effect on the stratospheric circulation. 2
1.2	Modeling studies of gravity waves. 5
1.3	Intermediate-scale inertia-gravity waves. 8
1.4	Thesis outline 10
2	Description of model and main methods 14
2.1	Model configuration and governing equations 15
2.2	Physical parameterizations 19
2.3	Wavelet analysis: S-Transform 21
2.4	FFT spectral analysis: Calculations of Eliassen-Palm vector 24
3	Intermediate-scale tropical inertia-gravity waves observed during the TWP-ICE campaign 27
3.1	Data and Meteorological conditions 28
3.2	Wave properties 33
3.2.1	Period 33
3.2.2	Vertical wavelength 37
3.2.3	Horizontal structure 38
3.3	Identification of Inertia-Gravity Waves 44
3.3.1	Quadrature spectrum 44

3.3.2	Intrinsic frequency and group propagation	45
3.3.3	Wave Energy	47
3.3.4	Momentum Flux	48
3.4	Summary and conclusions	51
4	Model study of intermediate-scale tropical inertia-gravity wave and comparison to TWP-ICE	
	campaign observations.	53
4.1	Wave analysis in ECMWF	55
4.1.1	Data	55
4.1.2	Wavelet Analysis.	56
4.1.3	Wave properties	58
4.2	Identification of the wave source	64
4.3	Wave analysis in the WRF simulations	70
4.3.1	Model and experiments	70
4.3.2	Model validation	71
4.3.3	Wave structure in WRF	77
4.4	Discussion	83
4.5	Summary and conclusions	88
5	WRF simulations of gravity waves in opposite QBO phases	90
5.1	Model and data description	92
5.2	Mean state	93
5.3	Precipitation characteristics	96
5.4	Wave response	100
5.5	Wave forcing of the QBO.	106
5.5.1	Zonal wind evolution	106
5.5.2	Upwelling	109
5.5.3	TEM momentum equation budget	113

5.6	Spatial characteristics of gravity waves	116
5.7	Summary and Discussion	119
6	Summary and Conclusions	123
6.1	Tropical inertia-gravity wave properties and their representation in numerical models	124
6.2	Gravity wave forcing of the QBO	126
6.3	Perspectives	127
	Bibliography	129

Tables

Table

3.1	Radiosonde profile statistics.	29
3.2	Phase differences between Mount Bundy and other sites. Mount Bundy is taken as the reference site.	40
3.3	Phase differences between Point Stuart and other sites. Point Stuart is taken as the reference site	40
3.4	Apparent wavelengths between the different pairs of sites (G: Garden Point, C: Cape Don, P: Point Stuart, M: Mount Bundy)	41
3.5	Directions of horizontal propagation (degrees from East) estimated with different combinations of sites.	41
3.6	Density of Kinetic (KE) and Potential Energy (PE) averaged between 22 and 27km for all of the sites.	48
3.7	Total momentum flux $\overline{u'_h w'}$ and zonal momentum flux $\overline{u' w'}$ ($\times 10^{-3} \text{ m}^2 \text{ s}^{-2}$) averaged between 20 and 28km	51
4.1	Properties of the wave event derived from the ECMWF fields of zonal and meridional winds at 20 hPa. Also shown are the characteristics of the wave derived from the radiosondes for comparison.	62

4.2	Mean wave characteristics from the ray tracing analysis for the altitude range 10-15 km. The values correspond to rays with initial angle of propagation of -45° . The wave direction α is expressed in degrees from the West-East direction. The phase speeds and horizontal background wind are in the direction of the wave propagation.	70
4.3	Configuration and parameterizations used in WRF experiments.	71
4.4	Mean horizontal wavelength and direction of propagation in the WRF simulations. .	81
5.1	The cumulus (BMJ) and microphysics (MP) schemes mean (mm hr^{-1}) and variance ($\text{mm}^2 \text{hr}^{-2}$) of tropical precipitation (10°S - 10°N).	98
5.2	Precipitation variability ($\text{mm}^2 \text{hr}^{-2}$) in the WRF simulations. The values correspond to the TRMM and WRF total variance of precipitation, precipitation associated with the BMJ cumulus scheme and the microphysics (MP) for the frequency ranges $\omega < 1$ cpd (low-frequency), $\omega = 1$ cpd (diurnal) and $\omega > 1$ cpd (high-frequency).	99
5.3	$F^{(z)}$ (mPa) at 65 and 100 hPa for 2006 and 2007	105
5.4	Mean tropical upwelling $\overline{w^*}$ (mm s^{-1}) averaged over 10°S - 10°N	111
5.5	Mean acceleration terms $\partial\overline{u}/\partial t$ ($\text{m s}^{-1} \text{day}^{-1}$) and $-\overline{w^*}\partial\overline{u}/\partial z$ ($\text{m s}^{-1} \text{day}^{-1}$) for the height-range 23-32 km.	113
5.6	Peak accelerations ($\text{m s}^{-1} \text{day}^{-1}$) associated with different gravity wave types for the height range 25-28 km.	119

Figures

Figure

- | | | |
|-----|---|----|
| 1.1 | Time-height section of monthly mean zonal wind at Singapore 2000-2011. Westerly winds are shaded, contour interval is 10 m s^{-1} . The data are obtained from http://www.geo.fu-berlin.de/en/met/ag/strat/produkte/qbo/index.html | 4 |
| 2.1 | WRF tropical channel model domain. | 17 |
| 2.2 | Example of S-transform cosine (black solid line) and sine (red dashed line) wavelet pair with period of 5 days. | 22 |
| 2.3 | (a) A time series consisting of a sinusoid with a period of 2 days for the first part, a period of 4 days for the middle of the signal and a period of 1 day for the last part of the signal. (b) Time-frequency spectrum of the synthetic time series. | 23 |
| 3.1 | Location of the radiosonde sites used in the study. | 28 |
| 3.2 | Latitude-height cross section of zonal wind averaged over January-February 2006 at the longitude of Darwin (130.89°) (from NCEP/DOE 2 Reanalysis data provided by the NOAA/OAR/ESRL PSD, Boulder, Colorado, USA, http://www.cdc.noaa.gov/). The contour interval is 4 m s^{-1} . Negative values are dotted. The crosses indicate the latitudes of the different radiosonde sites. | 30 |
| 3.3 | Mean vertical profiles of zonal wind (U), meridional wind (V), temperature (T) and buoyancy frequency squared (N^2) averaged over the TWP-ICE campaign period. Each line represents a different site. | 30 |

3.4	Sequence of daily average (average over UTC times) infrared brightness temperature (from TRMM global-merged data set) from 20 January to 31 January 2006. On January 19 Tropical Cyclone Daryl can be observed at 18°S, 116°E. On January 23 a Mesoscale Convective System developed south of Darwin (around 11°S, 128°E).	32
3.5	Time-height series of unfiltered perturbations of (a) Temperature (T_p), (b) zonal wind (U_p), (c) meridional wind (V_p) observed at Point Stuart.	34
3.6	Time-frequency spectrum averaged between 22 and 26km for the perturbations of (a) temperature, (b) zonal wind and (c) meridional wind observed at Point Stuart.	35
3.7	Time-height series showing the perturbations of (a) temperature (T_p), (b) zonal wind (U_p), (c) meridional wind (V_p) observed in the 1.7-3 day range at Point Stuart.	36
3.8	Vertical profiles of phase differences and coherences of u' for a period of 2.5 days at (a) Garden Point, (b) Cape Don, (c) Point Stuart, (d) Mount Bundy. The reference level is 23km.	37
3.9	Vertical profiles of phase differences for time series of zonal wind between (a) Mount Bundy and Garden Point, (b) Mount Bundy and Cape Don, (c) Mount Bundy and Point Stuart.	39
3.10	Schematic showing angles between sites (see text for explanations).	42
3.11	Distribution of directions of horizontal propagation derived from velocity and temperature perturbations. The distribution includes angles for Garden Point, Mount Bundy, Point Stuart and Cape Don.	43
3.12	Vertical profile of quadrature spectrum of zonal and meridional wind perturbations observed at Garden Point. Positive quadrature in solid and negative quadrature in dots.	44
3.13	Vertical profile of time scale for radiative damping for a vertical wavelength of 6km.	46
3.14	Vertical profiles of the momentum fluxes for waves of 1.5-2.5 day period for all of the sites. (a) Angle of propagation of -74° and (b) angle of propagation of -47.3°	50

4.1	Time-frequency spectrum averaged between 30 and 20 hPa for the ECMWF perturbations of (a) temperature, (b) zonal wind and (c) meridional wind observed at 12.5°S,132.5°E.	56
4.2	(a) Distribution of horizontal wavelengths derived from the zonal wind perturbations. (b) Distribution of horizontal wavelengths derived from the meridional wind perturbations. (c) Distribution of directions of horizontal propagation derived from the zonal wind perturbations. (d) Distribution of directions of horizontal propagation derived from the meridional wind perturbations.	61
4.3	Squared amplitude ($\text{m}^2 \text{s}^{-2}$) of the wave observed in the 1.7-3 day range inferred from the quadrature spectrum of meridional and zonal wind perturbations.	61
4.4	Longitude-height series showing the eastward propagating perturbations of (a) temperature, (b) zonal wind and (c) meridional wind observed in the 1.7-3 day range and in the 4-7 planetary wavenumber range. The perturbations are averaged over the latitudes 5-15°S and shown on 02/01/2006 at 18UTC.	63
4.5	(a) Daily average infrared ($11\mu\text{m}$) brightness temperature from MTSAT-1R. Average from 01/18 to 01/27. Areas colder than 253 K correspond to deep convection (Inoue et al., 2008). (b) Final locations of back trajectories in longitude-latitude cross sections for the height range 10-15 km. The red symbols correspond to rays with initial angle of propagation of -45° . and the blue symbols are for initial angle of propagation of -74°	67
4.6	Wave parameters obtained from the ray tracing calculations for $\lambda_h = 6500 \text{ km}$, $\alpha_0 = -74^\circ$: (a) Ray trajectory (b) Intrinsic frequency (black) and absolute value of the Coriolis parameter (red), (c) Intrinsic zonal group velocity (black), zonal wind (blue) and ground-based zonal group velocity (red), (d) Intrinsic meridional group velocity (black), meridional wind (blue) and ground-based meridional group velocity (red), (e) Vertical wavelength, (f) Vertical group velocity.	68
4.7	Same as Fig. 6., except for $\lambda_h = 6500 \text{ km}$, $\alpha_0 = -45^\circ$	69

4.8	Comparison of simulated (right) versus GPCP and ECMWF (left) daily mean rainfall (mm/day) from 18 January to 28 January 2006.	72
4.9	Taylor diagram of daily mean precipitation. Each dot represents a 10-day average from 01/18 to 01/28. The position of each dot represents the correlation between observations (GPCP) and model (WRF, ECMWF). The standard deviation of the simulated rainfall is proportional to the radial distance from the origin. The green contours indicate the root-mean-square difference between the simulated and observed rainfall.	73
4.10	Latitude-pressure cross section of zonal wind averaged over 18 January-6 February 2006.	75
4.11	Vertical profile of buoyancy frequency averaged over 15°S-15°N and 18 January-6 February. WRF (red), ECMWF (black).	76
4.12	Time-frequency spectrum averaged between 22 and 26 km for the WRF perturbations of (a) temperature, (b) zonal wind and (c) meridional wind in the simulation beginning 01/18. The amplitudes correspond also to an average value over the region 120-140°E and 5-15°S.	78
4.13	Squared amplitude of the 2-day wave inferred from the quadrature spectrum of meridional and zonal wind perturbations averaged between 30 and 20 hPa. (a) ECMWF, (b) WRF simulation beginning 01/18, (c) 01/20, (d) 01/22, (e) 01/24, (f) 01/26. The amplitudes correspond to an average value over 28 January to 6 February.	80
4.14	Vertical profiles of phase differences and coherences for u for a period of 2.5days for the simulation initialized January 18 with a grid spacing of 500 m (left), the simulation initialized January 26 with a grid spacing of 500 m (middle) and the simulation initialized January 18 with ECMWF vertical resolution (left).	82

4.15	(a) Time-height sections of heating rate from the BMJ cumulus scheme for the period of wave generation (01/18 to 01/28). The heating rate is averaged over the region 100-140°E and 10°S-5°N. (b) Vertical profile of zonal wind averaged over the region 100-140°E and 10°S-5°N and 18 January-28 January.	84
4.16	Time-longitude section of (a) TRMM and (b) WRF18 3-hourly precipitation rates averaged from 10°S to 5°N.	87
5.1	Time-height cross section of zonal wind averaged over 10°S-10°N from October 2005 to March 2007. The dashed lines delimit the two simulation periods.	94
5.2	Mean vertical profiles of zonal wind (u), temperature (T) and buoyancy frequency squared (N^2) averaged over the tropics (10°S-10°N). The red curves correspond to ERA-I and the black curves to WRF.	95
5.3	Distribution of hourly precipitation (mm hr^{-1}) averaged over the two simulation periods. The TRMM observations are shown on the top panel, the model values are on the bottom panel.	97
5.4	Zonal Wavenumber-frequency spectra of TRMM and WRF precipitation variance ($\text{mm}^2 \text{hr}^{-2}$) averaged from 10°S to 10°N. The red lines correspond to phase speed of 10 m s^{-1}	98
5.5	Zonal wavenumber-frequency spectra of $ F^{(z)} $ ($\log_{10} \text{ Pa}$) averaged from 10°S to 10°N. The distributions correspond to 2006 (left) and 2007 (right) at 100hPa (top), 65hPa (middle) and 20hPa (bottom).	102
5.6	Vertical component of the EP flux $ F^{(z)} $ (Pa) as a function of frequency at 65 hPa for 2006 (red) and 2007 (blue).	104
5.7	Evolution of WRF and ERA-I zonal mean zonal wind for the two simulation periods. The black curves indicate zonal wind vertical profiles at the beginning of the simulation, the blue profiles correspond to the middle of the simulation and the red curves to the end of the simulation.	108

- 5.8 Monthly zonal wind profiles from daily radiosonde measurements at Singapore (103.98°E, 1.36°N) in 2006 (left) and 2007 (right). The black curves indicate monthly mean values for January and the red curves correspond to monthly means for February. . . . 109
- 5.9 Vertical profiles of $\overline{w^*}$ averaged from 10°S to 10°N for the 2006 (left) and 2007 (right) simulations periods. The WRF estimates are shown in red and the ERA-I profiles are in black. 111
- 5.10 Vertical profiles of the zonal wind tendency (dashed black), the EP Flux divergence from low-frequency (green) and gravity waves (red), forcing due to the residual circulation (blue) and sum of EP Flux divergence and forcing due to the residual circulation (black). The forcing terms are averaged from 10°S to 10°N and over the two simulation periods. 114
- 5.11 Vertical profiles of EP flux divergence associated with different gravity wave types.
 (a) 2006 total acceleration due to gravity waves (red), gravity waves with $\lambda_x \geq 1000$ km (blue) and gravity waves with $\lambda_x < 1000$ km (green). (b) Same profiles as (a) but for waves with $\lambda_z < 10$ km. (c) 2007 total acceleration due to gravity waves (red), gravity waves with $\lambda_x \geq 1000$ km (blue) and gravity waves with $\lambda_x < 1000$ km (green). (d) Same profiles as (c) but for waves with $\lambda_z < 10$ km. 117

Chapter 1

Introduction

In the atmosphere, disturbances to a balanced state can result in excitation of gravity waves with a variety of spatial and temporal scales. When the effect of Earth's rotation (i.e. the Coriolis force) is included, these waves are also referred to as inertia-gravity waves. Atmospheric gravity waves can be forced by flow over topography, frontogenesis, jet stream activity and convection. Gravity waves transport momentum and energy upward from the troposphere and by dissipation, affect the large-scale structure of the middle atmosphere.

Gravity waves are an important mechanism of the climate system. They affect the middle atmospheric mean winds and temperatures, and thus, influence the stratospheric ozone photochemistry in the polar regions. In the tropics, gravity waves also have an impact on the formation of cirrus clouds which have an impact on the stratospheric dehydration (Jensen and Pfister, 2004). In addition, gravity waves play a key role in the tropical stratospheric circulation. The dominant variability in the tropical lower stratosphere is the Quasi-Biennial Oscillation (QBO). The QBO is an oscillation of the stratospheric zonal winds with an average period of 27 months. The phenomenon is forced by equatorial and convectively-generated gravity waves. The QBO affects the meridional circulation and temperature over a wide latitude range. It also influences the transport and chemistry of gases such as ozone or water vapor (Baldwin et al., 2001). Chemistry Climate Models (CCMs) or Global Climate Models (GCMs) which do not have a realistic QBO, may have significant biases in their representation of the stratospheric chemical composition. These models' deficiencies can reduce their ability to represent the present and future tropospheric climate via

dynamic or radiative links. Therefore an accurate representation of the QBO in CCMs is essential for climate studies. However the majority of current GCMs and CCMs fail to represent the QBO as they do not have an accurate representation of gravity wave effects in the tropics. This is in part because model grid resolution is insufficient to explicitly resolve gravity waves. In addition, most GCMs/CCMs have deficiencies in the representation of convective processes which are the gravity wave sources in the tropics. Capturing convectively-generated gravity wave effects remains a challenge for most GCMs/CCMs and this is an area of active current research.

Convectively-generated gravity waves in the tropics have horizontal wavelengths ranging from kilometers to thousands of kilometers, and periods ranging from minutes to the inertial period corresponding to $\frac{2\pi}{f}$, where f is the Coriolis parameter. The inertial period varies from ~ 1 day at 30° to ~ 6 days at 5° . The work presented in this thesis focuses primarily on intermediate-scale inertia-gravity waves which correspond to waves with horizontal wavelengths order of 1000-10,000 km and periods ranging from ~ 12 hours to 3 days. A good understanding of their morphology and forcing mechanisms is important to improve their representation in GCMs/CCMs. This chapter will review some important notions on tropical wave motions and their effects on the middle atmospheric circulation. Section 1.1 will discuss some characteristics of tropical waves and the tropical stratospheric circulation. Section 1.2 will present our current understanding of gravity waves from numerical studies. In Section 1.3 the properties of intermediate-scale inertia-gravity waves inferred from observational data are presented. Finally, Section 1.4 highlights the important questions that this thesis will consider.

1.1 Tropical waves and their effect on the stratospheric circulation.

In the tropics, wave motions develop primarily in response to latent heat release by convection. The characteristics of these waves are strongly influenced by the spatial and temporal evolution of the convective heating sources and the background flow. These waves correspond to planetary scale waves such as Kelvin, Rossby-Gravity and equatorial Rossby waves, the intermediate scale inertia-gravity waves and the small-scale gravity waves.

Kelvin waves correspond to large-scale wave motions which propagate along the equator toward the east. They can be observed with different periodicities ranging from 6 days to 20 days. They were first observed in the equatorial stratosphere by Wallace and Gutzwiller (1968).

The equatorial Rossby waves are westward propagating low frequency waves. They have a small group vertical velocity and thus can be subject to strong dissipation which limits their propagation into the stratosphere.

Mixed Rossby-gravity waves were first observed by Yanai and Maruyama (1966) and were characterized as westward propagating waves with periods of 4-5 days, vertical wavelength order of 4-8 km and a horizontal wavelength corresponding to zonal wavenumber 4.

Convection in the tropics generates gravity waves associated with a broad spectrum of phase speeds, horizontal and vertical wavelengths. The small-scale gravity waves usually correspond to high-frequency waves while the intermediate-scale gravity waves correspond to low frequency waves.

The waves described here, with the exception of the equatorial Rossby waves, provide the main forcing of the tropical middle atmospheric circulation.

The dominant wind regimes in the tropical middle atmosphere are the Quasi-Biennial Oscillation (QBO) in the stratosphere and the Semiannual Oscillation (SAO) in the upper stratosphere and mesosphere. The QBO is an oscillation of downward propagating easterlies and westerlies with an average period of about 27 months. The SAO corresponds to periodic oscillations of the zonal winds with a period of 6 months.

The QBO is shown on Figure 1.1 which is a time-height section of monthly mean zonal wind at Singapore (103.98°E, 1.36°N). On this plot we can see alternating easterly and westerly wind regimes propagating downward with time. The easterlies are generally stronger than the westerlies. The westerlies usually move down faster than the easterlies (Naujokat, 1986). The QBO is caused by an interaction between vertically propagating convectively generated waves emanating from the troposphere and the mean flow. This process is referred to as the wave-mean flow interaction in which the background flow acts as a filter on the vertical propagation of the waves and in return the momentum deposition from the waves can accelerate or decelerate the mean flow.

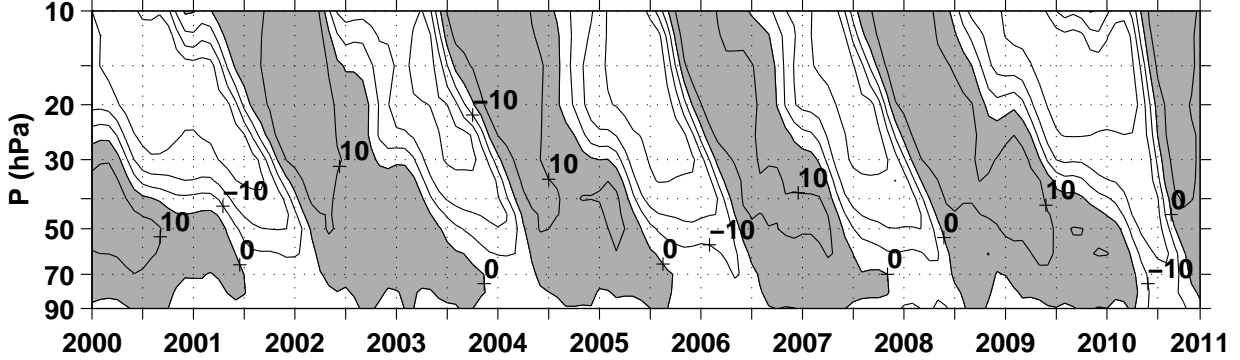


Figure 1.1: Time-height section of monthly mean zonal wind at Singapore 2000-2011. Westerly winds are shaded, contour interval is 10 m s^{-1} . The data are obtained from <http://www.geo.fu-berlin.de/en/met/ag/strat/produkte/qbo/index.html>.

The SAO is caused by the wave-mean flow interaction and by the mean advection of momentum by the meridional circulation (Garcia et al., 1997). The SAO and QBO have an influence on the meridional circulation and the temperature in the tropics and thus influence the transport and photochemistry of trace gases such as ozone (Baldwin et al., 2001). The QBO can also affect the distribution of water vapor.

The phase of the QBO determines which waves propagate through the stratosphere. Tropical waves can only propagate vertically through certain background conditions. The interaction of the waves with the mean flow depends on the wave phase velocity. The waves can only exist in regions where $c \neq \bar{u}(z)$, where c is the wave ground-based phase speed and $\bar{u}(z)$ is the horizontal wind at height z in the wave direction of propagation. The height at which $c = \bar{u}(z)$ corresponds to the wave critical level. As a wave approaches its critical level, its vertical wavelength and group velocity will become small and the wave will become more susceptible to dissipation. When the wave dissipates, it causes a deceleration or acceleration of the background zonal wind depending on the wave propagation direction.

In the first conceptual model of the QBO proposed by Lindzen and Holton (1968), the QBO is driven by vertically propagating gravity waves interacting with the mean flow. Holton and Lindzen (1972) then suggested that vertically-propagating Kelvin waves are responsible for forcing the westerly phase of the QBO while mixed Rossby-gravity waves drive the easterly phase of the QBO.

The mean tropical ascent of the Brewer-Dobson circulation acts to reduce the downward propagation of the QBO winds. According to observational studies, Kelvin and mixed Rossby-gravity wave amplitudes are too weak to provide sufficient momentum flux to compensate the effect of the mean tropical ascent on the QBO. Therefore additional momentum flux from intermediate-scale inertia-gravity waves and small-scale gravity waves is necessary to drive the QBO with its observed period. This was first demonstrated by Dunkerton (1997).

The potential of gravity waves for driving the QBO was demonstrated by Sato and Dunkerton (1997). They estimated momentum fluxes associated with gravity waves with periods between 1 and 3 days using radiosonde data from Singapore over 10 years. They estimated that momentum fluxes associated with gravity-waves are 5 to 10 times larger than those of Kelvin waves.

Convectively-generated gravity waves have been the subject of several observational studies. However observations in the tropics are too scarce to cover the broad gravity wave spectrum. Thus numerical studies have also been used to understand gravity wave excitation, propagation and impacts on the middle atmosphere. In the subsequent section, we present the main results of these studies.

1.2 Modeling studies of gravity waves.

Modeling studies of gravity waves generated by convection have used a variety of approaches:

- Idealized/analytical approaches (Holton et al., 2002; Beres et al., 2002; Beres, 2004; Grimsdell et al., 2010).
- 2-D or 3-D Cloud-resolving models (Fovell et al., 1992; Alexander et al., 1995; Alexander

and Holton, 1997; Piani et al., 2000).

- Numerical weather prediction models (Kim et al., 2009; Kuester et al., 2008).
- Atmospheric global climate models/coupled atmosphere-ocean climate models (Sato et al., 1999; Kawatani et al., 2010a).

Cloud-resolving and numerical weather prediction models are traditionally run with a fine horizontal grid-spacing to have an explicit representation of convective processes. These models are used on a limited area to investigate wave generation mechanisms and characteristics of gravity-waves above the convective sources. Cloud-resolving models indicate that deep convection generates small-scale and high-frequency gravity waves that can play an important role in driving the QBO. Using a two-dimensional cloud-resolving model, Alexander and Holton (1997) estimated that small-scale gravity waves could provide 25% of the QBO forcing.

Convection involves vertical motions and thermal forcing associated with latent heat release that can interact with overlying stably stratified layers to produce gravity waves. Modeling studies of convectively-generated gravity waves have indicated three main generation mechanisms.

The first one corresponds to the pure thermal forcing. In the absence of strong shear, deep convective heating profiles tend to force gravity waves with vertical wavelength approximately twice the depth of the heating above the source region (Salby and Garcia, 1987; Holton et al., 2002; Alexander et al., 1995).

Gravity waves can also be generated by the "obstacle effect" mechanism. In this mechanism convective clouds act as a barrier to the background flow and generates waves via a mechanism that resembles mountain wave formation. This mechanism favors wave propagation opposite to the background wind relative to the convective source (Pfister et al., 1993; Beres, 2004). This mechanism also predicts the wave to be approximately stationary relative to the source if the source varies on a slow timescale.

Finally, strong convective updrafts in convective storms can displace the isentropes of a stable layer above clouds and can generate gravity waves with a frequency specified by the frequency of

the convective updrafts (Fovell et al., 1992; Lane et al., 2001). This mechanism corresponds to the mechanical oscillator effect.

Results of these different studies indicate that the spectral characteristics of convectively generated waves are strongly influenced by the properties of latent heating within convection and the wind shear in the source region.

GCMs with a horizontal grid-spacing less than 100 km can reproduce much of the gravity wave spectrum. From GCM studies, it was also shown that an accurate representation of convectively-generated gravity wave effects on the QBO requires that models have a high vertical resolution in the tropics (Takahashi and Boville, 1992; Giorgetta et al., 2002). These studies indicated that a vertical spacing of 750 m or less is necessary to resolve the wave-mean flow interaction. This is because the critical layers in which the wave-mean flow interaction occurs have a small vertical scale and because short vertical wavelength waves need to be resolved. The QBO can be realistically simulated in high-resolution GCMs (Hamilton et al., 1999, 2001; Kawatani et al., 2010a). High-resolution GCMs are efficient tools to obtain a complete representation of tropical waves and to assess their role in the driving of the middle atmospheric circulation. However they are computationally expensive and can only be run for a few years.

In contrast, CCMs are run for hundreds of years and cannot afford to have a high resolution. Their typical grid cells are of the order of 100 km horizontally, and they do not resolve the excitation, propagation, and dissipation of small-scale gravity waves. Therefore CCMs account for the effects of the unresolved gravity waves with a physical parameterization. Parameterizations of convectively-generated waves specify the wave spectral characteristics at the source level. These usually correspond to wave horizontal wavelengths, propagation directions and wave momentum fluxes as a function of phase speed. This "launch spectrum" is specified from the model resolved fields. The "launch spectrum" is then altered as the waves propagate upward and encounter changing winds, temperatures and dissipative effects. McLandress and Scinocca (2005) have shown that a GCM's response is largely insensitive to the details of the dissipation mechanisms and that proper specification of the source spectrum spectral characteristics is more important. In GCMs/CCMs,

parameterizations of convectively-generated waves will also depend on how the models represent cloud and convective processes. CCMs which have realistic parameterizations of convective processes and gravity wave effects can simulate the QBO (Scaife et al., 2000; Giorgetta et al., 2002; Shibata and Deushi, 2005).

Numerical studies have indicated that accurate simulation of the QBO in GCMs requires a wave spectrum of planetary scale Kelvin and Rossby-Gravity waves, intermediate scale inertia-gravity waves and small-scale gravity waves. Many numerical studies have focussed on large-scale and small-scale waves while the intermediate-scale inertia-gravity waves have received less attention. Numerical studies have primarily investigated the generation mechanisms of small-scale and high-frequency gravity waves. Similar approaches should be explored in order to determine forcing mechanisms of intermediate-scale inertia-gravity waves. The following section describes the properties of this wave type inferred from observations.

1.3 Intermediate-scale inertia-gravity waves.

Tropical intermediate-scale Inertia-Gravity Waves (IGW) have intrinsic frequencies $\hat{\omega}$ which are comparable to the Coriolis parameter f . IGW have a large horizontal-velocity signature and thus have been commonly studied with radiosonde measurements of horizontal winds.

A pioneering study of equatorial IGW was made by Cadet and Teitelbaum (1979). On the basis of radiosondes collected over the Atlantic Ocean, they revealed IGW with a period of 35 h, a zonal wavelength of 2400 km and a vertical wavelength of 5 km. The waves showed a westward and upward propagation during the easterly shear phase of the QBO.

Similarly, during the Tropical Ocean Global Atmosphere Coupled Ocean Atmosphere Response Experiment (TOGA-COARE), Wada et al. (1999) conducted a study of equatorial IGW over the Western Pacific while the QBO was in the westerly shear phase. 2-day disturbances were observed in the lower stratosphere with vertical wavelengths of 3 to 5 km and horizontal wavelengths of several to ten thousand kilometers. The waves propagated eastward in the stratospheric westerlies.

Recently, Ratnam et al. (2006) have shown evidence for IGW in the upper troposphere and lower stratosphere regions over Indonesia using Coupling Processes in the Equatorial Atmosphere (CPEA) campaign radiosonde data. The dominant gravity waves observed had a period of 2 to 3 days, a vertical wavelength of 3 to 5 km and a horizontal wavelength of 1700 km with a southeastward propagation. At that time the QBO was in the westerly shear phase.

These studies indicate that IGW with short vertical wavelengths are more likely to be observed in radiosonde data. This is because radiosonde observations in the stratosphere are mainly available for the height-range $\sim 20\text{-}30$ km. Thus IGW with vertical wavelengths longer than about 10 km will not be observable in radiosonde data.

IGW observed in radiosonde data with horizontal wavelengths $\sim 1000\text{-}10,000$ km and periods $\sim 1\text{-}3$ days are likely to play a role in the QBO forcing. For example, with a ground-based frequency ω corresponding to a period of 2 days and a zonal wavelength of 5000 km, the magnitude of the ground-based phase speed $|c| = |\omega/k|$ is equal to 29 m s^{-1} . In the lower stratosphere, the QBO zonal wind varies from around -35 m s^{-1} to around 20 m s^{-1} (Naujokat, 1986). Therefore the intermediate-scale IGW observed in radiosonde data can be subject to strong dissipation as they propagate through the QBO winds.

Sato and Dunkerton (1997) estimated momentum fluxes associated with 1- to 3-day period waves using twice-daily radiosonde data at Singapore. Waves with periods between 1 and 3 days would correspond to IGW. The momentum flux associated with IGW was $20\text{-}60 \times 10^{-3} \text{ m}^2 \text{ s}^{-2}$ during the westerly shear phase of the QBO and $10\text{-}30 \times 10^{-3} \text{ m}^2 \text{ s}^{-2}$ during the easterly shear phase of the QBO. These values are in agreement with the calculations of Dunkerton (1997) who estimated that gravity-wave fluxes in the range $10\text{-}30 \times 10^{-3} \text{ m}^2 \text{ s}^{-2}$ are required for a realistic QBO when the effect of the tropical upwelling is taken into account. Sato and Dunkerton also showed that IGW have significant momentum flux compared with Kelvin and Rossby-gravity waves.

It is difficult to confirm the importance of intermediate-scale waves for the middle atmospheric circulation because of the lack of global, synoptic data. Radiosonde observations provide only local estimate of the momentum flux associated with IGW while a global distribution of the momentum

flux is of interest for the driving of the middle-atmospheric circulation.

Additional information on intermediate-scale IGW could be obtained from satellite data. However because of satellite sampling, estimates of momentum flux associated with IGW would be restricted to zonal wavenumbers up to 7.

Therefore modeling studies are still needed to understand the morphology of intermediate-scale IGW and their possible role in the middle atmospheric circulation.

Sassi and Garcia (1997) investigated the role of equatorial waves forced by convection in the SAO by means of numerical simulations with a three-dimensional quasi-nonlinear equatorial β -plane model. Results of their simulations suggest that the forcing in the upper stratosphere is predominantly due to planetary-scale Kelvin waves. However they demonstrated that in the mesosphere the SAO can be driven mainly by intermediate-scale Kelvin and inertia-gravity waves (zonal wavenumber $k=4-15$) and that the contribution from Kelvin waves (zonal wavenumber $k=1-3$) is negligible. Sassi and Garcia also investigated the role of diurnal convective forcing in intermediate-scale wave excitation. In their numerical experiments, the removal of the diurnal cycle of convection resulted in weaker excitation of intermediate-scale IGW. Results of their study suggest that diurnal forcing can be important for the generation of intermediate-scale IGW.

However few observational studies have focussed on intermediate-scale IGW generation mechanisms. The primary difficulty in understanding IGW forcing is that low-frequency waves can travel far from their sources. As a result, it can be hard to establish a correlation between stratospheric IGW and their tropospheric convective sources in observational data. A modeling approach may be more suitable to determine IGW sources.

1.4 Thesis outline

It is widely accepted that a broad spectrum of waves is needed to drive the middle atmospheric circulation. A complete understanding of these waves is important for an accurate representation of the QBO and SAO in GCMs/CCMs. Equatorial waves, such as Kelvin or Mixed Rossby-gravity waves and small-scale gravity-waves have been extensively studied. While these studies have im-

proved our knowledge of the generation mechanisms of these waves and their contribution to the QBO forcing, the relative role of inertia-gravity waves in the stratospheric circulation is just starting to emerge. Despite observational evidence for the importance of forcing of the tropical circulation by inertia-gravity waves, their exact properties and forcing of the tropical stratospheric circulation are not fully known. In order to increase our understanding of these waves this thesis will consider three main questions:

- What are the inertia-gravity wave properties from observations ?

Until recently the horizontal resolution of GCMs/CCMs was too low to have an accurate representation of these waves. However some current GCMs have sufficient horizontal resolution to resolve intermediate-scale inertia-gravity waves. A climatology of intermediate-scale wave parameters determined from measurements is essential to validate the representation of this wave type in high resolution models. Few studies have characterized inertia-gravity wave properties using radiosonde profiles collected on a campaign basis. In chapter 3 we use high-resolution soundings of horizontal wind and temperature taken during the 2006 Tropical Warm Pool International Cloud Experiment (TWP-ICE) to study 2-day stratospheric inertia-gravity waves which were observed during the campaign.

- What is required for numerical models to have an accurate representation of inertia-gravity waves ?

As stated in the previous sections, most GCMs do not have an accurate representation of tropical waves. This is in part because model grid resolution is insufficient and also because the models do not have an accurate representation of convective processes which are the wave sources in the tropics.

Unlike GCMs, mesoscale and cloud-resolving models can have a better representation of convection and tropical waves because of their finer grid-spacing. However these models are usually restricted to limited horizontal domains and are run for short time periods (\sim days). This prevents an interaction between small scale and large scale processes. Some

mesoscale models can be configured as tropical channel models, i.e., they are global in the zonal direction but bounded in the meridional direction. This type of model configuration is a good compromise between a mesoscale and global model and allows an influence of midlatitude processes on the tropics. In chapter 4 we use high resolution mesoscale model runs with varying initial conditions to assess the influence of cumulus schemes, initial conditions and vertical resolution on model representation of convectively generated inertia-gravity waves. The model used is the Weather Research Forecasting (WRF) mesoscale model. WRF is a flexible modeling framework that can be configured as a limited area model or a global model. This model has been extensively used both as a weather forecast tool and as a regional climate model. In order to simulate convectively-generated inertia-gravity waves we developed a tropical channel version of WRF with top above 1 hPa (WRF is usually used with a model top below 10 hPa). General properties of this model are described in chapter 2. The 2-day wave event described in Chapter 3 is used to evaluate the tropical channel model ability to resolve gravity waves in the tropics. The 2-day wave event is also present in the European Centre for Medium-Range Weather Forecasts (ECMWF) data with a horizontal resolution comparable to that of the WRF tropical channel model. In Chapter 3 we also present a comparison of the 2-day wave properties inferred from ECMWF with the wave properties inferred from the WRF simulations. This comparison helps to understand the representation of intermediate-scale inertia-gravity waves in reanalysis data.

- Which gravity waves contribute to the QBO forcing ?

With growing computer power, many GCMs will have better horizontal and vertical resolution. As a result a larger part of the gravity wave spectrum will be explicitly simulated. This raises the question of which portion of the gravity wave spectrum should be explicitly resolved and which part should be parameterized in these models. We propose to address this question by using the WRF tropical channel model. In Chapter 5, we use WRF to study gravity waves under opposite QBO phases. This is a new way to ad-

dress the QBO problem which combines GCM and numerical weather prediction model approaches. We compute gravity wave forcing for two periods corresponding to opposite QBO phases but similar regimes of convection. The WRF high-resolution simulations are used to provide some guidance for constraining gravity wave parameterizations in coarse-grid GCMs/CCMs. The model results are also used to quantify the QBO forcing due to intermediate-scale inertia-gravity waves.

Chapter 2

Description of model and main methods

The mesoscale model used in this thesis corresponds to the Weather Research Forecast (WRF) model developed by the National Center for Atmospheric Research. WRF is typically applied over limited area domains. Here we used a WRF tropical channel model with a high top (i.e., pressure at the top of the model ≤ 1 hPa). This model configuration alleviates issues with reflection of tropical waves that could result from imposing east/west boundaries.

As stated in Chapter 1, an accurate representation of gravity waves and their effects in the tropics requires a high vertical resolution. The model vertical grid-spacing is the same in all numerical experiments and corresponds to 500 m from 5 km to ~ 30 km.

The model results are analyzed using a wavelet technique analysis and Fast Fourier Transform (FFT) spectral analysis. The wavelet technique is similar to the one used in Chapter 3 to analyse the radiosonde data from TWP-ICE experiment. Numerous methods are used in this thesis but in this chapter, we only describe the techniques which require a detailed explanation. Other methods and term definitions will be presented in the subsequent chapters as we use them.

This chapter begins by describing the model configuration and governing equations in section 2.1. Then section 2.2 deals with the physical parameterizations used in the numerical experiments. Section 2.3 presents the wavelet technique analysis and finally, the FFT spectral analysis is described in section 2.4.

2.1 Model configuration and governing equations

The flux-form nonhydrostatic Euler equations in Cartesian space are used in the WRF model. The equations are formulated using a terrain-following vertical coordinate η which is defined as:

$$\eta = \frac{p_h - p_t}{p_s - p_t}$$

Where p_s and p_t are the pressures at the surface and top of the model respectively and p_h is the hydrostatic component of the pressure p . η varies from 1 at the surface to 0 at the top of the model. A complete description of the model equations is provided in Skamarock et al. (2005) and we provide here a short summary of WRF governing equations.

The model coupled variables are defined as:

$$\mathbf{V} = (U, V, W) = \mu_d(u, v, w) \quad (2.1)$$

$$\Omega = \mu_d \frac{\partial \eta}{\partial t} \quad (2.2)$$

$$\Theta = \mu_d \theta \quad (2.3)$$

$$Q_m = \mu_d q_m \quad (2.4)$$

Where \mathbf{V} is the coupled wind vector and u, v, w correspond to the horizontal and vertical winds. μ_d is the mass of the dry air in the column. Ω is the coupled contravariant vertical velocity. Θ represents the coupled potential temperature and θ is the potential temperature. q_m corresponds to the mixing ratio of the different hydrometeors resolved in the model (e.g. water vapor, cloud, rain, ice). The flux-form Euler equations correspond to:

The momentum equations:

$$\frac{\partial U}{\partial t} + \frac{\partial(Uu)}{\partial x} + \frac{\partial(Vu)}{\partial y} + \frac{\partial(\Omega u)}{\partial \eta} + \mu_d \alpha \frac{\partial p}{\partial x} + \frac{\alpha}{\alpha_d} \frac{\partial p}{\partial \eta} \frac{\partial \phi}{\partial x} = F_U \quad (2.5)$$

$$\frac{\partial V}{\partial t} + \frac{\partial(Uv)}{\partial x} + \frac{\partial(Vv)}{\partial y} + \frac{\partial(\Omega v)}{\partial \eta} + \mu_d \alpha \frac{\partial p}{\partial y} + \frac{\alpha}{\alpha_d} \frac{\partial p}{\partial \eta} \frac{\partial \phi}{\partial y} = F_V \quad (2.6)$$

$$\frac{\partial W}{\partial t} + \frac{\partial(Uw)}{\partial x} + \frac{\partial(Vw)}{\partial y} + \frac{\partial(\Omega w)}{\partial \eta} + g(\mu_d - \frac{\alpha}{\alpha_d} \frac{\partial p}{\partial \eta}) = F_W \quad (2.7)$$

The thermodynamic equation:

$$\frac{\partial \Theta}{\partial t} + \frac{\partial(U\theta)}{\partial x} + \frac{\partial(V\theta)}{\partial y} + \frac{\partial(\Omega\theta)}{\partial \eta} = F_{\Theta} \quad (2.8)$$

The mass-continuity equation:

$$\frac{\partial \mu_d}{\partial t} + \frac{\partial U}{\partial x} + \frac{\partial V}{\partial y} + \frac{\partial \Omega}{\partial \eta} = 0 \quad (2.9)$$

The conservation of water:

$$\frac{\partial Q_m}{\partial t} + \frac{\partial(Uq_m)}{\partial x} + \frac{\partial(Vq_m)}{\partial y} + \frac{\partial(\Omega q_m)}{\partial \eta} = F_{Q_m} \quad (2.10)$$

The hydrostatic equation:

$$\frac{\partial \phi}{\partial \eta} = -\mu_d \alpha_d \quad (2.11)$$

In these equations α_d represents the inverse density of dry air, α is the inverse of the full air density, ϕ is the geopotential and F_U , F_V , F_W , F_{Θ} , F_{Q_m} represent the forcing terms associated with WRF physical parameterizations, turbulent mixing and the Coriolis force.

To solve the flux-form Euler equations, the model variables are further partitioned between reference state variables and perturbations from the reference state. This reference state is hydrostatically-balanced. The reference state variables are a function of height (η) only and satisfy the model equations for an atmosphere at rest.

WRF uses high-order discretization schemes for time and space. A third-order Runge-Kutta scheme is used for the time integration. For all numerical experiments described in this thesis the time-step is equal to 45 s. The model uses a sixth order scheme for the advection terms.

Figure 2.1 shows the model domain. The latitudinal boundaries are located at $\pm 42^\circ$ and the horizontal grid-spacing is equal to 37 km. The number of grid points in Cartesian coordinates is 1081 (west-east) by 270 (south-north). The boundary conditions are periodic in the west-east direction. At the northern and southern boundaries the model is relaxed towards the ECMWF analyses. The relaxation zone corresponds to the model five outermost rows.

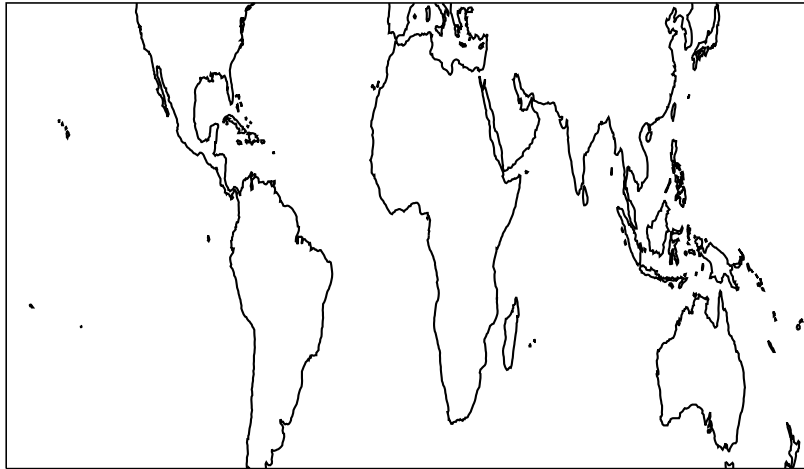


Figure 2.1: WRF tropical channel model domain.

We used 84 vertical levels in the model with the highest resolution ($\sim 20\text{-}100$ m) in the boundary layer, a vertical grid-spacing of 500 m between 5 km and 30 km and a coarse vertical grid-spacing (~ 2 km) in the upper stratosphere. The model top is fixed at 1 hPa in the first series of WRF experiments (Chapter 4) and 0.1 hPa for the WRF experiments focussing on inertia-gravity wave effects on the QBO (Chapter 5).

One specificity of the WRF tropical channel model used in this thesis is that the model top is higher than the default model top at 50 hPa. WRF is traditionally used for tropospheric studies and few WRF studies have focussed on stratospheric gravity waves in the tropics. The default model top can be modified by the model user. We initially did some tests with a model top at 5 hPa which causes anomalous values of geopotential height and vertical interpolation errors in the initialization program. This was related to the way the reference temperature state was defined in WRF version 3.0.1.1 (released in August 2008). In version 3.0.1.1, the base state temperature was computed as:

$$T = T_0 + A \ln \frac{\overline{p_d}}{p_0}$$

Where $T_0 = 300$ K is the reference sea level temperature, $p_0 = 10^5$ Pa is the reference sea level pressure and $A = 50$ K is the temperature difference between p_0 and p_0/e . With this definition

the temperature is decreasing linearly with log-pressure which is a valid approximation for the troposphere. However with the model top pressure lower than 5 hPa, stratospheric temperatures were unrealistically cold. As the reference state geopotential was defined using the reference state pressure and temperature, the cold stratospheric temperatures resulted in unrealistic values of reference geopotential height. The definition of the reference state temperature was modified in WRF version 3.1 (released in April 2009). Using this model version we were able to produce realistic stratospheric temperature distributions. WRF version 3.1 is the model version used for all simulations presented in this thesis. An issue was also found for the microphysics scheme for a model top pressure lower than 5 hPa. The low-pressure problem was related to the computation of the saturated water vapor mixing ratio. At low pressure the saturated water vapor pressure e_s can exceed the pressure p . When q_s is computed, it has $p - e_s$ in the denominator. In the upper stratosphere the formula for q_s breaks down and makes the denominator negative. As a result q_s gets set to a small value causing saturation and spurious clouds in the upper part of the model. This was fixed by introducing a minimum value for $p - e_s$ for low pressure cases. This minimum value prevents the production of clouds in the upper stratosphere but does not affect cloud formation elsewhere.

To avoid reflections near the model top, a sponge layer is included. In this region an implicit Rayleigh Damping is applied for the vertical velocity (Klemp et al., 2008). The vertical structure of the damping layer is defined as:

$$\tau(z) = \gamma_r \sin^2 \left[\frac{\pi}{2} \left(1 - \frac{z_{top} - z}{z_d} \right) \right] \text{ for } z \geq (z_{top} - z_d)$$

where γ_r is a damping coefficient equal to 0.4 s^{-1} in our simulations, z_{top} is the height of the model top and z_d is the depth of the damping layer (from the model top). In our numerical experiments z_d is equal to 15 km for a model top at 1 hPa and 20 km for a model top at 0.1 hPa.

2.2 Physical parameterizations

The WRF physics package includes microphysics, cumulus parameterization, planetary boundary layer (PBL), land surface models (LSM), longwave and shortwave radiation (Skamarock et al., 2005).

The PBL scheme and land surface model that we use are suitable for real case simulations. The PBL scheme is the Mellor-Yamada-Janjic (MYJ) scheme (Janjic, 2002) and the land surface model corresponds to the Noah LSM (Chen and Dudhia, 2001). The Noah LSM scheme provides sensible and latent heat fluxes to the PBL scheme.

The longwave and shortwave radiation schemes correspond to the Rapid Radiative Transfer Model for GCMs (Mlawer et al., 1997) and the Goddard shortwave scheme (Chou and Suarez, 1994). Detailed calculations of radiative fluxes involve a spectral integration (over molecular absorption lines), a vertical integration, and a directional integration. The spectral integration is time consuming and thus calculations of radiative fluxes can take a lot of computing time. In our WRF simulations the radiative schemes are called every 60 min for efficiency. The RRTMG scheme uses pre-set tables to calculate efficiently and accurately longwave fluxes and heating for application to GCMs. We chose the Goddard shortwave scheme as it has several climatological profiles for ozone. It has a tropical ozone profile that is appropriate to represent shortwave ozone effects in the tropical stratosphere.

In Chapter 4 we conduct numerical experiments using two cumulus schemes. The first one corresponds to the Kain-Fritsch cumulus scheme (Kain and Fritsch, 1990). The Kain-Fritsch convective parameterization utilizes a simple cloud model with moist updrafts and downdrafts that includes the effects of detrainment and entrainment. This scheme has been designed for grid sizes of ~ 25 km. In the scheme the onset of convection depends on the large-scale vertical velocity. The trigger criterion is applied above the PBL and thus the scheme can be sensitive to forcings provided by the PBL scheme. The Kain-Fritsch distinguishes deep and shallow convection depending on the cloud depth. The closure assumption used by the scheme is based on convective available potential

energy (CAPE). The scheme rearranges mass in the column using the simple cloud model until at least 90% of the CAPE is removed.

The second cumulus scheme used is the Betts-Miller-Janjic scheme (Janjic, 1994, 2000) which is derived from the Betts-Miller scheme (Betts, 1986; Betts and Miller, 1986). This scheme is a convective adjustment scheme that includes both deep and shallow convection. The BMJ scheme simulates the effects of deep convection by relaxing temperature and water vapor profiles to empirically based quasi-equilibrium thermodynamic profiles. The basic shape of these quasi-equilibrium thermodynamic profiles is based on observations from tropical field experiments (e.g., the Global Atmospheric Research Program Atlantic Tropical Experiment in 1974). The scheme starts by searching for the cloud base and cloud top. Then shallow or deep convection is activated depending on the cloud depth. If the cloud depth exceeds 200 hPa the scheme assumes that there is deep convection. The reference thermodynamic profiles are distinct for deep and shallow convection. When shallow convection is triggered, no precipitation is produced and the scheme redistributes heat and moisture in the column to satisfy enthalpy conservation. When deep convection is activated no liquid water is stored in the column, and all liquid water produced by condensation precipitates. The convective adjustment time scale used by this scheme is equal to 40 min in the WRF model. Differences in model results using the two schemes will be presented in Chapter 4.

In the simulations presented in Chapter 5, we use the WRF Single Moment 5-class (WSM5) microphysics scheme to represent cloud processes. This scheme predicts the mixing ratios of cloud water, rain, ice, snow and water vapor. A description of the scheme is provided in Hong et al. (2004). We chose this scheme as it is simple enough that it does not require a lot of computation time. The scheme allows supercooled water to exist and a gradual melting of snow as it falls below the melting layer. More complex microphysics schemes which include different types of frozen hydrometeors (e.g. graupel, hail) or predict the number concentration of the different hydrometeors are much more computationally expensive. With a grid-size of 37 km, the added expense of these schemes is not worthwhile as the model may not resolve strong updrafts that are important for dense frozen hydrometeors formation.

2.3 Wavelet analysis: S-Transform

In Chapters 3 and 4 we use a wavelet-type analysis technique to infer inertia-gravity wave properties.

A wavelet is a mathematical function used to divide a given function or continuous-time signal into different frequency components and study each component with a resolution that matches its scale. A wavelet transform is the representation of a function by wavelets. Wavelets are well-suited for analyzing functions that have discontinuities and sharp peaks, and for accurately deconstructing and reconstructing finite, non-periodic or non-stationary signals. Wavelet analysis provides a time-frequency representation of a time-series and gives the principal modes present in a signal and the variability of these modes.

Here the S-Transform is used to analyse time series of perturbations associated with gravity waves. The S-Transform (Stockwell et al., 1996) is a continuous wavelet transform analysis whose wavelet functions consist of sinusoidal functions modulated by a Gaussian (Figure 2.2). The S-Transform of a function h is given by:

$$H(f) = \int_{-\infty}^{+\infty} h(t) \frac{|f|}{\sqrt{2\pi}} e^{\frac{(\tau-t)^2 f^2}{2}} e^{-i2\pi f t} dt \quad (2.12)$$

The width of the Gaussian window is proportional to the inverse of the frequency f . During the analysis, only the Gaussian window is translated in time (t), keeping a constant phase reference, and providing absolute phase information of the signal. Figure 2.3 shows a synthetic time series consisting of a sinusoid with different periods and its time-frequency spectrum. We can see that the S-Transform can capture the three different modes of the signal as well as their location in time.

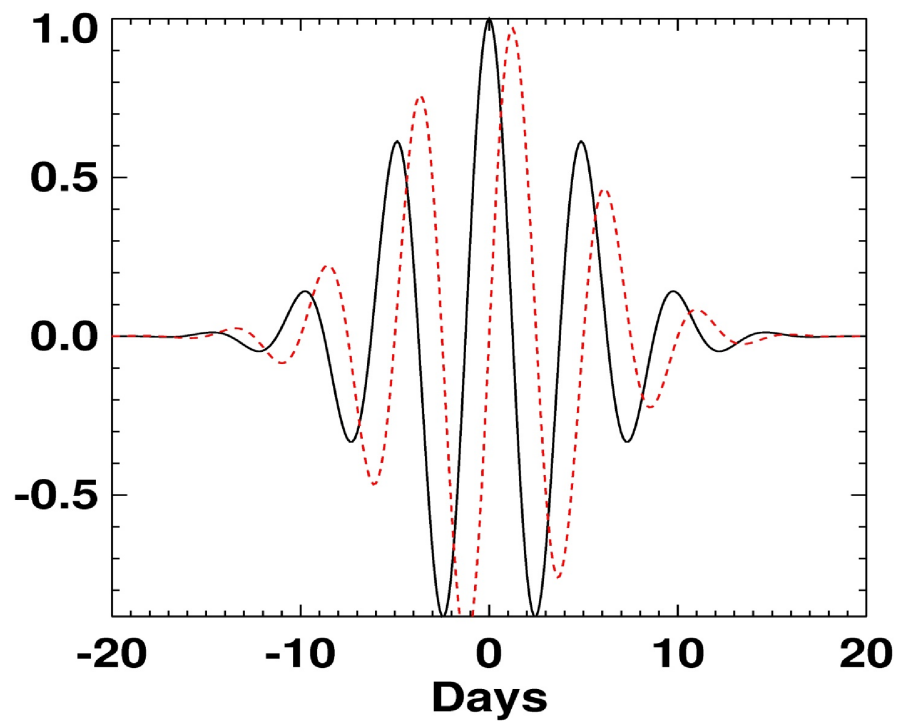


Figure 2.2: Example of S-transform cosine (black solid line) and sine (red dashed line) wavelet pair with period of 5 days.

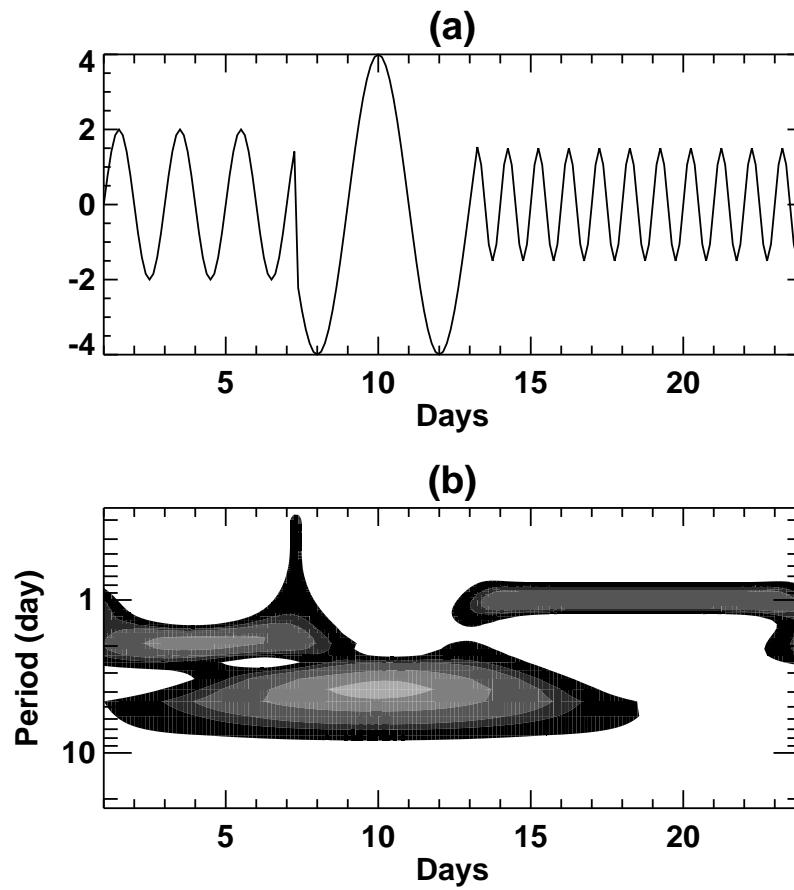


Figure 2.3: (a) A time series consisting of a sinusoid with a period of 2 days for the first part, a period of 4 days for the middle of the signal and a period of 1 day for the last part of the signal. (b) Time-frequency spectrum of the synthetic time series.

Furthermore the S-Transform provides an accurate tool to estimate the phase lag between two time series $f_1(t)$ and $f_2(t)$ by means of the cross S-Transform which is defined as:

$$CrossST(t, f) = S_{f_1}(t, f) \{S_{f_2}(t, f)\}^* \quad (2.13)$$

where $\{S_{f_2}(t, f)\}^*$ is the complex conjugate of $S_{f_2}(t, f)$. From the cross-spectrum we can define the phase and covariance amplitude spectrum as :

$$\Phi(t, f) = \arctan \left[\frac{\Im(CrossST(t, f))}{\Re(CrossST(t, f))} \right] \quad (2.14)$$

where $\Im(CrossST(t, f))$ and $\Re(CrossST(t, f))$ are the imaginary part and real part of the cross S-Transform respectively.

$$Cov(t, f) = |CrossST(t, f)| \quad (2.15)$$

The maximum of the covariance amplitude spectrum provides the amplitude and the frequency of the perturbation present in both signals. The phase at the frequency where the covariance is significant corresponds to the phase shift between the two time series.

Previous studies have used the S-Transform for wave analysis. Wang et al. (2006) derived properties of small-scale gravity waves in wind and temperature measurements during the CRYSTAL-FACE campaign. More recently, Alexander et al. (2008) provided global estimates of gravity wave momentum flux from High Resolution Dynamics Limb Sounder (HIRDLS) observations.

2.4 FFT spectral analysis: Calculations of Eliassen-Palm vector

In Chapter 5, FFT spectral analysis is used to analyze the wave response in the simulations. In particular, the Eliassen-Palm (EP) vector $\mathbf{F} = (F^{(\phi)}, F^{(z)})$ is used to diagnose the wave activity. Further discussion and interpretation of \mathbf{F} will be provided in Chapter 5 and in this section we only describe the calculations of \mathbf{F} . Additional details of EP vector calculations can also be found in Horinouchi et al. (2003) and Kawatani et al. (2010a).

Following Andrews et al. (1987), we express the Eliassen-Palm vector as:

$$F^{(\phi)} = \rho_0 a \cos \phi \left(\overline{u_z} \frac{\overline{v'\theta'}}{\theta_z} - \overline{u'v'} \right) \quad (2.16)$$

$$F^{(z)} = \rho_0 a \cos \phi \left\{ [f - (a \cos \phi)^{-1} (\overline{u \cos \phi})_\phi] \frac{\overline{v'\theta'}}{\theta_z} - \overline{u'w'} \right\} \quad (2.17)$$

where $F^{(\phi)}$ and $F^{(z)}$ are the latitudinal and vertical components of the EP vector, ϕ is the latitude, z is a log-pressure coordinate, ρ_0 the density, f the Coriolis parameter, a the mean radius of the earth. The overbar denotes the zonal average and prime the deviations from the zonal average. u' , v' , w' and θ' correspond to the zonal, meridional, vertical wind and potential temperature perturbations respectively.

The terms $\overline{u'v'}$, $\overline{v'\theta'}$, $\overline{u'w'}$ in equations 2.16 and 2.17 can be computed from the cospectrum (Co) of their Fourier transforms which is defined as:

$$Co(u', v') = \hat{U} \hat{V}^* \quad (2.18)$$

$$Co(v', \theta') = \hat{V} \hat{\Theta}^* \quad (2.19)$$

$$Co(u', w') = \hat{U} \hat{W}^* \quad (2.20)$$

Here \hat{U} , \hat{V} , $\hat{\Theta}$, \hat{W} correspond to the Fourier transforms of u' , v' , θ' , w' respectively and the asterisk denotes the complex conjugate. The perturbation fields are a function of latitude, longitude, height and time. For each model latitude in the equatorial belt (10°S-10°N) and each model level above 100 hPa we compute the two dimensional FFT of u' , v' , w' and θ' as a function of frequency ω and zonal wavenumber k . Hence at each latitude y and altitude z , the spectral analysis provides the zonal wavenumber-frequency distributions $F^{(\phi)}(\omega, k, y, z)$ and $F^{(z)}(\omega, k, y, z)$.

As the model data are real, the computed Fourier transforms \hat{U} , \hat{V} , \hat{W} and $\hat{\Theta}$ satisfy the relationship:

$$\hat{U}(\omega, k) = \hat{U}(-\omega, -k) \quad (2.21)$$

$$\hat{V}(\omega, k) = \hat{V}(-\omega, -k) \quad (2.22)$$

$$\hat{W}(\omega, k) = \hat{W}(-\omega, -k) \quad (2.23)$$

$$\hat{\Theta}(\omega, k) = \hat{\Theta}(-\omega, -k) \quad (2.24)$$

This means that there is a redundancy in $F^{(\phi)}(\omega, k, y, z)$ and $F^{(z)}(\omega, k, y, z)$. To eliminate this redundancy, we retain only the part of the distributions associated with positive frequencies and negative/positive wavenumbers. $\omega > 0$ and $k > 0$ correspond to eastward propagating waves while $\omega > 0$ and $k < 0$ indicate westward propagating waves. We use this convention as we assume waves of the form $e^{i(kx - \omega t)}$.

We are interested in waves with upward group propagation (as the source is tropospheric convection), therefore negative values of $F^{(z)}$ indicate waves that propagate upward and eastward while positive values of $F^{(z)}$ correspond to waves that propagate upward and westward.

Finally by integrating $Co(u', v')$, $Co(v', \theta')$ and $Co(u', w')$ over wavenumbers and frequencies we obtain $F^{(\phi)}$ and $F^{(z)}$ as a function of latitude and height.

Chapter 3

Intermediate-scale tropical inertia-gravity waves observed during the TWP-ICE campaign

As stated in Chapter 1, few studies have characterized inertia-gravity wave properties using radiosonde profiles collected on a campaign basis. However, observational studies are important to document the space-time variability of the wave activity and to validate the representation of inertia-gravity waves in high resolution models.

In tropical Australia, the area of Darwin constitutes an ideal site to study convection as this region is under the influence of the Asian and Indian monsoons. In addition, this region is characterized by considerable convective activity on a wide range of scales from localized thunderstorms up to global-scale intra-seasonal variability associated with the Madden Julian Oscillation.

Therefore, the Tropical Warm Pool International Cloud Experiment (TWP-ICE) was conducted from 23 January to 13 February 2006 in this area. The experiment goal was to describe the evolution of tropical convection, including the large-scale heat, moisture, and momentum budgets, while at the same time obtaining detailed observations of cloud properties and the impact of clouds on the environment. A general description of the campaign was given in the work of May et al. (2008).

Using TWP-ICE radiosonde data, we will focus in this chapter on the study of 2-day tropical waves observed during the campaign. The chapter is organized as follows. The data used and meteorological conditions are described in Section 3.1. The inferred wave properties are presented in Section 3.2. Section 3.3 discusses the nature of the waves. A short summary and conclusions are

given in Section 3.4.

3.1 Data and Meteorological conditions

The data used in this chapter are radiosonde data acquired 8 times per day (3-hourly) from a circular network of four stations around Darwin (Figure 3.1) and from a ship west of Darwin. Contrary to the other sites Darwin has 6-hourly soundings.

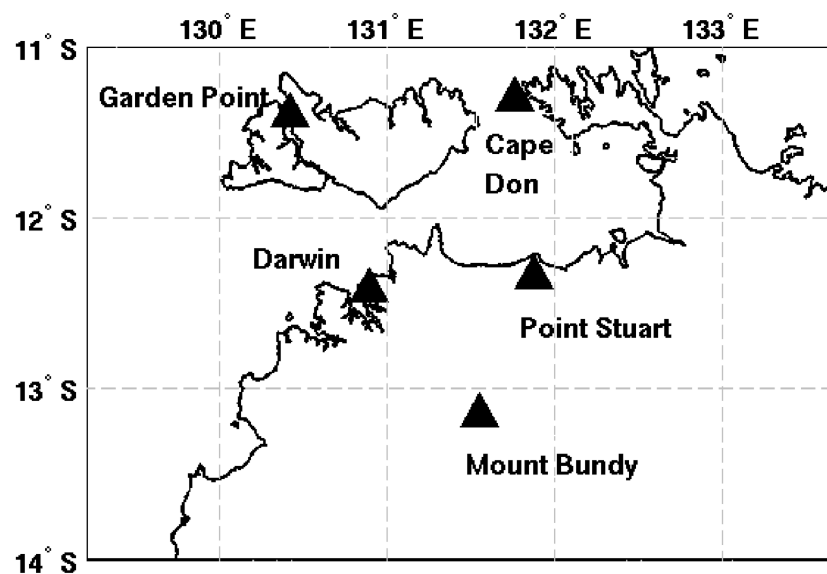


Figure 3.1: Location of the radiosonde sites used in the study.

Table 3.1 presents the radiosonde profile statistics. On average more than 60% of the profiles reached an altitude of 28 km. In general in the first part of the campaign more profiles failed to reach 20 km. Point Stuart and Darwin had the largest percentage of balloons reaching 25 km. The ship was the site with the lowest profiles and therefore is not used in this chapter.

The data are interpolated to a vertical spacing of 50 m and additional interpolation in time is computed to fill the missing data. Temporal linear trends are then removed from the entire record

to define the time series of perturbations of horizontal velocities and temperature. The S-Transform described in chapter 2 is used to analyse the time series of the perturbations.

Table 3.1: Radiosonde profile statistics.

Sites	Total	$H > 20km$	$H > 25km$
Garden Point	162	62%	60%
Cape Don	173	72%	68%
Mount Bundy	165	78%	70%
Point Stuart	175	84%	73%
Darwin	82	90%	83%
Total	757	77.2%	70.8%

Figure 3.2 shows the latitude-height cross section of zonal wind averaged over January-February 2006 at the longitude of Darwin (130.89°E). The data correspond to the National Centers for Environmental Prediction reanalysis with 27 pressure levels. Between 20 and 25 km, easterly winds dominate with a westerly shear zone above: the transition from the end of the easterly phase to the beginning of the westerly phase of the QBO can be observed.

The mean vertical profiles of zonal wind, meridional wind, temperature and buoyancy frequency squared averaged over the TWP-ICE campaign period are plotted on Figure 3.3. Weak westerlies below 5 km associated with the Australian monsoon were observed at all sites. The meridional wind was fairly weak with the presence of wave-like perturbations with growing amplitude above 20 km (Figure 3.3).

During the experiment, the mean tropopause defined as the cold point tropopause was located at 17.5 km with a temperature of 190 K and the buoyancy frequency N was equal to $2.4 \times 10^{-2} \text{ s}^{-1}$ in the stratosphere.

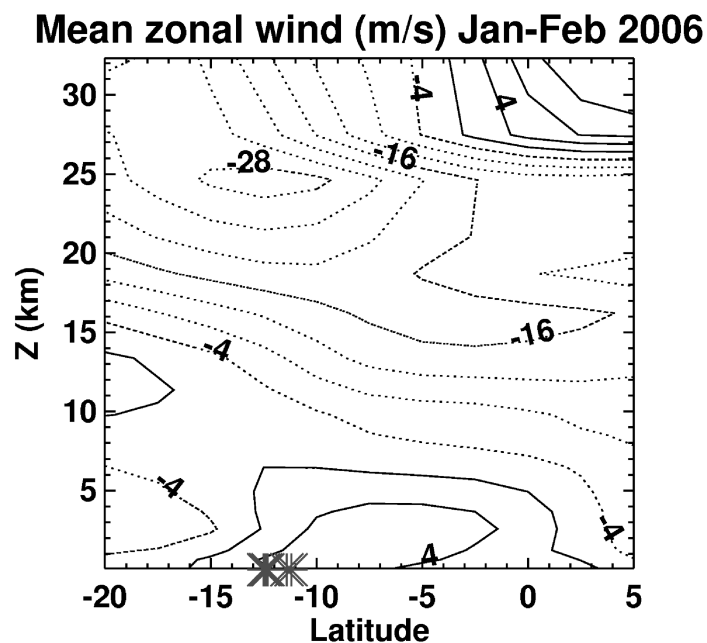


Figure 3.2: Latitude-height cross section of zonal wind averaged over January-February 2006 at the longitude of Darwin (130.89°) (from NCEP/DOE 2 Reanalysis data provided by the NOAA/OAR/ESRL PSD, Boulder, Colorado, USA, <http://www.cdc.noaa.gov/>). The contour interval is 4 m s^{-1} . Negative values are dotted. The crosses indicate the latitudes of the different radiosonde sites.

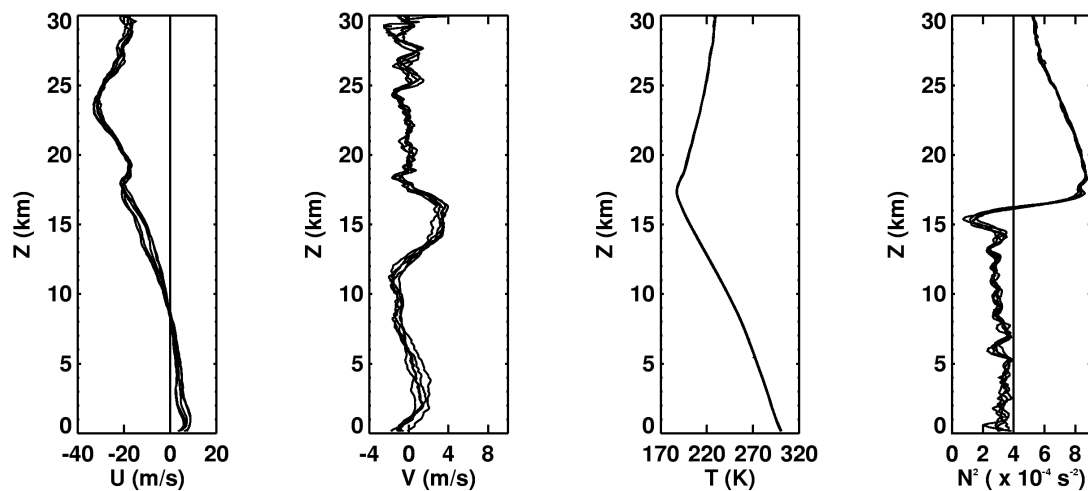


Figure 3.3: Mean vertical profiles of zonal wind (U), meridional wind (V), temperature (T) and buoyancy frequency squared (N^2) averaged over the TWP-ICE campaign period. Each line represents a different site.

At the beginning of the campaign, the Darwin area experienced an active monsoon.

Figure 3.4 corresponds to a sequence of daily average (average over UTC times) infrared brightness temperature from 20 January to 31 January 2006. From 19 to 24 January Tropical Cyclone Daryl formed off the West Australia coast (around 18°S , 116°E) then moved southwest and weakened over the Indian Ocean (Figure 3.4). On January 23 a large Mesoscale Convective System developed south of Darwin (around 11°S , 128°E) and evolved into a large Mesoscale Convective Complex with an anvil exceeding 500 km in diameter. During the following days, the system moved over land and became a monsoon low. This monsoon low was observed until February 1 when it started to weaken. Break period conditions of the Australian monsoon were observed from February 3 until the end of the campaign.

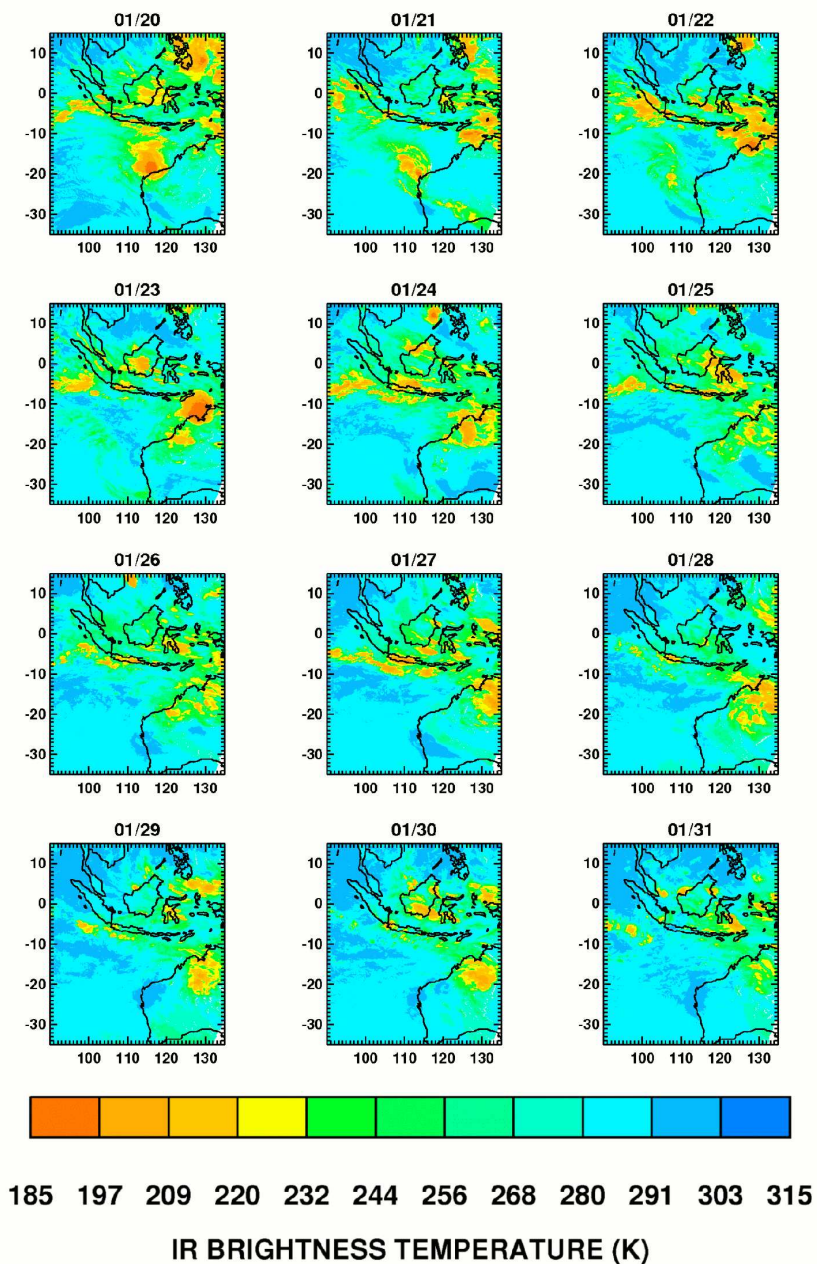


Figure 3.4: Sequence of daily average (average over UTC times) infrared brightness temperature (from TRMM global-merged data set) from 20 January to 31 January 2006. On January 19 Tropical Cyclone Daryl can be observed at 18°S, 116°E. On January 23 a Mesoscale Convective System developed south of Darwin (around 11°S, 128°E).

3.2 Wave properties

3.2.1 Period

Figure 3.5 shows the time-height series of unfiltered perturbations of temperature and meridional and zonal winds observed at Point Stuart. Clear signatures of waves can be observed in the upper troposphere and stratosphere with downward phase propagation. The phase tilt indicates that energy is propagating upward. At 15 km, strong perturbations during the first 15 days of the campaign can be observed. The same features were observed at all the different sites (not shown). It is noteworthy that a diurnal tide was also observed in the data of temperature and zonal and meridional winds for all of the sites (Alexander and Tsuda, 2008).

Figure 3.6 shows the average of the wavelet power spectra of time series of perturbations for the height ranges 22-26 km. The maximum amplitude corresponds to a period of 2.5 days for a wave event occurring in the middle of the campaign. Although at the latitude of Darwin the inertial period is 2.4 days (corresponding to the longest period a gravity wave can have in this region), a signal with a period of 2.5 days can still be observed in the data, as 2.4 days refers to the longest intrinsic period while what is measured is the period in the ground-based reference frame.

In order to remove longer period equatorial wave mode signals in the data and to keep the 2.5-day signal we apply a band-pass filter (a modified Welch window) with cut-off frequencies at 0.3 and 0.6 day^{-1} (1.7-3.3 days). The resulting filtered perturbations for Point Stuart can be seen on Figure 3.7.

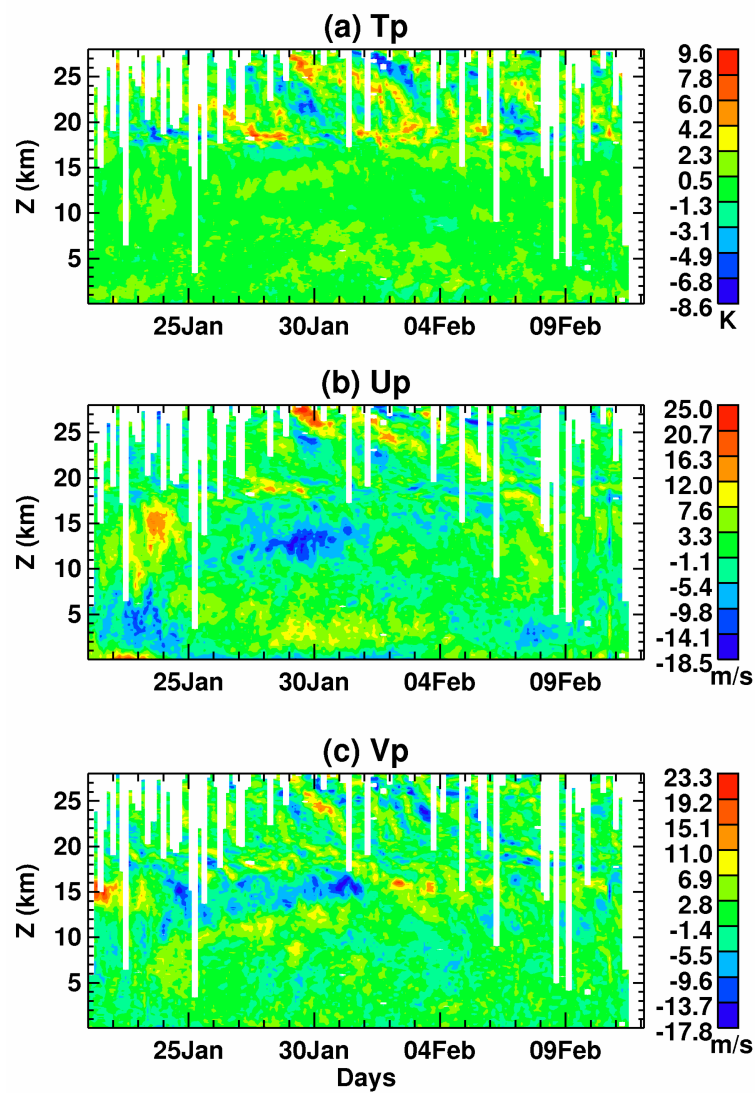


Figure 3.5: Time-height series of unfiltered perturbations of (a) Temperature (T_p), (b) zonal wind (U_p), (c) meridional wind (V_p) observed at Point Stuart.

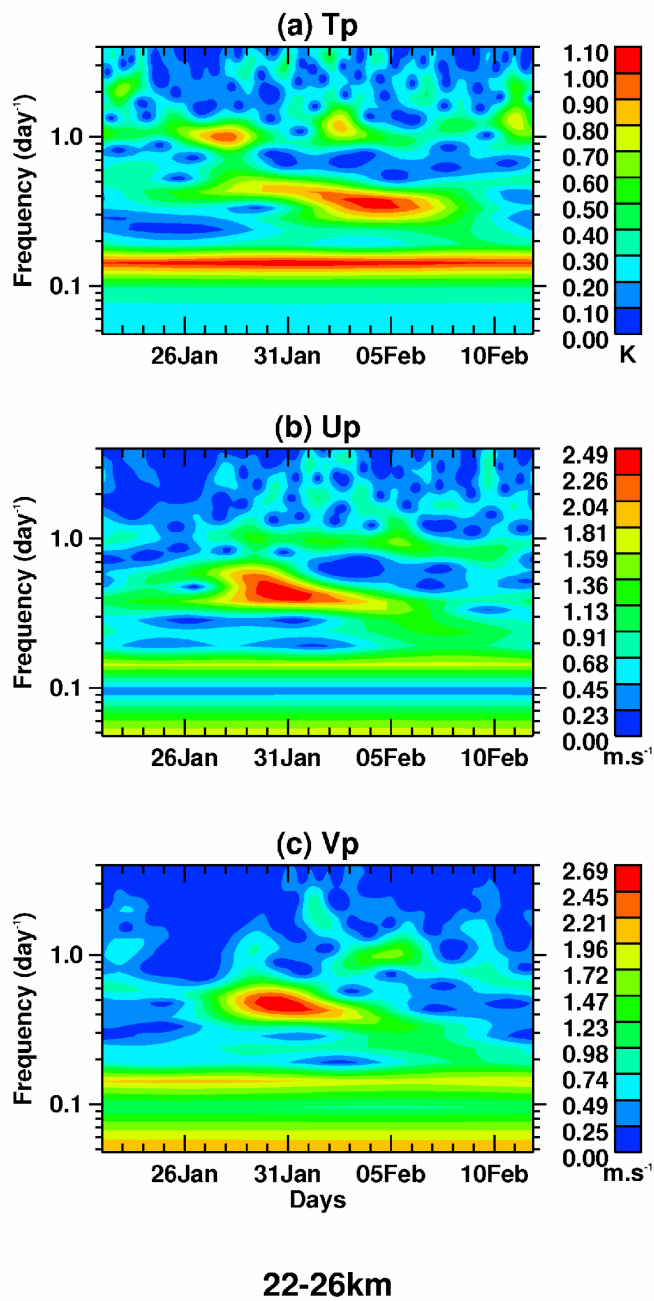


Figure 3.6: Time-frequency spectrum averaged between 22 and 26km for the perturbations of (a) temperature, (b) zonal wind and (c) meridional wind observed at Point Stuart.

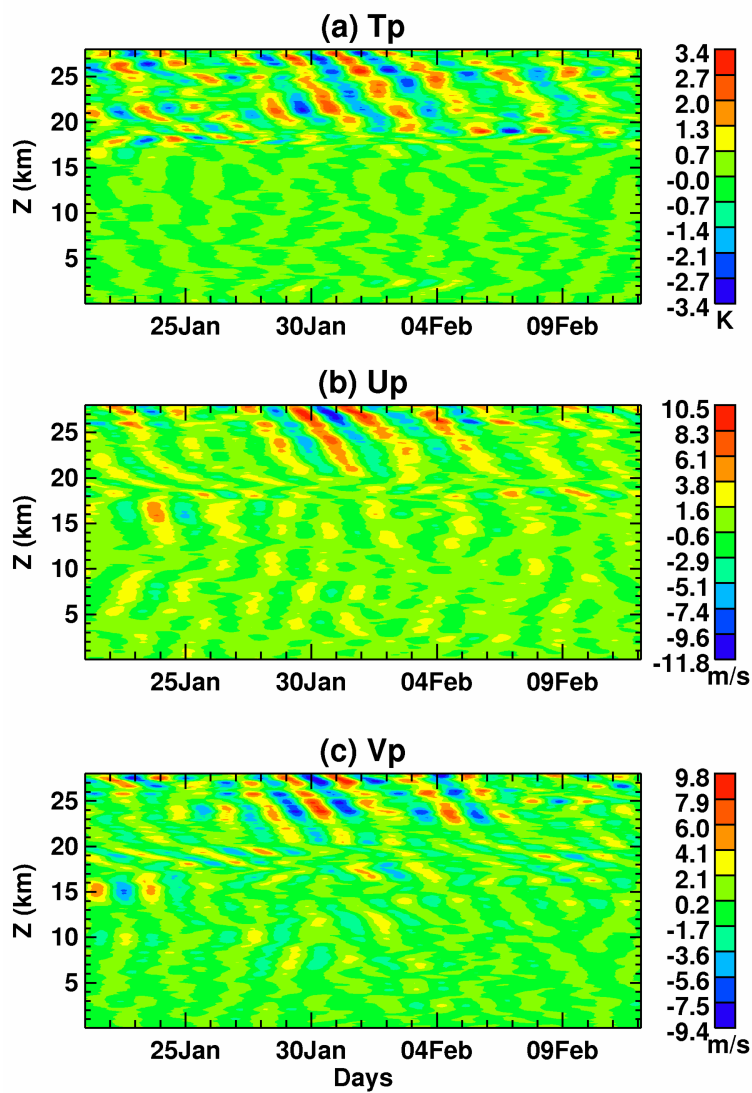


Figure 3.7: Time-height series showing the perturbations of (a) temperature (T_p), (b) zonal wind (U_p), (c) meridional wind (V_p) observed in the 1.7-3 day range at Point Stuart.

3.2.2 Vertical wavelength

The difference of phase between the perturbations at various levels and a reference level can provide information about the vertical structure of the waves (Wada et al., 1999). We use the cross-spectrum for a time series of zonal wind perturbations at a reference height and at other different altitudes. The reference height is fixed at 23 km which corresponds to the altitude of maximum amplitude for the 2.5 day-period.

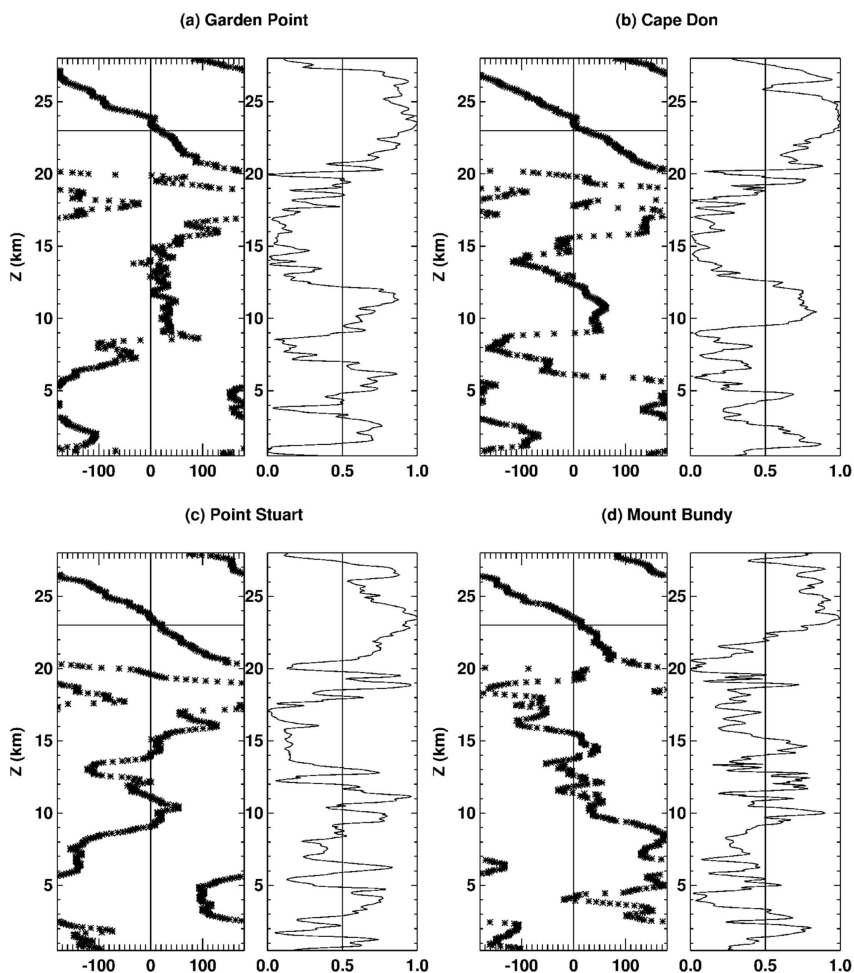


Figure 3.8: Vertical profiles of phase differences and coherences of u' for a period of 2.5 days at (a) Garden Point, (b) Cape Don, (c) Point Stuart, (d) Mount Bundy. The reference level is 23km.

The vertical profiles of phase differences and coherences of the zonal wind perturbations u' for a period of 2.5 days can be seen on Figure 3.8. A consistent phase-height relationship is observed above 20 km associated with a strong coherence. From the profile of phase difference the vertical wavelength is estimated to be around 6 km for the zonal wind perturbations. The analysis for the meridional wind perturbations gives a similar result (not shown). The temperature fluctuations show a vertical wavelength in the range 5-7 km and somewhat higher variability is observed in the phase and coherence (not shown).

3.2.3 Horizontal structure

For each altitude between 22 and 26 km the phase shift between two sites is calculated by averaging over the two-day time period surrounding the maximum in the wavelet covariance spectrum (defined by the frequency f_m and time t_m). The final phase shift between two sites is the average of the vertical profile of phase between 21 and 26 km.

From the horizontal phase lag, the apparent wavelength is estimated along the line joining the two sites by :

$$\lambda_a = \frac{2\pi\Delta x}{\Delta\phi} \quad (3.1)$$

Where Δx is the distance between the two sites.

Figure 3.9 presents the vertical profiles of phase differences for time series of zonal wind between Mount Bundy and the other sites. On this plot, Mount Bundy is taken as the reference site.

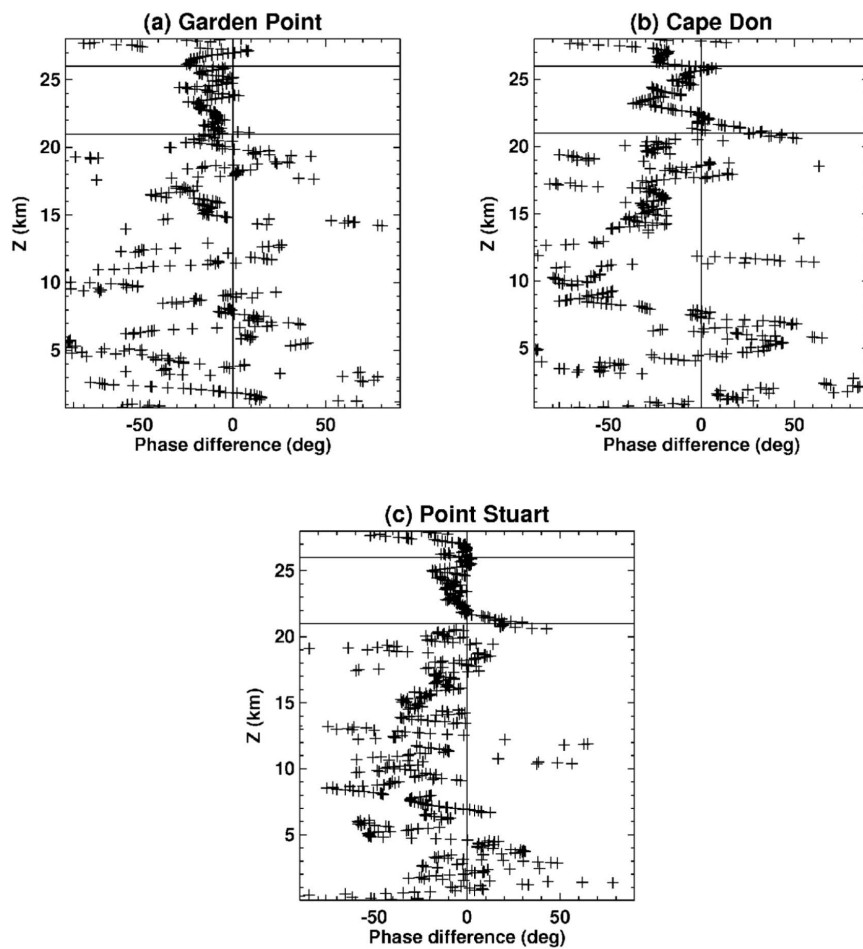


Figure 3.9: Vertical profiles of phase differences for time series of zonal wind between (a) Mount Bundy and Garden Point, (b) Mount Bundy and Cape Don, (c) Mount Bundy and Point Stuart.

The same calculations were done for Point Stuart and the average phase differences are summarized in Table 3.2 and Table 3.3.

Table 3.2: Phase differences between Mount Bundy and other sites. Mount Bundy is taken as the reference site.

Sites	Phase difference (degree)	Distance (km)	λ_a (km)
Garden Point	-10.56	230.26	7850
Cape Don	-8.38	206.35	8865
Point Stuart	-2.85	96.62	12205

Table 3.3: Phase differences between Point Stuart and other sites. Point Stuart is taken as the reference site

Sites	Phase difference(degree)	Distance (km)	λ_a (km)
Garden Point	-7.63	190.51	8989
Cape Don	-6.20	115.92	6731

The values of phase differences show that Mount Bundy lags Point Stuart which lags Cape Don and Garden Point. This fact indicates a south to southeastward propagation for the waves. For finding the horizontal wavelength, we compute an angle of propagation and a horizontal wavelength that fits the apparent horizontal wavelengths along the lines joining pairs of sites (Ratnam et al., 2006).

Considering lines of constant phase of the wave on an (x,y) plane, if the line between two sites lies along the propagation direction of the wave, then the true horizontal wavelength is equal to the apparent horizontal wavelength. If the line between two sites lies at different angles α_1 and α_2 from the propagation direction (Figure 3.10) then:

$$\lambda_h = \lambda_1 \cos \alpha_1 = \lambda_2 \cos \alpha_2 \quad (3.2)$$

In this equation, λ_h is the true horizontal wavelength, λ_1 and λ_2 are the apparent wavelengths between site 1 and site 2 and between site 1 and site 3 respectively. Using these equations for each

pair of sites, a combination of three sites gives the solution :

$$\delta = \arctan \left(\frac{\lambda_2 \cos \theta_2 - \lambda_1 \cos \theta_1}{\lambda_1 \sin \theta_1 - \lambda_2 \sin \theta_2} \right) \quad (3.3)$$

Where δ is the horizontal angle of propagation (expressed in degrees from the West-East direction). To compute δ we assume that the waves have same propagation direction in the stratosphere.

The values of apparent wavelengths found between the different pairs of sites are given in Table 3.4 and the angles of propagation and horizontal wavelengths found using (3.2) and (3.3) are presented in Table 3.5. We found a mean horizontal wavelength of 7220 km (5500 to 8700 km) and an angle of propagation of -74° (in degrees from the eastward direction).

Table 3.4: Apparent wavelengths between the different pairs of sites (G: Garden Point, C: Cape Don, P: Point Stuart, M: Mount Bundy)

λ (km)	G	C	P	M
G	0			
C	180,000	0		
P	8989	6731	0	
M	7850	8865	12205	0

Table 3.5: Directions of horizontal propagation (degrees from East) estimated with different combinations of sites.

	GCP	PGC	CPG	GPM	PMC	MGP	CPM	GCM	CMG	MGC	Average
Angle (deg)	-86	-86	-76	-62	-61	-63	-66	-86	-67	-86	-74
λ (km)	6727	5475	6661	7900	7832	7817	6411	8715	7741	6919	7220

In addition we computed the mean direction of propagation by using the covariance between the velocities and temperature perturbations. The mean direction (in degrees from the eastward

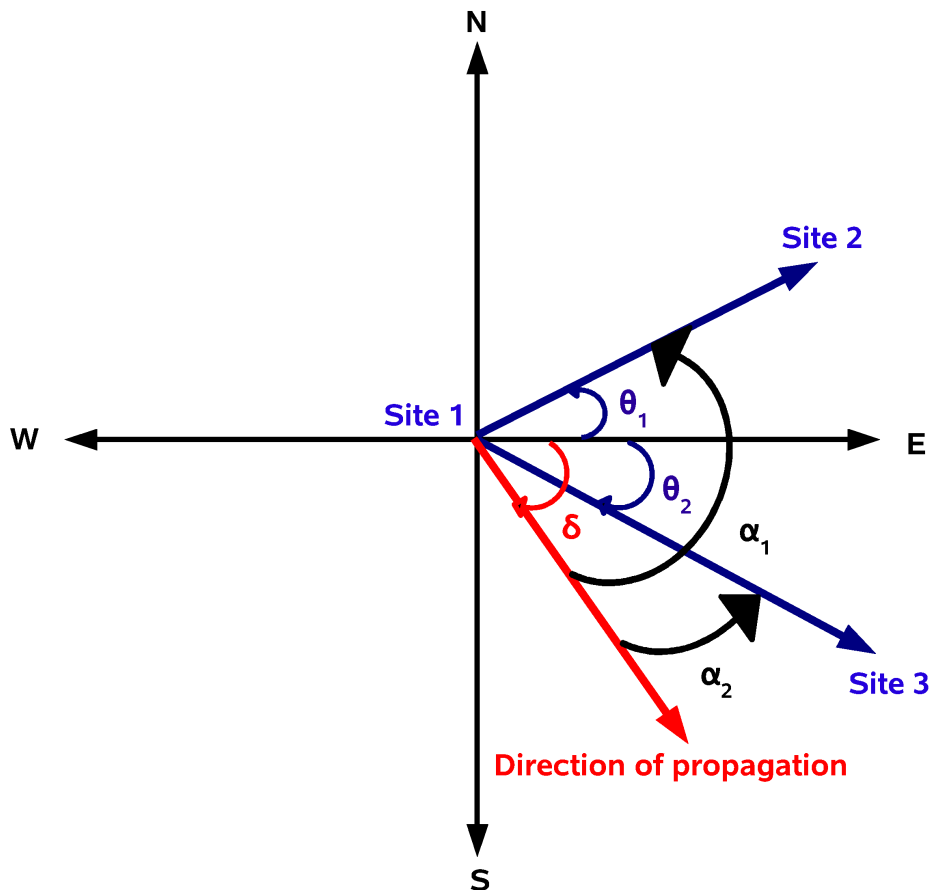


Figure 3.10: Schematic showing angles between sites (see text for explanations).

direction) can be expressed as (Vincent et al., 1997):

$$\delta = \arctan \left(\frac{\overline{u'T'_{+90}}}{\overline{v'T'_{+90}}} \right) \quad (3.4)$$

Where T'_{+90} is the value of the temperature after shifting the phase by $+90^\circ$ via the Hilbert transform.

Figure 3.11 shows the distribution of the mean direction of propagation for all of the sites. 63% of the profiles show a southeastward propagation ($-90^\circ < \delta < 0^\circ$). For angles less than 0 degrees (southward propagation), the median is -47.3° which is consistent with the southeastward

propagation established with the cross-spectrum analysis.

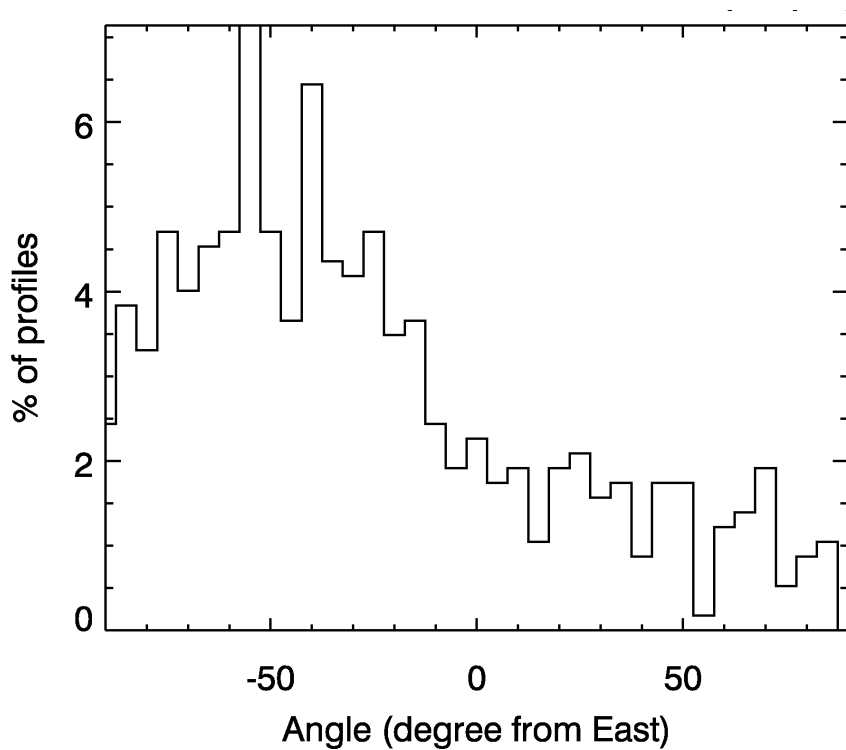


Figure 3.11: Distribution of directions of horizontal propagation derived from velocity and temperature perturbations. The distribution includes angles for Garden Point, Mount Bundy, Point Stuart and Cape Don.

3.3 Identification of Inertia-Gravity Waves

3.3.1 Quadrature spectrum

Inertia-gravity waves are influenced by the rotation of the Earth and have intrinsic frequencies of the same order as the Coriolis parameter. For these types of waves, the wind velocity perturbations are related by:

$$\tilde{v} = -i \frac{f}{\hat{\omega}} \tilde{u} \quad (3.5)$$

where \tilde{u} and \tilde{v} correspond to the amplitudes of the wind velocity perturbations that are parallel and orthogonal to the wave propagation direction respectively. The wind velocity perturbations are one-quarter cycle out of phase, and thus will have large signals in the quadrature spectrum of zonal (u') and meridional (v') wind fluctuations.

Figure 3.12 shows the vertical profile of the quadrature spectrum of u' and v' . Large amplitudes can be seen above 22 km demonstrating the presence of inertia-gravity waves during the campaign in the lower stratosphere.

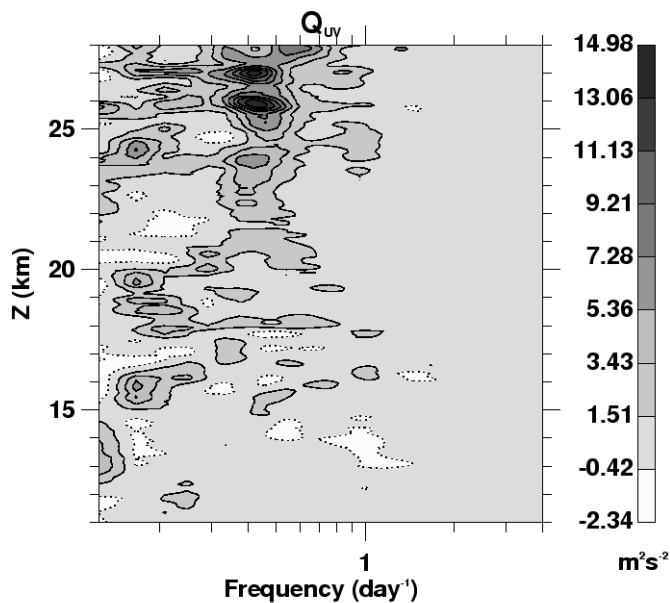


Figure 3.12: Vertical profile of quadrature spectrum of zonal and meridional wind perturbations observed at Garden Point. Positive quadrature in solid and negative quadrature in dots.

3.3.2 Intrinsic frequency and group propagation

To assess the wave characteristics relevant to the general circulation, we can use the dispersion relation for low frequency inertia-gravity waves. For a linear gravity wave with horizontal wavenumber k_h , the intrinsic frequency $\hat{\omega}$ is given by:

$$\hat{\omega} = \omega - \overline{u_h}k_h, \quad (3.6)$$

where ω is the ground-based frequency and $\overline{u_h}$ is the background wind speed in the direction of wave propagation. During the campaign, the background wind was easterly in the stratosphere (-25 m s^{-1}). Assuming that the waves propagate southeastward toward -74° , have a ground-based period of 2.5 days, a horizontal wavelength λ_h around 5500 to 8700 km, the intrinsic frequency is estimated to be around $3.70 \times 10^{-5} \text{ s}^{-1}$ and $3.41 \times 10^{-5} \text{ s}^{-1}$ (≈ 2 days).

Furthermore, $\hat{\omega}$ can be deduced from the dispersion relation for low-frequency inertia-gravity waves (Fritts and Alexander, 2003):

$$\hat{\omega}^2 = f^2 + N^2 \frac{k_h^2}{m^2} \quad (3.7)$$

f represents the Coriolis parameter equal to $-3.132 \times 10^{-5} \text{ s}^{-1}$ at the latitude of Darwin, N is the buoyancy frequency ($= 2.449 \times 10^{-2} \text{ s}^{-1}$ in the stratosphere), k_h and m are the horizontal and vertical wavenumbers. According to equation (3.7) $\hat{\omega}$ is equal to $4.12 \times 10^{-5} \text{ s}^{-1}$ and $3.56 \times 10^{-5} \text{ s}^{-1}$ for λ_h equal to 5500 km and 8700 km respectively. In both cases, the relative error is less than 11 % which confirms the estimate of the wave parameters.

The vertical group velocity ($-\frac{k_h^2 N^2}{\hat{\omega} m^3}$) lies between 1.62 km day^{-1} and $0.647 \text{ km day}^{-1}$ for λ_h between 5500 and 8700 km. Assuming a source located in the troposphere (convection) and waves generated in the upper troposphere around 17 km, then 4 to 12 days are needed for the perturbations to propagate upward to 25 km. The S-Transform analysis indicates that the wave mainly occurred between the 28th of January and the 5th of February. Using a vertical profile of temperature averaged over the campaign period we can estimate $\tau(m, z)$, the scale-dependent relaxation time for radiative damping (Fels, 1982). Figure 3.13 shows the vertical profile of $\tau(m, z)$

for a vertical wavelength of 6 km. Between 20 and 28 km the average $\tau(m, z)$ is equal to 6.7 days. This value is in agreement with the time observed for the wave to dissipate in the stratosphere and suggests that radiative damping is the main cause of the wave attenuation.

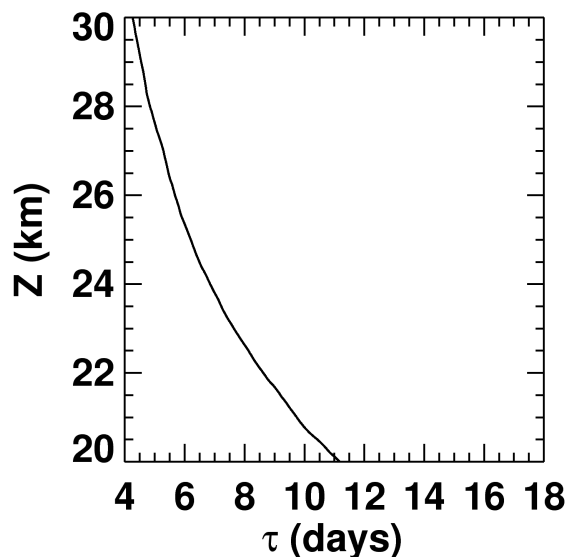


Figure 3.13: Vertical profile of time scale for radiative damping for a vertical wavelength of 6km.

On Figure 3.4, the low values of brightness temperature over the Indonesian region tend to indicate strong convective activity on the middle of January. For low frequency inertia-gravity waves the vertical group velocity is much smaller than the horizontal group velocity. Therefore this type of wave can propagate over large horizontal distances and the observed wave is likely generated in association with strong convection over Indonesia.

These waves cannot propagate meridionally beyond the latitude at which the intrinsic wave frequency equals the inertial frequency (Sato et al., 1999, 2003) and with $\hat{\omega} = 3.64 \times 10^{-5} \text{ s}^{-1}$ (period of 2 days) the critical latitude corresponds to $\pm 14.44^\circ$. The waves observed may be refracted or absorbed while moving southward toward the critical latitude. After reflection if they still propagate upward and eastward in the equatorial region they might encounter the westerly wind observed at 4°S on Figure 3.2. This can cause the vertical wavelength to shrink and thus to decrease the scale-

dependent relaxation time for radiative damping. As a result the dissipation might be stronger after reflection at 14.44°S.

The latitudinal distribution of the QBO in the zonal wind has a 12° half-width and considerable amplitudes are still observed at 20° (Baldwin et al., 2001). Thus the calculated critical latitudes are well inside the QBO region and the observed wave might impact the mean circulation between $\pm 14.44^\circ$.

3.3.3 Wave Energy

According to the linear wave theory, the partitioning of total gravity wave energy into potential energy (PE) and kinetic energy (KE) depends on the ratio $\alpha = \frac{|k_h|}{m}$ (Gill, 1982):

$$\frac{KE}{PE} = 1 + \frac{2f^2}{N^2\alpha^2} \quad (3.8)$$

Yamamori and Sato (2006) used the dispersion relation for low frequency inertia-gravity waves to express (3.8) as:

$$\frac{KE}{PE} = \frac{1 + (f/\hat{\omega})^2}{1 - (f/\hat{\omega})^2} \quad (3.9)$$

For the area of Darwin f varies between $-3.338 \times 10^{-5} \text{ s}^{-1}$ (at Cape Don) and $-3.073 \times 10^{-5} \text{ s}^{-1}$ (at Mount Bundy) which gives a mean value of $-3.205 \times 10^{-5} \text{ s}^{-1}$. With an intrinsic period of 2 days then KE/PE should equal 6. We compute the mean kinetic and potential energies for the period corresponding to the maximum of wave activity between January 28 and February 5. The mean temperature and buoyancy profiles used to define PE were estimated by an average over the period of the campaign. Table 3.6 shows the averaged potential and kinetic energies as well as the ratio of KE to PE for the band-pass filtered perturbations for the height ranges 22-27 km. In general a mean ratio between 5 and 6 was observed for all the sites except Darwin. As expected, the large ratio for KE/PE is consistent with the presence of low-frequency inertia-gravity waves in the stratosphere.

Table 3.6: Density of Kinetic (KE) and Potential Energy (PE) averaged between 22 and 27km for all of the sites.

Sites	KE, m ² s ⁻²	PE, m ² s ⁻²	KE/PE
Garden Point	14.2	2.6	5.5
Cape Don	18.7	3.2	5.8
Point Stuart	13.5	2.5	5.4
Darwin	15.2	4.1	4.1
Mount Bundy	13.5	2.7	5.0

3.3.4 Momentum Flux

To assess the importance of the wave event we compute the total vertical flux of horizontal momentum associated with the 2-day waves,

$$F_{ph} = \bar{\rho} \left(1 - \frac{f^2}{\hat{\omega}^2}\right) (\overline{u'w'^2} + \overline{v'w'^2})^{1/2} \quad (3.10)$$

Ern et al. (2004) expressed equation (3.10) as,

$$\begin{aligned} F_{ph} &= \left[1 - \frac{\hat{\omega}^2}{N^2}\right] \left[1 + \frac{1}{m^2} \left(\frac{1}{2H} - \frac{g}{c_s^2}\right)\right]^{-1} \\ &\times \left[1 + \left(\frac{f}{\hat{\omega}m}\right)^2 \left(\frac{1}{2H} - \frac{g}{c_s^2}\right)\right]^{1/2} \\ &\times \frac{1}{2} \bar{\rho} \frac{k_h}{m} \left(\frac{g}{N}\right)^2 \left(\frac{\hat{T}}{\bar{T}}\right)^2 \end{aligned} \quad (3.11)$$

where \hat{T} is the temperature amplitude of the wave, k_h and m are the horizontal and vertical wavenumbers, $\bar{\rho}$ is the background density, g is Earth's gravitational acceleration, N is the buoyancy frequency, H is the scale height of the atmosphere and \bar{T} is the background temperature. As $\hat{\omega} \ll N$ and $1/m^2 \ll 4H^2$, by letting the sound speed $c_s \rightarrow \infty$

(3.11) yields :

$$\frac{F_{ph}}{\bar{\rho}} = \frac{1}{2} \frac{k_h}{m} \left(\frac{g}{N}\right)^2 \left(\frac{\hat{T}}{\bar{T}}\right)^2 \quad (3.12)$$

With a mean stratospheric temperature of $\bar{T} = 217$ K between 20 and 30 km, $\hat{T} = 1.10$ K estimated with the S-Transform analysis, for λ_h between 5500 and 8700 km, $\lambda_z = 6$ km then $F_{ph}/\bar{\rho}$ is ranging

from 1.4×10^{-3} to $2.2 \times 10^{-3} \text{ m}^2 \text{ s}^{-2}$.

The vertical flux of horizontal momentum obtained with (3.12) corresponds to an absolute value and thus does not take in account the wave propagation direction. However Sato and Dunkerton (1997) used the quadrature spectra Q_{Tu} of u and T fluctuations to provide a direct estimate of the zonal momentum flux of equatorial waves. By analogy, the total momentum flux in the horizontal direction of propagation of the wave can be expressed as,

$$\overline{u'_h w'} = -\frac{g}{\overline{T} N^2} \int_{\omega_1}^{\omega_2} Q_{Tu_h}(\hat{\omega}) \hat{\omega} d\hat{\omega} \quad (3.13)$$

where Q_{Tu_h} is the quadrature spectrum of T and u_h , the wind fluctuations along the horizontal direction of propagation. The quadrature spectrum is calculated for both propagation directions (-74° and -47.3°) for all stations considered. First $Q_{Tu_h}(\omega)$, the quadrature spectrum as a function of the ground-based frequency, is computed by using the cross S-Transform of T and u_h series at each altitude. The result is then averaged for the period of maximum wave activity between 28 January and 5 February. Then $Q_{Tu_h}(\omega)$ is shifted by 0.5 days (which corresponds to the average difference between intrinsic and ground-based wave periods) to obtain the quadrature spectrum as a function of the intrinsic frequency $Q_{Tu_h}(\hat{\omega})$. Finally $Q_{Tu_h}(\hat{\omega})$ at each altitude is integrated between the frequencies 0.4 and 0.7 day^{-1} (1.5-2.5 days) to make sure that the 2-day spectral peak attributed to the inertia-gravity wave is covered. We use 217 K and $6 \times 10^{-4} \text{ s}^{-2}$ as values for \overline{T} and N^2 .

Figure 3.14 shows the vertical profiles of momentum flux for waves of 1.5-2.5 day period for all of the sites for both propagation directions. For all the sites positive values of $\overline{u'_h w'}$ were observed above 20 km. This confirms the dominance of an upward and southeastward propagating wave in the range 0.4 - 0.7 day^{-1} . The momentum flux starts to decrease above 25 km. As the winds are easterly in the stratosphere and the waves propagate eastward, the observed waves are not attenuated because of the critical-level effect.

Moreover, we have previously seen that the radiative damping is probably the main process responsible for the waves' attenuation between 20 and 28 km. This agrees with the fact that the

maximum of momentum flux is seen at 25 km.

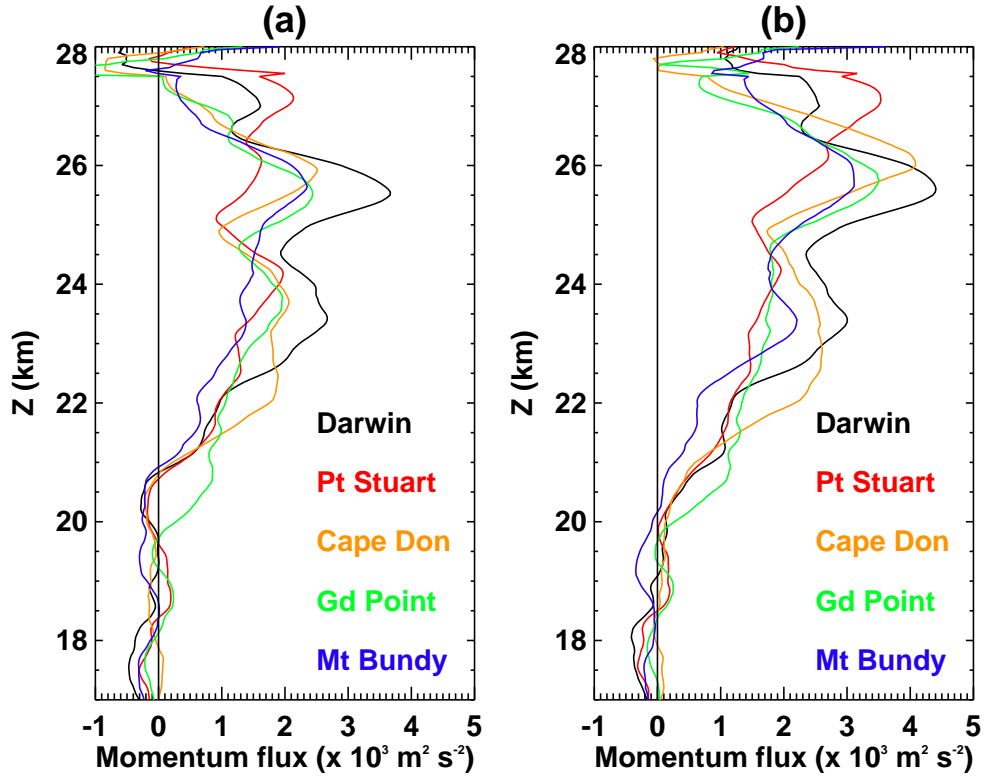


Figure 3.14: Vertical profiles of the momentum fluxes for waves of 1.5-2.5 day period for all of the sites. (a) Angle of propagation of -74° and (b) angle of propagation of -47.3°

Table 3.7 summarizes the average of $\overline{u'_h w'}$ for the height region 20 to 28 km at each station. Values of total momentum flux $\overline{u'_h w'}$ and zonal momentum flux $\overline{u' w'}$ are shown for the two different angles of propagation. The values of total momentum fluxes obtained from (3.12) and (3.13) are of the same order of magnitude and range from 1 to $2 \times 10^{-3} \text{ m}^2 \text{ s}^{-2}$.

The uncertainty in the direction of propagation leads to an uncertainty in the values of the zonal momentum fluxes. We can see that the average of $\overline{u' w'}$ between 20 and 28 km ranges from 0.3 to $1.03 \times 10^{-3} \text{ m}^2 \text{ s}^{-2}$.

The upper limit of $\overline{u' w'}$ is consistent with the values of momentum fluxes obtained by Sato and Dunkerton for 1-3 day waves during the easterly shear phase of the QBO at Singapore

Table 3.7: Total momentum flux $\overline{u'_h w'}$ and zonal momentum flux $\overline{u' w'}$ ($\times 10^{-3} \text{ m}^2 \text{ s}^{-2}$) averaged between 20 and 28km

Sites	$\overline{u'_h w'} (-74^\circ)$	$\overline{u'_h w'} (-47.3^\circ)$	$\overline{u' w'} (-74^\circ)$	$\overline{u' w'} (-47.4^\circ)$
Garden Point	1.18	1.68	0.33	0.80
Cape Don	1.17	1.94	0.39	0.82
Point Stuart	1.14	1.69	0.31	0.78
Darwin	1.52	2.16	0.42	1.03
Mount Bundy	1.00	1.56	0.30	0.70

($1.4^\circ \text{N}, 104^\circ \text{E}$). In addition, the zonal momentum fluxes observed are greater than those obtained by Holton et al. (2001) for 8-17 and 4-6 days Kelvin waves at Nauru ($0.5^\circ \text{S}, 166.9^\circ \text{E}$) and Murthy et al. (2002) for 6.7 and 7.8 days Kelvin waves observed at Gadanki ($13.5^\circ \text{N}, 79.2^\circ \text{E}$).

3.4 Summary and conclusions

A 2-day wave event was observed during the TWP-ICE campaign, from January 28 to February 5 in the lower stratosphere over the Darwin area. Using the S-Transform analysis, the vertical and horizontal wavelengths were estimated to be around 6 km and 7220 km respectively. Moreover, the waves showed a southeastward propagation confirmed both by the cross S-Transform analysis and the covariance of horizontal velocities and temperature fluctuations. The group velocity of the observed waves being small, they were confined to the lower stratosphere and were likely attenuated because of radiative damping. The waves were identified as low frequency inertia-gravity waves as shown by the consistency between the inferred wave parameters and the dispersion relation for low frequency inertia-gravity waves. The ratio of KE to PE in the lower stratosphere is also in agreement with the linear wave theory. Additionally, the momentum flux associated with the waves was estimated by two methods. A first value of total vertical momentum flux of 1.4×10^{-3} to $2.2 \times 10^{-3} \text{ m}^2 \text{ s}^{-2}$ was found using Ern et al's estimate. The second estimate is based on the quadrature spectra of u'_h and T' , giving values of total momentum flux in the range

1.0×10^{-3} to $2.16 \times 10^{-3} \text{ m}^2 \text{ s}^{-2}$. Both estimates are consistent. The corresponding values of zonal momentum flux found are of the same order as values of zonal momentum flux associated with Kelvin waves and thus constitute evidence for the importance of forcing of the tropical circulation by intermediate-scale inertia-gravity waves.

It is not possible to establish the wave source just by using the radiosonde data. Therefore in Chapter 4, we use the WRF model and the ECMWF data to assess the source and mechanisms which led to the generation of the 2-day wave event observed during the campaign.

This portion of the work was published in the *Journal of Geophysical Research* (Evan and Alexander, 2008).

Chapter 4

Model study of intermediate-scale tropical inertia-gravity wave and comparison to TWP-ICE campaign observations.

In the previous chapter, we use radiosonde data acquired during the TWP-ICE campaign to study a 2-day stratospheric inertia-gravity wave (IGW) observed in the Darwin Area. Radiosonde data have the advantage of high vertical resolution so the vertical structure of the waves is resolved accurately. Radiosonde observations usually provide horizontal winds and temperature measurements and thus an estimate of the momentum flux associated with gravity waves (Sato and Dunkerton, 1997). However these estimates are localized while a global distribution of the momentum flux is of interest for the driving of the middle atmospheric circulation. High-resolution satellite data can now provide global distribution of the momentum flux based on temperature measurements (Ern et al., 2004) but this estimate is limited to part of the wave spectrum.

In addition to observational data, analysis data can also be used to study equatorial and gravity waves. Analyses are produced by combining atmospheric observations with a forecast model using data assimilation. These data consist of global fields which describe the 'best' estimate of the atmospheric state. Most of the forecast models used to produce analysis data now have sufficient horizontal resolution to resolve mesoscale to intermediate-scale waves. Recent studies have used the ECMWF analyses to infer the properties of tropical waves.

For instance, Tindall et al. (2006a,b) studied the representation of equatorial waves in the ECMWF 15-year reanalysis dataset (ERA-15) by using wavenumber-frequency spectral analysis and linear wave theory. They showed that the equatorially trapped wave annual and interannual

variability in the ERA-15 data were in agreement with previous studies based on radiosonde or satellite observations. In particular, Kelvin and Rossby gravity wave variations at 50 hPa were correlated with the QBO. However with the limitations in resolution of the dataset, the influence of higher frequency waves on the acceleration of the QBO was more difficult to assess.

Similarly Le Sommer et al. (2006) used the ERA40 reanalysis data to quantify large-scale IGW activity in the equatorial lower stratosphere. They considered IGW activity during December 1992 which corresponds to the TOGA-COARE campaign period. They showed that IGW in the ERA40 data had characteristics similar to the IGW observed during the TOGA-COARE campaign. Moreover, their study demonstrated that large-scale IGW can provide a noticeable contribution to the momentum flux driving the QBO and that this contribution is comparable to momentum flux associated with Kelvin and Rossby gravity waves.

These studies suggest that the ECMWF model has some ability to reproduce gravity wave and equatorial wave activity in the lower stratosphere. The 2-day wave event described in chapter 3 is also observed in the ECMWF data. In this chapter, we will show that the ECMWF data capture similar horizontal structure for this 2-day wave event but with a larger vertical wavelength. This is likely due to the coarse vertical resolution of ECMWF, which we will later show does not properly resolve the vertical structure of the wave event. At the moment, between 20 and 40 km the ECMWF model vertical resolution is around 1.5 km and several studies have shown that a vertical resolution of 750 m or less is necessary to accurately resolve vertically propagating equatorial waves and their interaction with the mean flow (Boville and Randel, 1992; Takahashi, 1996; Giorgetta et al., 2002). Currently the representation of the QBO in analysis data depends crucially on the assimilation of wind measurements from radiosonde observations (Bengtsson et al., 2004).

Unlike operational models, high-resolution global circulation models (GCMs) can simulate a QBO in free running mode (Hamilton et al., 1999, 2001; Kawatani et al., 2010a,b). These GCMs are efficient tools to obtain a complete representation of tropical waves and to assess their role in the driving of the middle atmospheric circulation. However high resolution GCMs with a fine grid spacing in the stratosphere are computationally expensive. Thus regional models such as WRF can

be used as a complement to GCMs or analysis data.

In this chapter we propose to use the WRF model as a complement to the ECMWF data to validate and further understand the structure of tropical gravity waves observed in analysis data. WRF is used with the same horizontal resolution as the operational ECMWF in 2006 while using a finer vertical grid-spacing than ECMWF.

To gain more information on the 2-day wave structure described in chapter 3, we will in this chapter use the ECMWF analyses and forecasts to analyze the 2-day wave observed in the radiosonde data. In addition we conducted a series of WRF simulations to assess the influence of vertical resolution and initial conditions on the wave structure observed in ECMWF.

In section 4.1, we describe the wave analysis in ECMWF. In section 4.2 we use a ray-tracing analysis to identify the wave source. The WRF experiments are described in section 4.3. Section 4.4 discusses the possible mechanisms of the wave generation in the WRF simulations. A summary and conclusions are given in section 4.5.

4.1 Wave analysis in ECMWF

4.1.1 Data

We use the daily global ECMWF analyses at 00, 06, 12 and 18UTC and forecasts at 03, 09, 15 and 21UTC from 21 January to 12 February 2006. We use the data from the ECMWF operational forecasting system. In 2006 the operational model had a T511 spectral resolution, equivalent to a grid size of approximately 40 km. The model had 60 vertical levels from near surface up to 0.1 hPa. The vertical resolution is 1 km at the tropopause and 1.5 km at 25 km. The data set comprises the ECMWF fields of temperature, zonal and meridional winds and geopotential heights. Although operational ECMWF spatial resolution in 2006 was around 40 km the wind and temperature data set we are using have been archived at a regular $1^\circ \times 1^\circ$ grid. The data are analysed between 30°N and 30°S for the entire globe. At each latitude/longitude and height point a temporal linear trend is removed from the entire record to define the time series of perturbations of horizontal velocities

and temperature. The 3-hourly ECMWF perturbations are then analyzed using the S-Transform wavelet analysis described in chapter 2.

4.1.2 Wavelet Analysis.

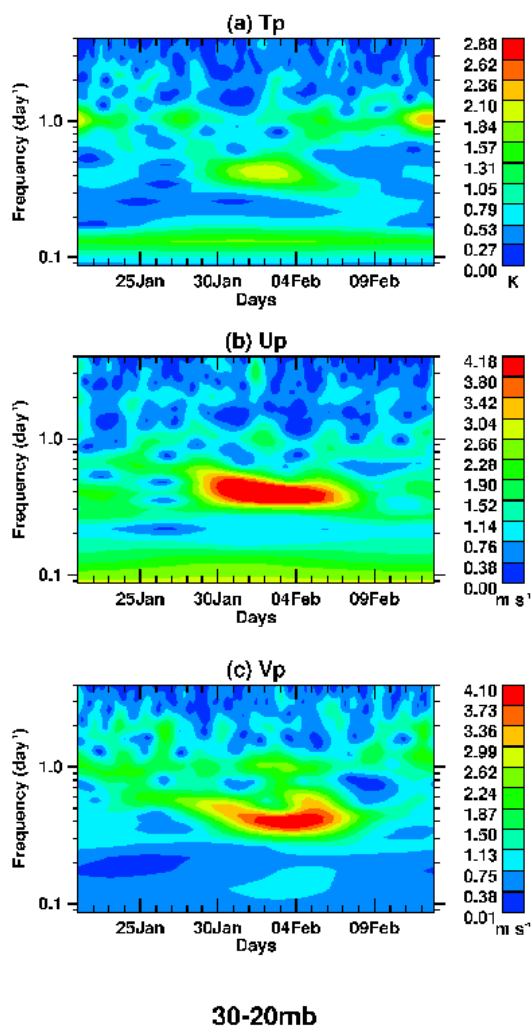


Figure 4.1: Time-frequency spectrum averaged between 30 and 20 hPa for the ECMWF perturbations of (a) temperature, (b) zonal wind and (c) meridional wind observed at $12.5^{\circ}\text{S}, 132.5^{\circ}\text{E}$.

Figure 4.1 shows the average wavelet power spectra between 30 and 20 hPa of time series of perturbations of temperature, zonal and meridional winds at the ECMWF grid box including the

radiosonde sites (12.5°S, 132.5°E). The maximum amplitude corresponds to a period of 2.5 day and is observed from 29 January to 8 February. The wave has larger amplitude in the horizontal winds. We can compare this time-frequency spectrum to the one computed with the radiosonde data of Point Stuart (cf. Figure 3.6 in chapter 3). Both ECMWF and radiosonde data show a ground-based period of 2.5 days. However the amplitudes of the temperature and horizontal wind fluctuations differ from the radiosondes. For instance, the amplitude of temperature fluctuations is greater by a factor of 2 in ECMWF. The amplitudes of the zonal and meridional wind perturbations are greater by a factor of 1.5. This is likely due to the coarse vertical resolution of ECMWF, which we will later show does not properly resolve the vertical structure of the 2.5-day wave. To keep the 2.5-day signal we apply a band-pass filter with cut-off frequencies of 0.3 and 0.6 day⁻¹ (the filter is similar to the one used for the radiosonde data in chapter 3). The larger amplitudes were observed at 20 hPa and thus this pressure level is used to derive the characteristics of the wave event.

4.1.3 Wave properties

To conduct a wave analysis similar to the one described in chapter 3, one needs to combine the data from adjacent radiosonde sites to infer the wave horizontal wavelength. The radiosonde data used in chapter 3 were from a circular network of 4 stations around Darwin with a distance less than 100 km between the stations. The short distance between the stations and the size of the ECMWF grid box do not allow the same wave analysis. Hence we used the cross spectral S-Transform analysis to calculate the mean horizontal wavelength and angle of propagation of the wave observed in the 1.7-3 day range of wave periods. The method used is similar to the one described in Alexander and Barnet (2007). For each analysis time and latitude we first compute the cross S-Transform of adjacent series of filtered zonal wind u' as:

$$CrossST_i(k_x, lon) = S_{u'_i}(k_x, lon) \left\{ S_{u'_{i+1}}(k_x, lon) \right\}^* \quad (4.1)$$

Where lon is the longitude, k_x is the zonal wavenumber, $S_{u'_i}(k_x, lon)$ is the S-Transform of u' at the latitude i . $\left\{ S_{u'_{i+1}}(k_x, lon) \right\}^*$ is the complex conjugate of $S_{u'_{i+1}}(k_x, lon)$, the S-Transform of u' at the latitude $i + 1$. The cross spectral analysis yields the covariance amplitude and phase spectra shift between latitude i and latitude $i + 1$ as:

$$Cov_i(k_x, lon) = |CrossST(k_x, lon)| \quad (4.2)$$

$$\Phi_i(k_x, lon) = \arctan \left[\frac{\Im(CrossST(k_x, lon))}{\Re(CrossST(k_x, lon))} \right] \quad (4.3)$$

Here \Im and \Re refer to the imaginary and real parts of the cross S-Transform. For each analysis time an average covariance amplitude spectrum as a function of k_x is then computed for 4 latitude bands (20-30°S, 0-20°S, 0-20°N and 20-30°N). These latitude bands correspond to different regions of wave activity. Between 20-30°S and 20-30°N the wave activity is weak during the whole period of the campaign whereas strong amplitudes in the horizontal winds can be observed between the equator and 20°N and between the equator and 20°S (not shown). This average covariance amplitude spectrum is given by:

$$Cov(k_x) = \frac{1}{n} \frac{1}{\Delta lon} \sum_{i=1}^n \sum_{lon} Cov_i(k_x, lon) \quad (4.4)$$

$i = 1$ and $i = n$ correspond to the limits of the 4 latitude bands (not shown).

For each latitude band we find the dominant zonal wavenumber and amplitude peaks in $Cov(k_x)$. Then using (3) at each latitude we compute the phase shift associated with these dominant features. The phase shift Φ_i between adjacent series of u' (separated by a distance $\Delta y \approx 110$ km) yields the meridional wavenumber k_y of the dominant features using the formula:

$$k_y = \frac{\Phi_i}{\Delta y} \quad (4.5)$$

Knowing k_x and k_y we can then calculate the amplitude-weighted horizontal wavenumber $k_h = (k_x^2 + k_y^2)^{0.5}$ and wave propagation direction α relative to the west-east direction.

The distributions of k_h and α were determined using both the zonal and meridional wind perturbations.

Figure 4.3 displays the squared amplitude of the wave derived from the quadrature spectrum of the perturbations of zonal and meridional winds at 20 hPa. These amplitudes correspond to an average value over the campaign period. The wave amplitude presents a maximum between 5 and 15°S over a large range of longitudes (0 to 150°E) consistent with the large horizontal wavelength inferred from the radiosonde data.

Figure 4.2 shows the distributions of horizontal wavelengths and angles of propagation associated with the amplitude shown on Figure 4.3. The distributions comprise values of horizontal wavelength and angle of propagation for locations where the wave amplitude is greater than 0.7 times the maximum amplitude.

Also shown on the histograms are the weighted-mean of each distribution. The weights of the average correspond to the magnitude of the quadrature spectrum shown on Figure 4.3. The zonal wind fluctuations have a horizontal wavelength close to the value found for the meridional wind fluctuations (5785 km vs 5516 km). The wave packet identified on Figure 4.3 has thus an average horizontal wavelength $\overline{\lambda}_h$ of 5650 km. Both fields show that the wave is propagating southeastward with an angle of propagation of -43° for the zonal wind fluctuations and of -42° for the meridional winds fluctuations which gives a mean angle of propagation of -42.5°. This

direction is consistent with the angle of propagation of -74° and -47.3° derived with the radiosonde horizontal winds using two different methods: (1) -74° corresponds to the mean direction computed from the phase differences among multiple combination of stations; (2) -47.3° was obtained by the covariance between the velocities and temperature perturbations. We then computed the mean vertical wavelength and mean intrinsic frequency of the observed wave using the linear wave theory. The mean intrinsic frequency is given by:

$$\bar{\omega} = \omega - \overline{u_h} \frac{2\pi}{\lambda_h}, \quad (4.6)$$

The average vertical wavelength is deduced from the dispersion relation for low-frequency inertia-gravity waves as:

$$\bar{\lambda}_z = \left[\frac{1}{\lambda_h^2} \frac{(\bar{\omega}^2 - \bar{f}^2)}{N^2} \right]^{1/2} \quad (4.7)$$

We used a spatial weighted-average value for the horizontal background wind u_h in the direction of propagation of the wave and Coriolis parameter f . The average was done over the same region used to compute the average horizontal wavelength and angle of propagation. u_h was also averaged over the period of the TWP-ICE campaign. $\overline{u_h}$ is equal to -18.4 m s^{-1} , \bar{f} is equal to $-2.479 \times 10^{-5} \text{ s}^{-1}$ and we took $N^2 = 5 \times 10^{-4} \text{ s}^{-2}$ as a typical value of the buoyancy frequency squared in the lower stratosphere. Table 4.1 summarizes the mean characteristics of the wave packet observed in Figure 4.3. The properties of the wave inferred from the radiosonde data are also shown for comparison. The intrinsic period and horizontal wavelength of the wave are underestimated by the ECMWF model by a factor of 1.25 and 1.3 respectively. On the contrary the vertical wavelength derived with the ECMWF winds is overestimated by a factor of 1.5.

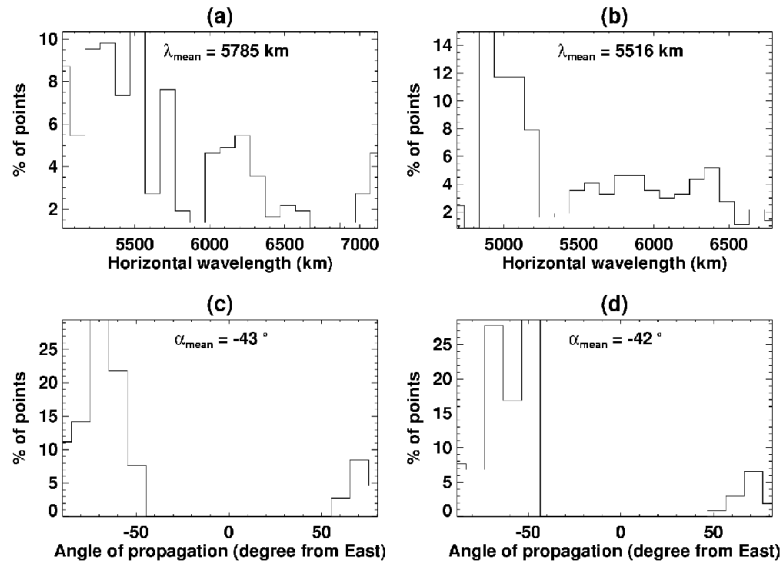


Figure 4.2: (a) Distribution of horizontal wavelengths derived from the zonal wind perturbations. (b) Distribution of horizontal wavelengths derived from the meridional wind perturbations. (c) Distribution of directions of horizontal propagation derived from the zonal wind perturbations. (d) Distribution of directions of horizontal propagation derived from the meridional wind perturbations.

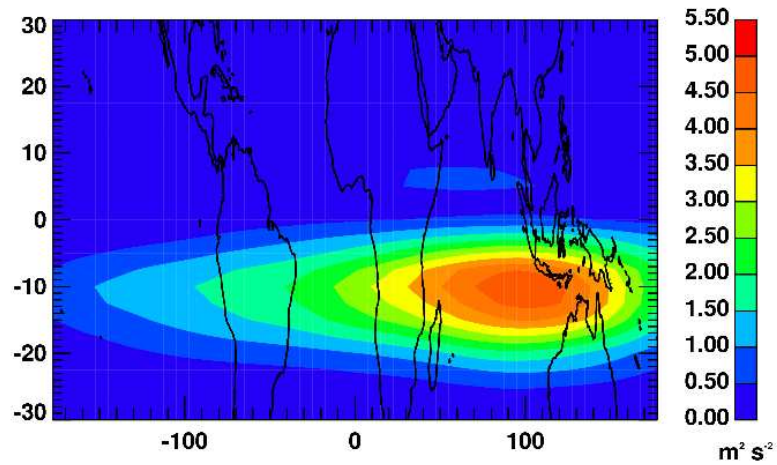


Figure 4.3: Squared amplitude ($\text{m}^2 \text{s}^{-2}$) of the wave observed in the 1.7-3 day range inferred from the quadrature spectrum of meridional and zonal wind perturbations.

Table 4.1: Properties of the wave event derived from the ECMWF fields of zonal and meridional winds at 20 hPa. Also shown are the characteristics of the wave derived from the radiosondes for comparison.

	ECMWF	Radiosondes
$\overline{\lambda}_h$ (km)	5650	7220
Direction of propagation (degree from east)	-42.5	-74 or -47.3 ^a
Intrinsic period (day)	1.6	2
$\overline{\lambda}_z$ (km)	9.3	6
$\overline{u'_h w'}$ ($\times 10^{-3}$ m ² s ⁻²)	3.78	1 to 2
$\overline{u' w'}$ ($\times 10^{-3}$ m ² s ⁻²)	2.79	0.3 to 1.03

^a The two values were derived using different methods. -47.3 is computed by using the covariance between the velocities and temperature perturbations. -74 is computed using the phase shift between adjacent radiosonde sites.

Figure 4.4 shows the longitude-height series of filtered perturbations of temperature and meridional and zonal winds with zonal wavelengths between 4000 and 10000 km. The perturbations averaged between 5 and 15°S are shown on February 1, which corresponds to the period of maximum wave activity. The wave is more active in the longitude band from 40°E to 150°E between 22 and 30 km. The observed vertical wavelength of 8 to 10 km is consistent with the vertical wavelength derived with the linear dispersion relationship. There is a difference in the height of maximum amplitude, which is observed at 28 km in the ECMWF fields and at 24 km in the radiosonde data.

Finally we computed the average total momentum flux associated with this wave event using the quadrature spectrum between the temperature fluctuations and the wind fluctuations along the horizontal direction of propagation (Sato and Dunkerton, 1997). The average total momentum flux is 3.78×10^{-3} m² s⁻² (cf. Table 4.1). This is of the same order of magnitude as the total momentum flux derived with the radiosonde data, although the ECMWF model tends to overestimate the total momentum flux by almost a factor of 2. This can be explained by the fact that the model overestimates the temperature and horizontal wind amplitudes by a factor of 1.5 to 2 and also to the larger 2-day wave vertical wavelength in ECMWF.

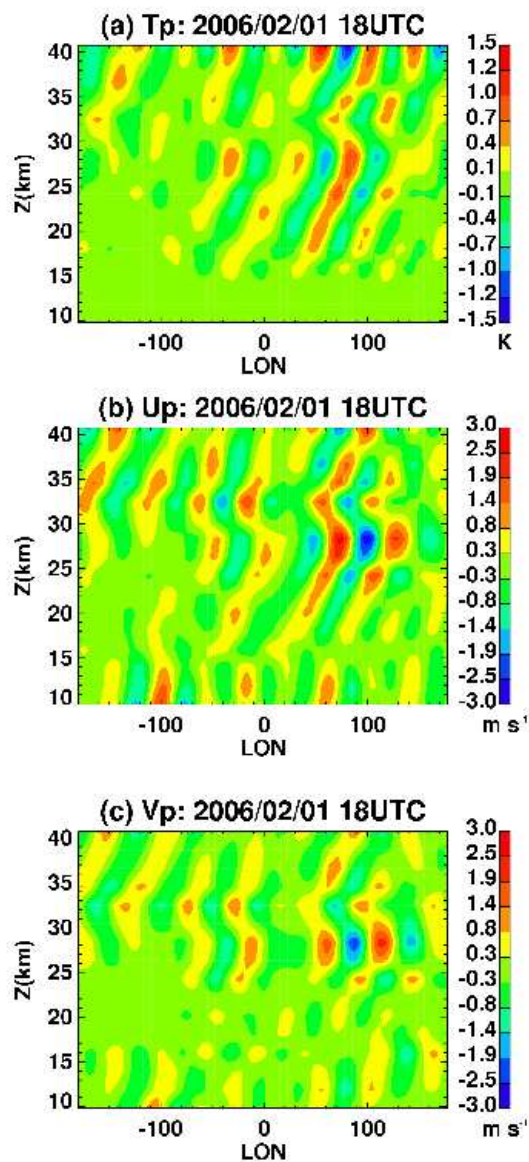


Figure 4.4: Longitude-height series showing the eastward propagating perturbations of (a) temperature, (b) zonal wind and (c) meridional wind observed in the 1.7-3 day range and in the 4-7 planetary wavenumber range. The perturbations are averaged over the latitudes 5-15°S and shown on 02/01/2006 at 18UTC.

4.2 Identification of the wave source

We used the Gravity-wave Regional or Global Ray Tracer (GROGRAT) model to find the source of the observed 2-day wave. The full gravity wave ray-tracing equations used by the model are described in Marks and Eckermann (1995). We briefly summarize here the simplified equations for low frequency IGW

$$\begin{aligned}
 \frac{dx}{dt} &= u + \frac{kN^2}{\hat{\omega}m^2} = u + c_{gx} \\
 \frac{dy}{dt} &= v + \frac{lN^2}{\hat{\omega}m^2} = v + c_{gy} \\
 \frac{dz}{dt} &= -\frac{N^2(k^2 + l^2)}{\hat{\omega}m^3} = c_{gz} \\
 \frac{dk}{dt} &= -k\frac{\partial u}{\partial x} - l\frac{\partial v}{\partial x} \\
 \frac{dl}{dt} &= -k\frac{\partial u}{\partial y} - l\frac{\partial v}{\partial y} - \frac{f}{\hat{\omega}}\frac{df}{dy} \\
 \frac{dm}{dt} &= -k\frac{\partial u}{\partial z} - l\frac{\partial v}{\partial z} - \frac{\hat{\omega}^2 - f^2}{\hat{\omega}N}\frac{dN}{dz}
 \end{aligned}$$

with

$$\hat{\omega} = f^2 + \frac{N^2(k^2 + l^2)}{m^2}$$

where f is the Coriolis parameter, N is the buoyancy frequency and (k, l, m) is the wavenumber vector. $\mathbf{U} = (u, v, 0)$ is the mean background horizontal wind vector, $\mathbf{c}_g = (c_{gx}, c_{gy}, c_{gz})$ is the intrinsic group velocity vector.

The ECMWF data are used to provide the atmospheric background conditions. Zonal and meridional winds and temperature fields are interpolated to a regular grid with a resolution of $2.5^\circ \times 2.5^\circ$ and on 30 vertical levels with a spacing of 1 km between the surface and 30 km. The buoyancy frequency is calculated by the model from the temperature field. The data are averaged over 15 January to 15 February to smooth the winds and temperature fields and remove transient tropical modes from the background.

The initial launch conditions correspond to those estimated from the radiosonde and ECMWF data. 150 rays are launched at 26, 24 and 22 km from the 5 radiosonde sites. The initial angles of propagation α_0 are -45° and -74° and horizontal wavelength between 5000 and 9000 km. In chapter 3 these two different propagation directions were derived using two different sets of assumptions, so we examine each separately. The initial m and $\hat{\omega}$ are calculated using the dispersion relationship of gravity waves. The initial values of m correspond to vertical wavelength between 4 and 8 km (the observed vertical wavelength is 6 km) and the initial $\hat{\omega}$ corresponds to a 2 day period. Backward time integration is carried out with a time interval of 15 min to ensure accurate ray paths.

In GROGRAT the vertical Wentzel-Kramers-Brillouin (WKB) approximation is ensured by the value of a parameter defined by: $\delta = \frac{1}{m^2} \left| \frac{\partial m}{\partial z} \right| \approx \left| \frac{1}{c_{gz} m^2} \frac{dm}{dt} \right|$. δ is used to identify vertical wave reflection. If $\delta \geq 1$ a ray integration is terminated; this is usually the case when $m \rightarrow 0$ or $\hat{\omega} \rightarrow N$. However for low-frequency inertia-gravity waves $\hat{\omega} \ll N$ and m remains finite, thus horizontal reflection dominates vertical reflection. These waves reflect at the critical latitude at which $\hat{\omega} = |f|$. At the critical latitudes $c_{gz} = -\frac{(\hat{\omega}^2 - f^2)}{\hat{\omega}} m$ decreases and this can cause δ to become greater than 1 and an early ray termination. To allow critical latitude reflection we set δ equal to 10. In our case the integration is stopped when the vertical group velocity falls below a minimum value. For low frequency IGW the vertical group velocity is much smaller than the horizontal group velocity and in the present study is order of 10^{-2} m s^{-1} . Therefore we used a minimum vertical group velocity of 10^{-4} m s^{-1} . We expect that the wave observed in the stratosphere originates from deep convective sources so we look for the location and time at which the back trajectory of each ray reaches the 10-15 km height range. The 10-15 km height is the average height range of deep convective clouds in the tropics (Highwood and Hoskins, 2001).

Figure 4.5b shows the locations of the rays for the height range 10-15 km. The majority of the ray paths (78%) are distributed between 15°S and 15°N and 80°E and 180°E . For $\alpha_0 = -45^\circ$ the ray paths originate from areas west of the radiosonde sites while they originate from areas east of the radiosonde sites for $\alpha_0 = -74^\circ$. This difference is due to the fact that with an angle of -74° , the

wave experiences more meridional propagation and horizontal reflection at the northern/southern critical latitudes. The results for the angle of -74° show that the strong easterly wind dominates the westerly c_{gx} (see Figure 4.6c). As a result the ground-based zonal group velocity is westward and indicates a source east of the observation sites (see Figure 4.6a). With an angle of -45° the zonal movement becomes more important and the ground-based zonal velocity is eastward in the troposphere and the stratosphere, which indicates a source located west of the radiosonde sites (see Figure 4.7a). Despite the east/west separation, in most cases the ray paths are confined to the Maritime Continent and Western Pacific regions.

We can identify deep convective areas in the Western Pacific by using brightness temperature of the infrared $11 \mu m$ channel of the Japanese geostationary satellite MTSAT-1R. Figure 4.5a shows the map of daily brightness temperature averaged over 18 January to 27 January, which corresponds to the estimated generation period of the wave. Several threshold temperatures can be used to define deep convection. Mapes and Houze (1993) used 208 K to define large cloud clusters in the Western Pacific. More recently Inoue et al. (2008) used 253 K to identify deep convective areas associated with anvil cloud. In the TWP-ICE mean temperature profile 208 K and 253 K correspond roughly to 14 km and 8 km. Over the Maritime Continent region convective areas are associated with brightness temperature lower than 253 K with the coldest areas observed north of Darwin and west of Sumatra. Convection is weaker between 160 and $180^\circ E$, which corresponds to the region of origin of waves with an initial angle of propagation of -74° in the stratosphere. The weaker convection in this area suggests that the wave is mostly generated from a source to the west of the observing sites and that -45° is a more likely value for wave propagation angle in the stratosphere. From the distribution of brightness temperature and the locations of the rays for the height range 10-15 km we can estimate that the 2-day wave was generated by convection in the Indonesian area.

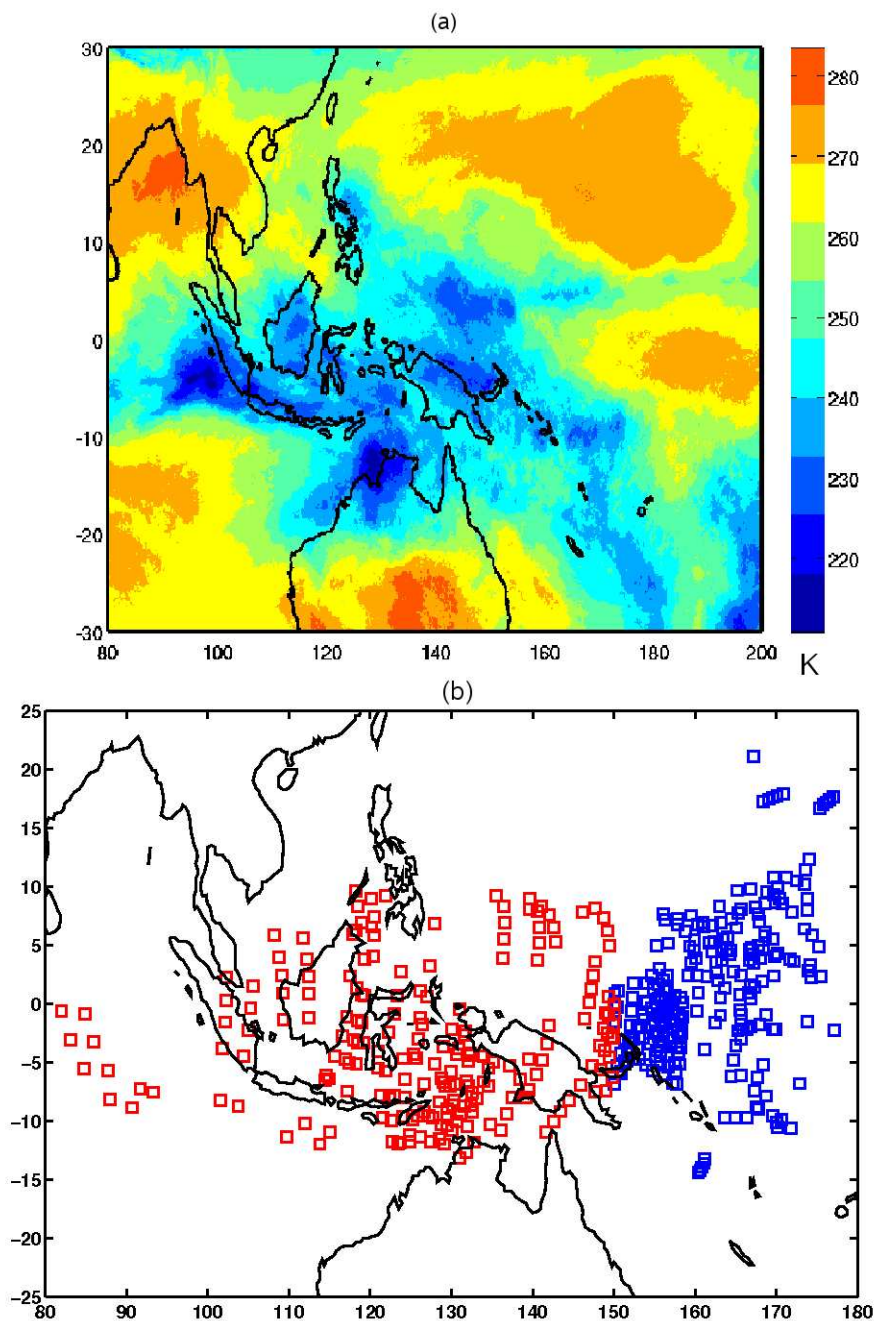


Figure 4.5: (a) Daily average infrared ($11\mu\text{m}$) brightness temperature from MTSAT-1R. Average from 01/18 to 01/27. Areas colder than 253 K correspond to deep convection (Inoue et al., 2008). (b) Final locations of back trajectories in longitude-latitude cross sections for the height range 10-15 km. The red symbols correspond to rays with initial angle of propagation of -45° , and the blue symbols are for initial angle of propagation of -74° .

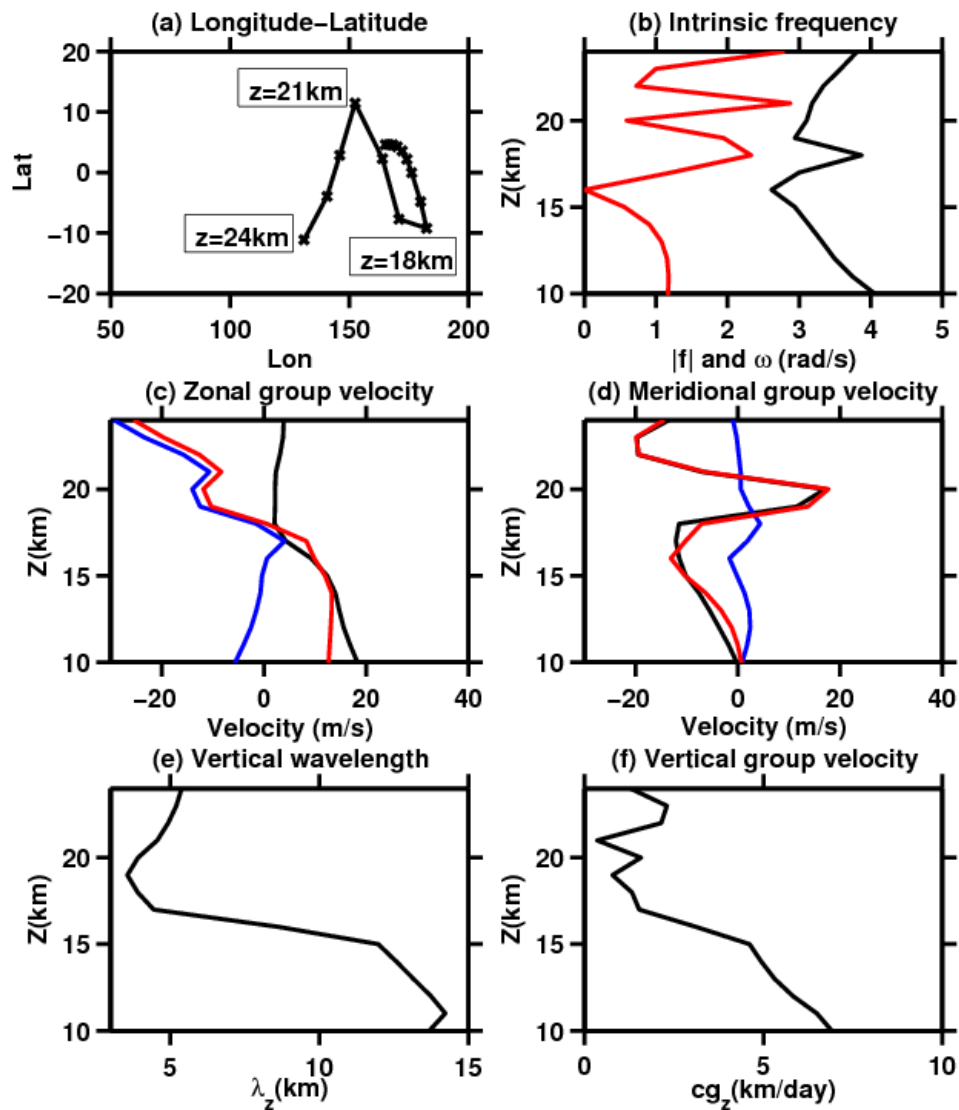


Figure 4.6: Wave parameters obtained from the ray tracing calculations for $\lambda_h = 6500$ km, $\alpha_0 = -74^\circ$: (a) Ray trajectory (b) Intrinsic frequency (black) and absolute value of the Coriolis parameter (red), (c) Intrinsic zonal group velocity (black), zonal wind (blue) and ground-based zonal group velocity (red), (d) Intrinsic meridional group velocity (black), meridional wind (blue) and ground-based meridional group velocity (red), (e) Vertical wavelength, (f) Vertical group velocity.

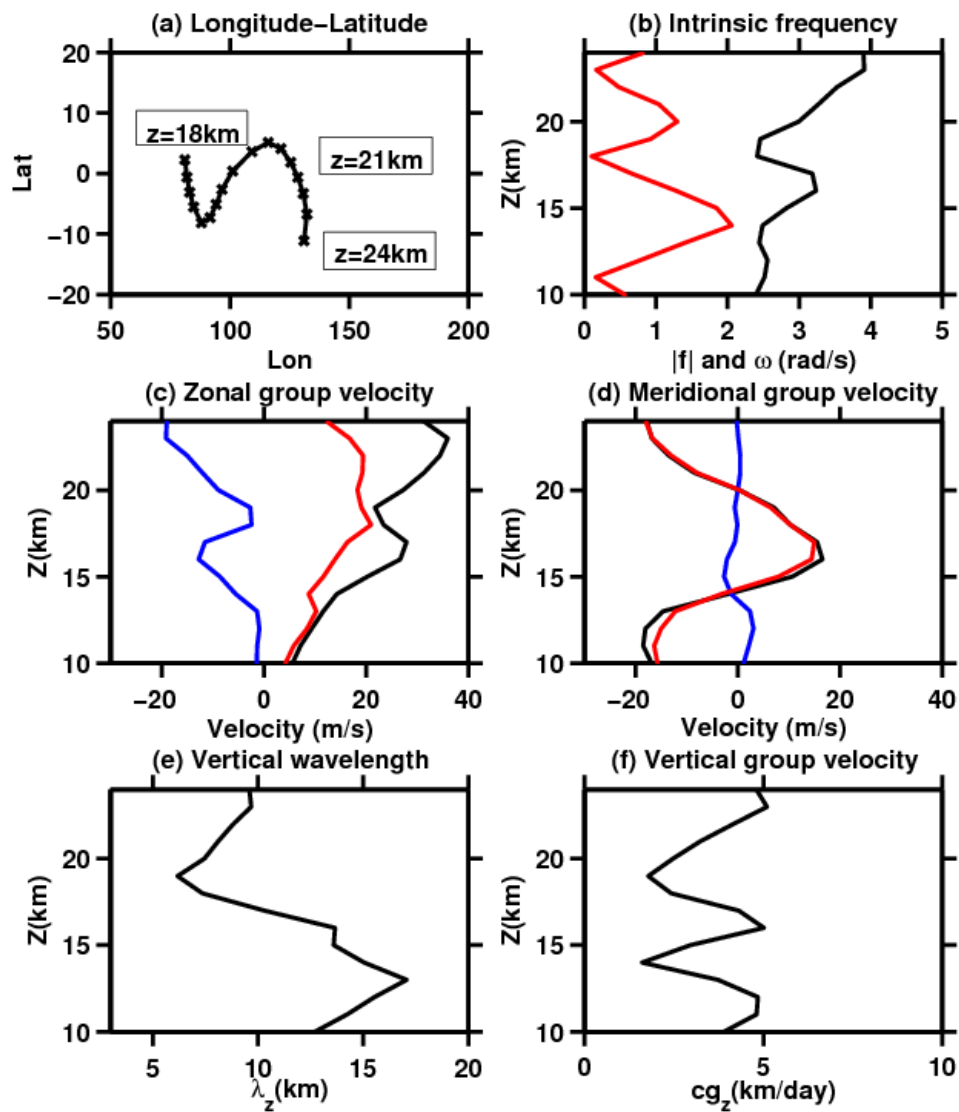


Figure 4.7: Same as Fig. 6., except for $\lambda_h = 6500$ km, $\alpha_0 = -45^\circ$

Table 4.2 summarizes the mean wave characteristics in the upper troposphere for initial angle of propagation of -45° . The mean wave traveling time from the stratosphere to the height range 10-15 km is equal to 7 days and the mean vertical wavelength in the upper troposphere is equal to 14 km. The mean wave propagation direction in the upper troposphere is -21.5° . The intrinsic phase speed distribution has a mean value of 20 m s^{-1} while the mean phase speed relative to the ground is 11.7 m s^{-1} . The effects of background wind are important for the wave propagation condition because of the Doppler effect on the wave. This makes it difficult to estimate the precise wave properties and source in the troposphere. However the ray tracing analysis provides a reasonable estimate of the wave properties near its convective source.

Table 4.2: Mean wave characteristics from the ray tracing analysis for the altitude range 10-15 km. The values correspond to rays with initial angle of propagation of -45° . The wave direction α is expressed in degrees from the West-East direction. The phase speeds and horizontal background wind are in the direction of the wave propagation.

α	-21.5°
\hat{c}_h	20 m s^{-1}
u_h	-8.3 m s^{-1}
c_h^{ground}	11.7 m s^{-1}
λ_z	14 km
λ_h	4000 km
$\hat{\omega}$	$3.456 \times 10^{-5} \text{ s}^{-1}$

4.3 Wave analysis in the WRF simulations

4.3.1 Model and experiments

We use the WRF modeling system version 3.1 described in chapter 2. Table 4.3 summarizes the main physics options used in the simulations. Simulations with two different cumulus schemes are performed. All simulations were performed using a horizontal grid-spacing of 37 km. 84 vertical levels are used from the surface to 1 hPa with a damping layer in the uppermost 15 km. The vertical grid-spacing matches the ECMWF spacing below 5km and is 500 m between 5 and 30 km. The boundary and initial conditions were constructed using the ECMWF analyses and

Table 4.3: Configuration and parameterizations used in WRF experiments.

WRF options	Configuration (Parameterization)
Shortwave radiation	Goddard SW radiation
Longwave radiation	RRTMG LW radiation
Land surface scheme	Unified Noah land-surface
Planetary Boundary Layer scheme	Mellor-Yamada-Janjic
Cumulus scheme	Kain-Fritsch scheme (Mass flux scheme) or Betts-Miller-Janjic scheme (Adjustment scheme)
Δt	45 s
Vertical layers	84 ($\Delta z = 500$ m between 20 and 30 km)
Model top	1 hPa
Damping layer depth	15 km

forecasts. Simulations were carried out globally in a tropical channel with latitudinal boundaries at $\pm 42^\circ$. The model was run during the 24 day period from 18 January to 11 February 2006 to overlap the period of the wave generation and propagation up to the stratosphere. We focus the analysis of the 2-day wave in the stratosphere between 20 and 30 km and on the period from 28 January to 6 February, when the wave is most prominent in the TWP-ICE observations. We also did 4 simulations with different initialization times (20, 22, 24 and 26 January) to evaluate the sensitivity of the wave response to the initial conditions. Model outputs were sampled every 3 hours to match the temporal resolution of ECMWF. For computational efficiency the microphysics is turned-off in the WRF simulations.

4.3.2 Model validation

We use the Global Precipitation Climatology Project (GPCP) one-degree daily precipitation data set to evaluate the WRF simulated daily mean rainfall. Figure 4.8 shows the distribution of daily mean rainfall from 18 January to 28 January 2006 (corresponding to the period of the wave generation). We can see that the model can fairly well locate the position of the ITCZ convection. However excess rainfall is simulated by both cumulus schemes over the Andes and New Guinea. This may be due to the inadequate representation of the topography in the WRF simulations. The circulation near the Andes is difficult to simulate as a result of extreme variations

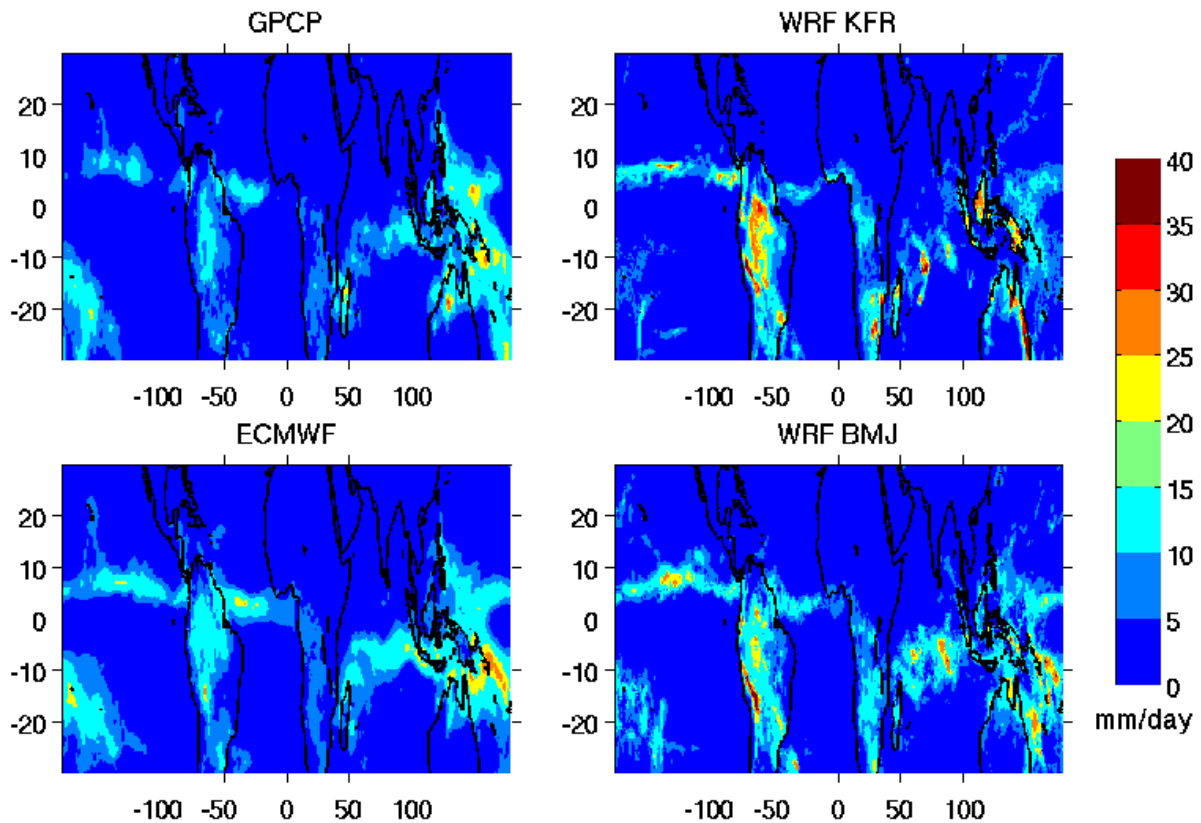


Figure 4.8: Comparison of simulated (right) versus GPCP and ECMWF (left) daily mean rainfall (mm/day) from 18 January to 28 January 2006.

in elevation. In this area, the elevation changes from sea level to about 3000 m in a few grid steps. The simulation using the Kain-Fritsch (KFR) cumulus scheme also shows excessive precipitation near 60°W between the equator and 10°S . In this region the WRF model shows an overestimate of the moisture flux compared to ECMWF (not shown). The tendency for higher moisture in this area may promote stronger convection in the model. As shown by the ray tracing analysis the source of the wave is located in the Indonesian area, thus the overestimation of precipitation over South America is unlikely to influence the model representation of the wave event.

Figure 4.9 shows the Taylor diagram of daily mean precipitation. Taylor diagrams are useful tools to help compare different datasets to one reference dataset, in our case GPCP. ECMWF daily

mean precipitation has good spatial correlations with GPCP. The simulation using the Betts-Miller-Janjic (BMJ) cumulus scheme shows superior skill in precipitation compared to the simulation using Kain-Fritsch.

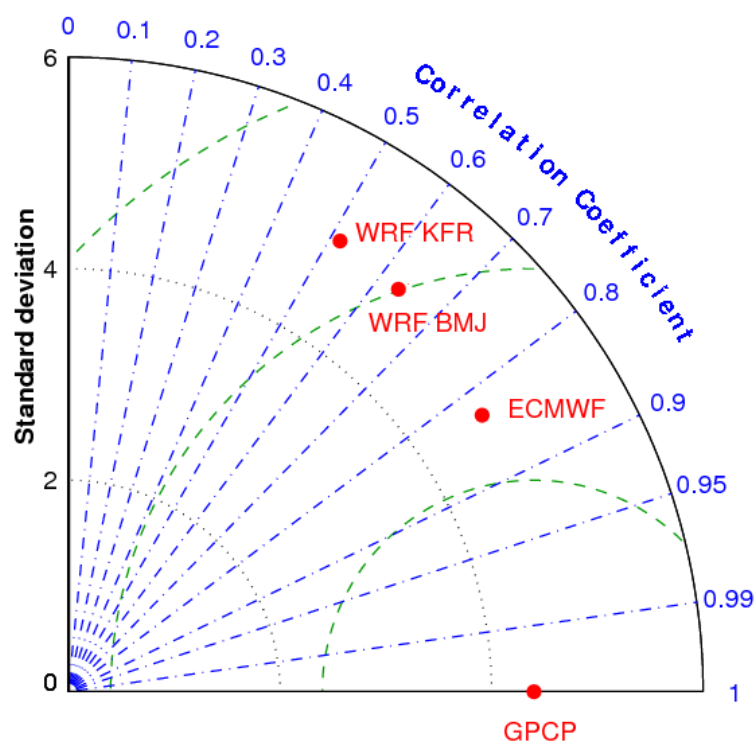


Figure 4.9: Taylor diagram of daily mean precipitation. Each dot represents a 10-day average from 01/18 to 01/28. The position of each dot represents the correlation between observations (GPCP) and model (WRF, ECMWF). The standard deviation of the simulated rainfall is proportional to the radial distance from the origin. The green contours indicate the root-mean-square difference between the simulated and observed rainfall.

Figure 4.10 corresponds to a latitude-pressure cross section of zonal wind averaged over 18 January-6 February 2006 for WRF using the BMJ scheme and ECMWF. WRF is interpolated in the vertical to match the ECMWF resolution for this comparison. The structure of the stratospheric zonal-mean zonal wind is important as it influences the vertical propagation of gravity waves. Overall there is good agreement between the zonal wind structures in ECMWF and WRF. The position and strength of the subtropical jet is realistic in the Northern Hemisphere. In the tropics the model is able to maintain the easterly phase of the QBO observed in ECMWF. The structure of the stratospheric zonal-mean zonal wind in the simulation using the KFR scheme is similar to the simulation using the BMJ scheme and is consistent with the ECMWF zonal wind distribution (not shown).

Figure 4.11 shows ECMWF and WRF-BMJ vertical profiles of buoyancy frequency (N) averaged over the tropical region between 15°S and 15°N . Both profiles were computed using a vertical resolution of 1 km. The ECMWF N^2 profile has a maximum around 20km while the WRF N^2 maximum is at 18km. However both models present a stratospheric mean value of N^2 around $6 \times 10^{-4} \text{ s}^{-1}$. There is a difference of 1 km in the position of the cold point tropopause in ECMWF and WRF (not shown). In WRF the cold point tropopause is located around 16 km whereas it is located around 17 km in ECMWF. In general a cold bias of 1-2 K is observed between 20 and 35 km in WRF (not shown).

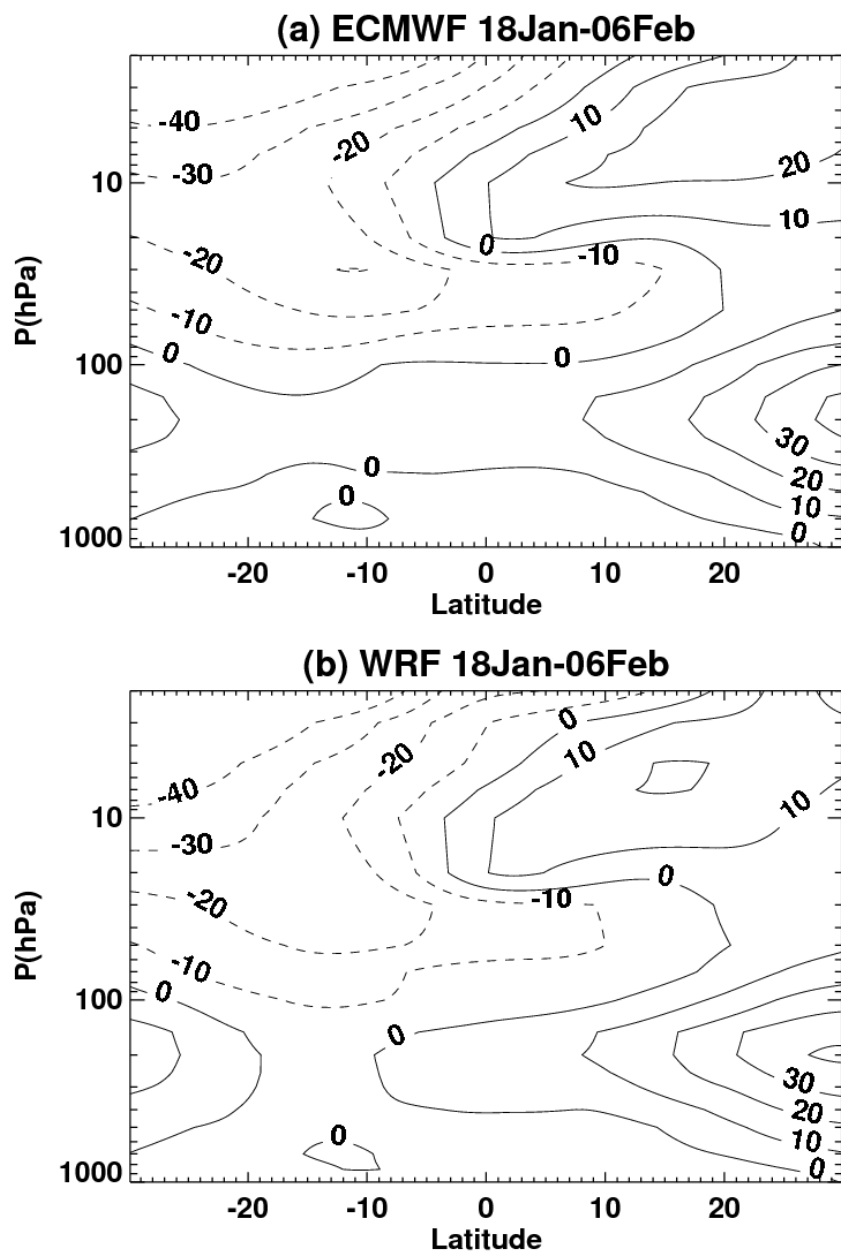


Figure 4.10: Latitude-pressure cross section of zonal wind averaged over 18 January-6 February 2006.

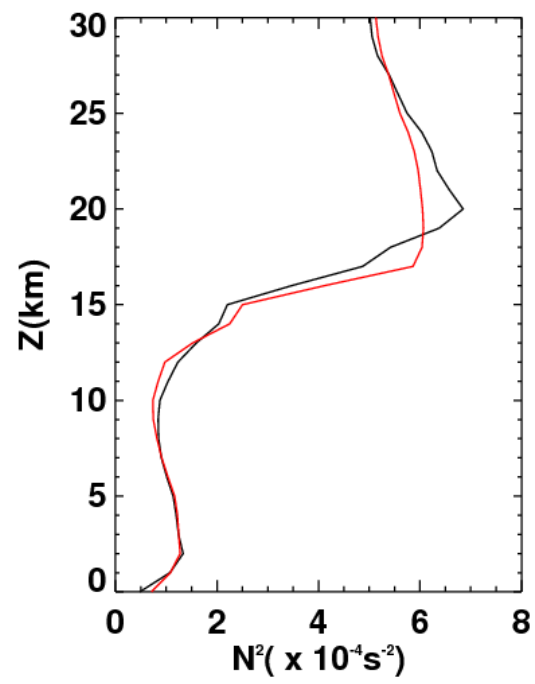


Figure 4.11: Vertical profile of buoyancy frequency averaged over 15°S - 15°N and 18 January-6 February. WRF (red), ECMWF (black).

4.3.3 Wave structure in WRF

Figure 4.12 shows the average of the wavelet power spectra of time series of perturbations for the height ranges 22 and 26 km in the simulation using the BMJ scheme initialized January 18. The spectra are also averaged over the area 120-140°E and 5-15°S. A strong diurnal cycle is observed in the wavelet spectra. The mean amplitude of the diurnal cycle in the radiosonde temperature data was 0.5 K (cf. Figure 3.6 of chapter 3) whereas the mean amplitude is 0.8 K in WRF using the BMJ scheme and 1.2 K in WRF using the KFR scheme (not shown). The mean amplitude of the diurnal cycle in ECMWF is 0.7 K (see Figure 4.1) at the location of the radiosonde sites. Both ECMWF and WRF exhibit nonmigrating diurnal tides in the stratosphere (not shown). Nonmigrating tides can be excited by latent heat release associated with deep tropical convection. Horinouchi et al. (2003) have shown a correspondence between nonmigrating diurnal tide activity in the stratosphere and the diurnal component of precipitation in different GCMs. In WRF and ECMWF the diurnal cycle of convective precipitation is strong compared to observations. This may be due to an overestimation of precipitation over the Amazon, the Maritime Continent and Africa where diurnal cycle of convection is strong (Kawatani et al., 2009).

A wave event corresponding to a period of 2.5 days can be seen between January 29 and February 6 in the zonal and meridional wind perturbations. The maximum amplitude in the winds corresponds approximately to the values observed in the radiosondes ($\approx 2.5 \text{ m s}^{-1}$). The simulation using the KFR scheme does not produce the 2-day wave response in the stratosphere and thus only the results of the simulations using the BMJ are presented hereafter. At each grid point we then applied a band-pass filter with cut-off frequencies at 0.3 and 0.6 day^{-1} to keep the 2.5 day signal. To determine the wave structure, only the zonal and meridional wind perturbations are considered and we applied the same procedure used for the ECMWF perturbations.

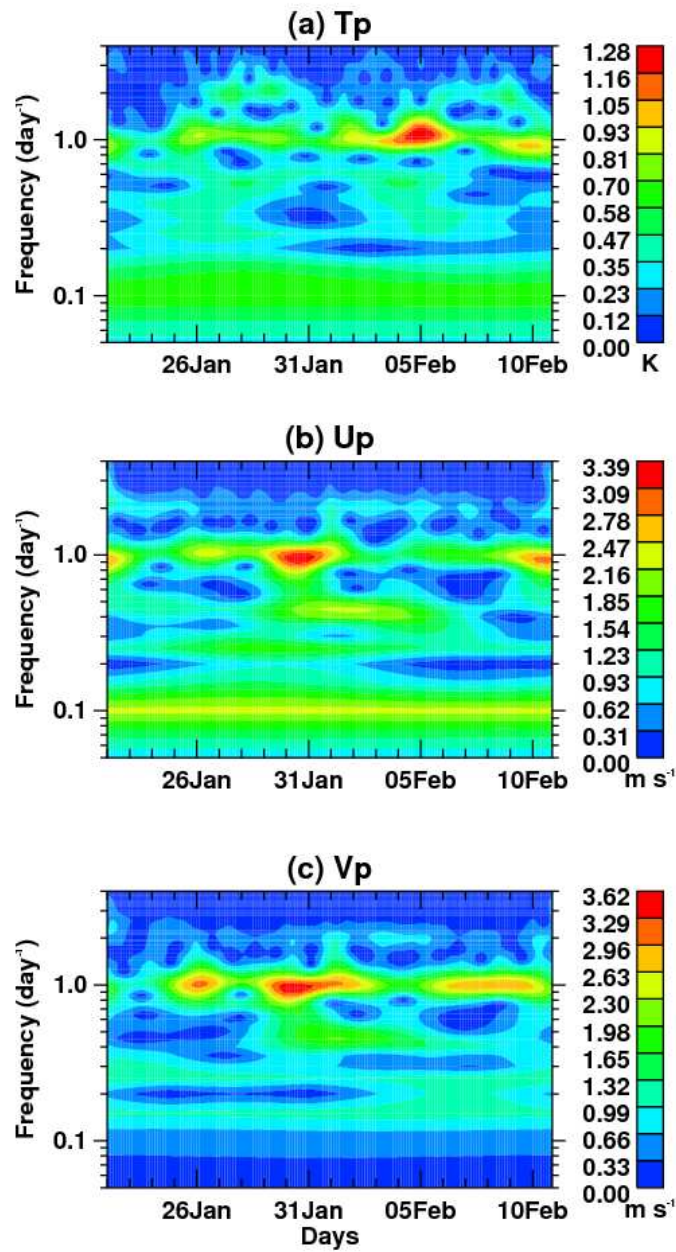


Figure 4.12: Time-frequency spectrum averaged between 22 and 26 km for the WRF perturbations of (a) temperature, (b) zonal wind and (c) meridional wind in the simulation beginning 01/18. The amplitudes correspond also to an average value over the region 120-140°E and 5-15°S.

Figure 4.13 presents the impact of initial conditions on WRF-BMJ representation of the wave event. The influence of the initial conditions can be demonstrated by looking at the wave response in the stratosphere for different initialization times. This is shown on Figure 4.13b-f. On each of these figures, the squared amplitude of the wave is averaged over the same altitude range (30 to 20hPa) and the same period (January 28 to February 6). We use this time period as it corresponds to the period during which the wave is most prominent in the radiosonde and ECMWF data. On Figure 4.13a the wave structure in the ECMWF wind data is shown again for direct comparison with the WRF results. In ECMWF the maximum wave amplitude is observed between 80° - 150° E and 5° - 15° S. In the simulation initialized January 18 (Figure 4.13b) two peaks appear. The first peak is located between 100° W- 10° E and 0° - 10° S. It is unclear what causes this wave response over this part of the domain. However this feature might be a wave response to the model overestimated precipitation in this region. The second peak over the Western Pacific seems to be in agreement with the structure observed in ECMWF.

Figure 4.13c-d show the wave response when WRF is initialized on January 20 and 22 respectively. For these initialization times the model shows less skill in producing the wave structure. The wave amplitude on Figure 4.13c-d is weaker than the wave amplitude shown on Figure 4.13b. This might be due to the fact that the model misses part of the development of the convective sources in the troposphere and thus the model produces an incomplete wave response in the stratosphere.

In the simulations initialized the 24th and 26th of January (Figure 4.13e-f) the model simulates a realistic spatial distribution and amplitude of the wave. In these two cases the wave structure seems to be more similar to the wave structure observed in the ECMWF data. Here the initial conditions in the stratosphere might be such that the model has enough information to reconstruct the wave structure. The results shown on Figure 4.13b-f suggest if the model is initialized soon enough, the model can then develop the convective sources in the troposphere and simulate the wave generation and propagation up to the stratosphere.

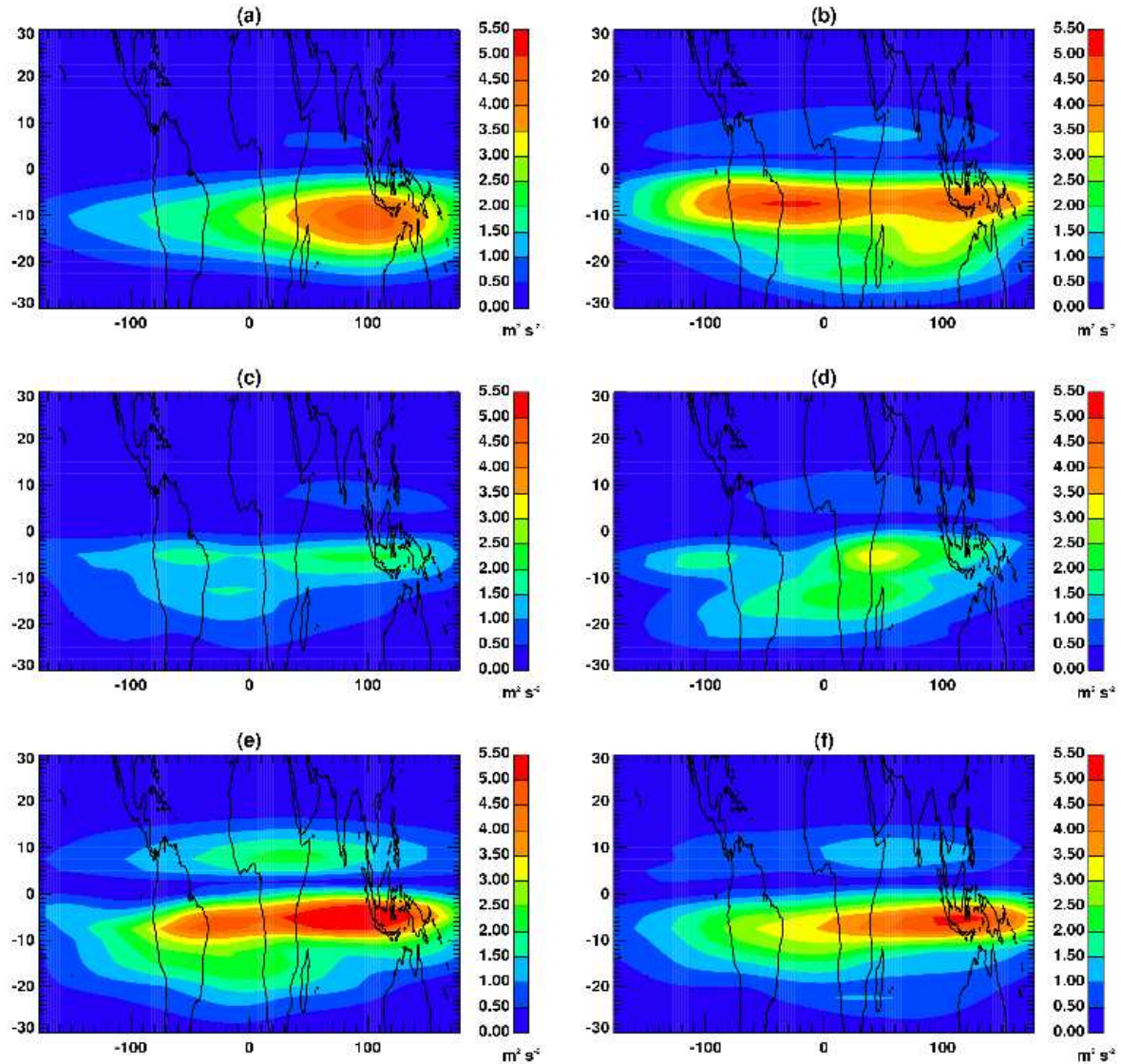


Figure 4.13: Squared amplitude of the 2-day wave inferred from the quadrature spectrum of meridional and zonal wind perturbations averaged between 30 and 20 hPa. (a) ECMWF, (b) WRF simulation beginning 01/18, (c) 01/20, (d) 01/22, (e) 01/24, (f) 01/26. The amplitudes correspond to an average value over 28 January to 6 February.

Table 4.4 summarizes the mean horizontal wavelength and propagation direction associated with the amplitudes shown in Figure 4.13. The values inferred from the radiosonde data are also shown for comparison.

Table 4.4: Mean horizontal wavelength and direction of propagation in the WRF simulations.

Data	λ_h (km)	α (degree from east)
Radiosondes	7220	-47.3 or -74
ECMWF	5650	-42.5
WRF 18 January	4175	-39
WRF 20 January	3622	-46
WRF 22 January	4372	-29
WRF 24 January	5294	-49
WRF 26 January	4655	-32

We use the cross-spectrum between the time series of zonal wind perturbations at a reference height and other altitudes to determine the wave vertical structure. The reference height is 23 km, which is the same value that was used to derive the vertical wavelength in the radiosonde data. Figure 4.14 displays the vertical profiles of phase differences and coherences of u' for a period of 2.5 days in the simulations at Point Stuart. The phase-height relationship is shown for two WRF experiments: the simulation initialized January 18 (WRF18) and the one initialized January 26 (WRF26). To estimate the phase difference the same number of points was used to compute the FFT of u' time series for each altitude. The time series correspond to the zonal wind perturbations from January 26 to February 11 in both simulations. Large coherence can be observed between 21 and 26 km for the simulation initialized January 18. Linear regression analysis is applied to the phase-height relationship between 21 and 26 km, the slope of the regression analysis yields m . The regression analysis indicates that the vertical wavelength of the wave in WRF18 is equal to 5.8 km which is in agreement with the vertical wave structure observed in the radiosonde observations. However the estimated vertical wavelength is equal to 8.6 km in WRF26 which is instead more similar to the ECMWF result. Moreover the coherence between 20 and 28 km is weaker and displays a narrow peak around 23 km. The fact that in WRF26 the vertical wavelength is closer to

what is observed in ECMWF points to an influence of the ECMWF initial conditions in this WRF experiment.

To verify the effect of vertical resolution on the wave structure resolved in WRF, we conducted a simulation which differs from WRF18 by the vertical resolution only (WRF18B). In WRF18B we use the ECMWF vertical grid spacing. In this experiment the vertical grid spacing is around 1 km between 20 and 30 km instead of 500 m in WRF18. In WRF18B the phase-height relationship does not exhibit the wave vertical structure observed in WRF18. This indicates the importance of the vertical grid spacing used in WRF18 which enables an accurate representation of the wave vertical structure.

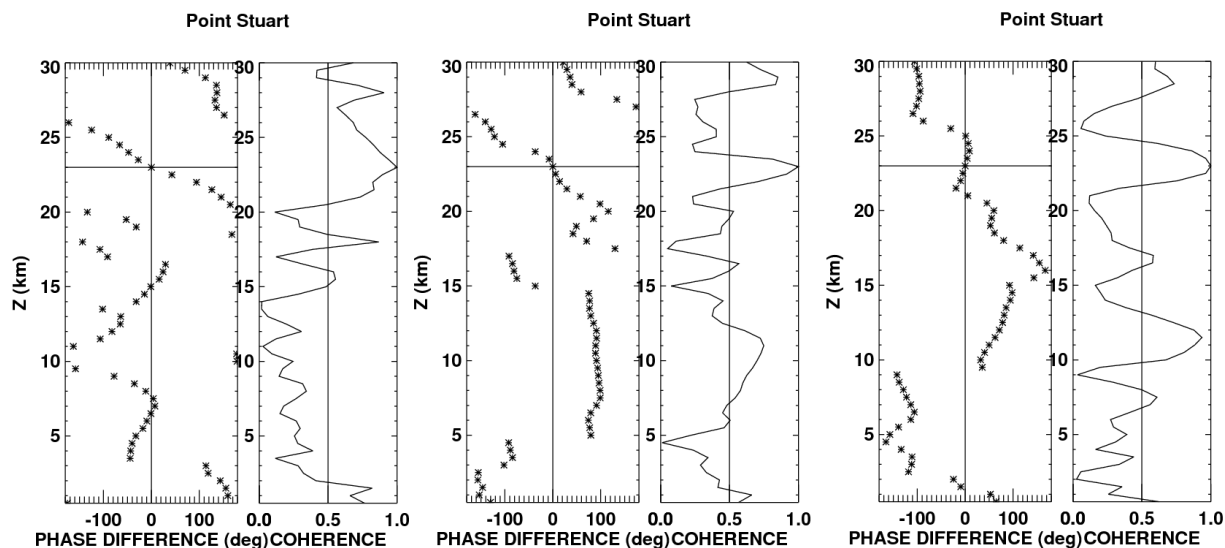


Figure 4.14: Vertical profiles of phase differences and coherences for u for a period of 2.5 days for the simulation initialized January 18 with a grid spacing of 500 m (left), the simulation initialized January 26 with a grid spacing of 500 m (middle) and the simulation initialized January 18 with ECMWF vertical resolution (left).

4.4 Discussion

The ECMWF can capture the overall structure of the intermediate scale inertia-gravity wave. However it is difficult to conclude whether the wave generation is due to the model representation of convection or to the assimilation procedure.

For the tropics and the Southern Hemisphere, radiosonde observations are relatively sparse compared with the Northern Hemisphere, and satellite measurements provide the main source of data for the assimilation procedure. Satellite observations provide mass-field information (information on temperature) from which the wind field is not easily reconstructed in the tropics. Furthermore waves divergent in nature (e.g Kelvin waves) are more easily reconstructed from mass-information compared to rotational waves such as IGW (Žagar et al., 2004). Thus we can estimate that satellite observations assimilated in the model contain little information on the existence of the 2-day wave. There might be a contribution by data assimilated from the few radiosonde sites in the tropical Southern Hemisphere to the wave representation in ECMWF but to a certain degree we can estimate that the wave structure in the analysis and forecast fields relies on model information rather than assimilation. Temperature and humidity data are assimilated in ECMWF which help the model moist physics to produce a rain rate closer to an observed value (Mahfouf et al., 2005). Thus we can assume that the forcing of the wave which is latent heat release in convection is resolved by the ECMWF model but the vertical resolution in the stratosphere is not fine enough to have an accurate representation of the vertical structure of the wave.

This is further supported by WRF simulations. The simulation which starts closer to the wave event does not give an accurate resolution of the vertical structure of the wave. In the simulation initialized January 18, after 10 days we can consider that the model has developed its own dynamics and is no longer dependent on the ECMWF initial conditions.

To understand the link between convection resolved by the model and the wave generation, we examine the evolution of the diabatic heating profiles produced by the cumulus scheme in WRF18. Figure 4.15 displays the time-height section of 3-hourly averaged convective heating averaged over

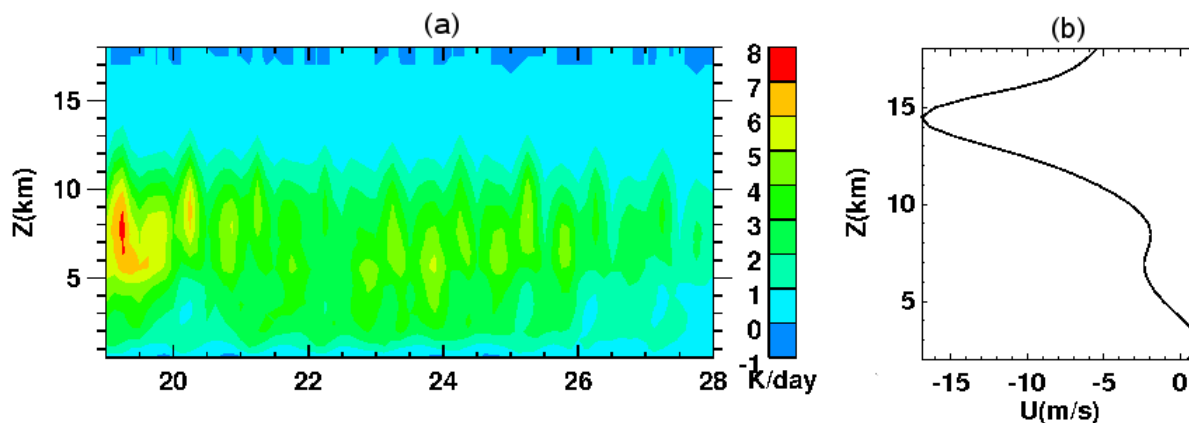


Figure 4.15: (a) Time-height sections of heating rate from the BMJ cumulus scheme for the period of wave generation (01/18 to 01/28). The heating rate is averaged over the region 100-140°E and 10°S-5°N. (b) Vertical profile of zonal wind averaged over the region 100-140°E and 10°S-5°N and 18 January-28 January.

the Indonesian region from January 18 to January 28. In general the top of convective heating is near 12-13 km with a maximum heating level between 5 and 7 km. The mean heating profile for January 18 to January 28 is similar to a deep convective heating profile (i.e. positive throughout the profile) with a depth of 13km (not shown). Significant diurnal variations are seen in the evolution of the simulated diabatic heating. Different regimes of convection were observed during the TWP-ICE campaign. The beginning of the campaign corresponded to the active monsoon during 13-25 January while a suppressed monsoon occurred during 26 January-2 February. This evolution of convection was associated with a strong Madden-Julian Oscillation (MJO) event passing northern Australia during 15-23 January (May et al., 2008). The WRF model seems to capture reasonably well the temporal evolution of convection. The first days of the simulation correspond to stronger convective activity as shown by higher amplitude of heating rate in the mid-troposphere and convection weakens after January 26. The heating profile produced by the BMJ scheme is in agreement with observations of diabatic heating during the TWP-ICE campaign. Xie et al. (2010) used TWP-ICE observational data to derive the diabatic heating profiles associated with convection in the Darwin area. Their mean diabatic heating profile during the active monsoon period showed

a maximum around 6 km with a shape characteristic of deep convection.

On the basis of the heating profile shape and mean value of the wave vertical wavelength in the upper troposphere, one can speculate about the possible generation mechanism of the 2-day wave event in the WRF simulations. Deep heating profiles tend to force fast gravity waves with the heating projecting most strongly on a wave with a vertical wavelength approximately twice the depth of the heating above the source region (Salby and Garcia, 1987; Holton et al., 2002).

The distribution of vertical wavelengths in the upper troposphere derived from the ray tracing (sec. 4.2) shows that 60% of the values are between 10 and 16 km with a mean of 14 km. Near the tropopause, rapid changes in buoyancy frequency with height will cause corresponding changes in vertical wavelength, which can explain the 10-16 km distribution of values. Conversely, the thermal forcing mechanism would predict a peak wave response at a vertical wavelength of 26 km below the tropopause, much longer than any of the ray tracing values, suggesting the thermal forcing mechanism does not explain the observed properties of the wave. Time-dependence and the horizontal scale of the heating can also modify the vertical wavelength of the peak response (Holton et al., 2002; Ortland et al., 2011), so we cannot rule out completely the thermal forcing as a possible generation mechanism of the 2-day wave event.

The interaction of wind shear with convection can also be an effective mechanism to excite upward propagating gravity waves via the obstacle mechanism. This mechanism favors wave propagation opposite to the background wind relative to the convective source and the peak response occurs when the wind amplitude in the frame of reference moving with the source is around 10-20 m s⁻¹ (Pfister et al., 1993; Beres, 2004). This mechanism also predicts the wave to be approximately stationary relative to the convective source if the source varies on a slow timescale. In other words the wave phase speed relative to the ground is similar to the speed of the source.

In WRF18 the background wind at the top of the heating profile averaged over the Indonesian region is westward with an amplitude on the order of -10 m s⁻¹ (see Figure 4.15b). Figure 4.16b shows the longitude-time diagram of WRF18 3-hourly precipitation rates averaged from 10°S to 5°N. A slow eastward-propagating feature can be observed between 110° and 150° from January 18

to January 22. Figure 4.16a shows a similar feature in the Tropical Rainfall Measurement Mission (TRMM) 3-hourly rain rates averaged over the same region. The mean value of wave phase velocity relative to the ground near the source region is 11.7 m s^{-1} in the southeastward direction (-21.5° cf. Table 4.2). This is coherent with the speed of the slow moving convection observed in WRF18 and the direction and amplitude of the background wind at the top of the heating profile. This suggests that the wave observed in the radiosondes is likely forced by the interaction between upper tropospheric easterlies and the slow-moving convection over the Maritime Continent.

An accurate depiction of wave generation by the obstacle effect in numerical models is sensitive to models' representation of vertical wind shear and the depth and propagation of convection. In the tropics a vertical grid-spacing of 1 km may be sufficient to accurately represent the structure of the vertical wind shear and our vertical resolution of 500 m seems to be adequate for this case study. The obstacle-effect mechanism is associated with the most intense convection which usually occurs on scales motion in the range 10-100 km. At a grid-scale of 40 km, the most intense convection is not resolved by the model and needs to be parameterized. This indicates that the representation of the obstacle effect and the generation of intermediate-scale IGW by this mechanism will strongly depend on the choice of the cumulus parameterization used. Here the wave structure with different initialization times suggests that the WRF evolution of the diabatic heating and depth of the diabatic heating is sensitive to the large-scale forcings provided by the ECMWF initial conditions. In particular the initial distributions of temperature and humidity might be an important factor determining the depth of the heating as the top of the convection in the cumulus parameterizations usually corresponds to the level of neutral buoyancy.

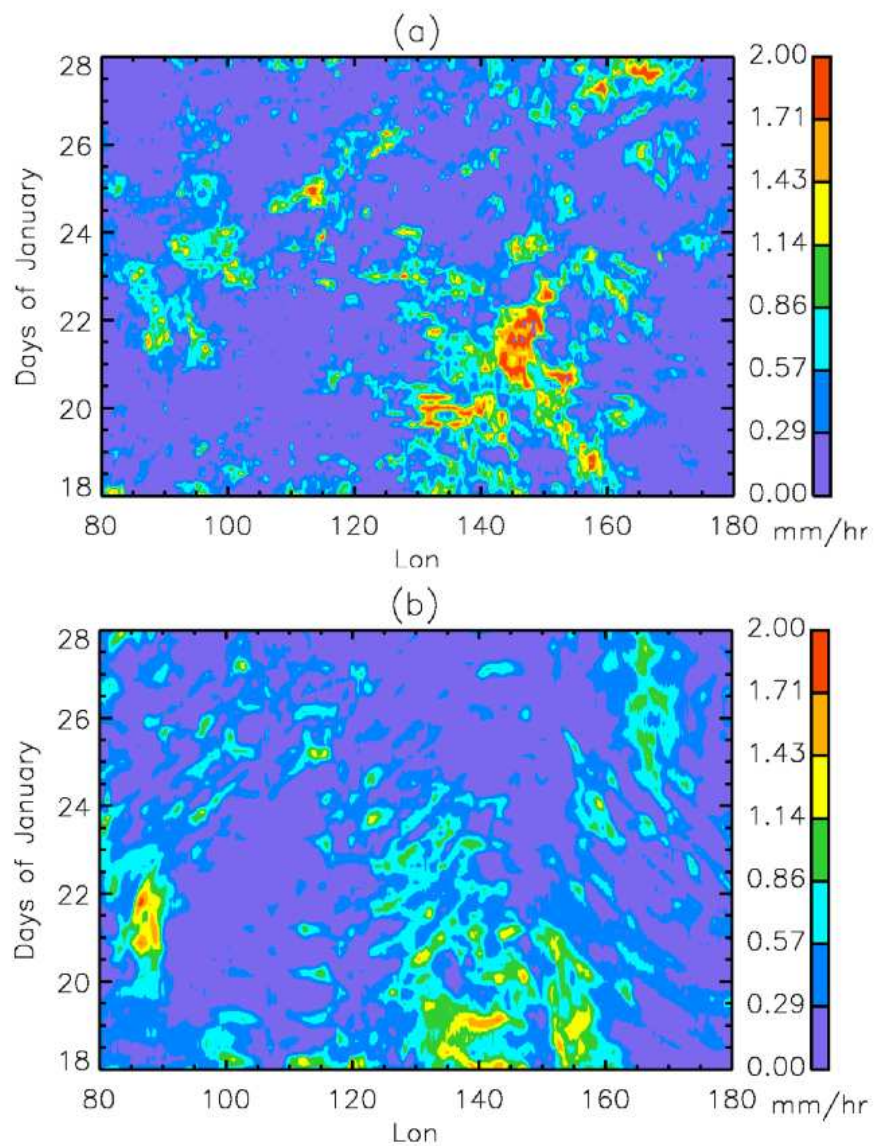


Figure 4.16: Time-longitude section of (a) TRMM and (b) WRF18 3-hourly precipitation rates averaged from 10°S to 5°N.

4.5 Summary and conclusions

Characteristics of a 2-day inertia-gravity wave observed during the TWP-ICE experiment are investigated by using the ECMWF data and the WRF model. Results from the ECMWF data analysis indicate that the ECMWF model overestimates the vertical wavelength of the observed 2-day wave event. This is likely due to the coarse resolution of the model in the stratosphere.

In order to correlate convective sources and the observed wave in the stratosphere, we use a three-dimensional ray-tracing model. The ray-tracing analysis indicates that the mean vertical wavelength of the wave in the upper troposphere (above the convective source) is 14 km and that the ground phase speed of the wave is 11.7 m s^{-1} in the southeastward direction. To gain additional information on the wave generation mechanism we used the WRF model to simulate the 2-day wave event. Different simulations have been performed to determine WRF sensitivity to cumulus schemes, initial conditions and vertical resolution. Among the two cumulus schemes used only the BMJ scheme produces a reasonable spatial distribution of precipitation with a daily variability similar to the observed precipitation. The Kain-Fritsch scheme in our WRF experiments tends to overestimate precipitation over land. More importantly, the BMJ scheme produces a vertical profile of diabatic heating in agreement with diabatic heating profiles observed during the TWP-ICE experiment.

In this study we have also shown that the WRF model is able to maintain the zonal mean state of zonal wind and temperature observed in ECMWF for January-February 2006. This is important for the vertical propagation of waves resolved by the WRF model.

The 2-day wave properties resulting from the WRF experiments have been compared to those retrieved from the radiosonde data and from the ECMWF analyses. The WRF model gives comparable results for the horizontal structure and shows better skill than ECMWF to resolve the vertical structure of the wave.

Our results show that the simulated wave structure is dependent on the initial conditions. The simulation initialized January 18 provides a better resolution of the vertical structure of the wave. The slow ground phase speed of the wave in the upper troposphere (above the convective source)

and the diabatic heating profile in the simulation indicate that the wave is likely generated by the interaction between upper-tropospheric winds and the slow moving convection in the Maritime Continent region via the obstacle effect mechanism.

Generally, the results are encouraging as they imply that the WRF model has the ability to simulate stratospheric gravity waves when run with realistic initial conditions. The increase in vertical resolution leads to a more realistic vertical structure of the 2-day wave compared to the wave structure resolved in ECMWF. This emphasizes the need for a fine vertical resolution in current operational models to accurately resolve the structure of vertically-propagating waves in the tropics and their effects on the middle-atmospheric circulation.

The WRF model has a rapidly growing community of users and is designed for different applications from daily weather forecasting to regional climate modeling. Therefore it is of interest to understand how this model performs in the tropical stratosphere beyond typical day-to-day weather situations. This case study suggests that our configuration of the WRF model has some ability to resolve intermediate-scale inertia-gravity waves generated by convection in the tropics. However, it is necessary to investigate the general properties of other gravity waves in the WRF model results. This will be explored in chapter 5.

This portion of the work is in press in the *Journal of Atmospheric Sciences* (Evan et al., 2011).

Chapter 5

WRF simulations of gravity waves in opposite QBO phases

Chapter 4 has discussed WRF performance in the tropical stratosphere beyond typical day-to-day weather situations. WRF ability to resolve gravity waves generated by convection has also been evaluated with high-resolution radiosonde horizontal wind and temperature measurements of a 2-day inertia-gravity wave event observed during the 2006 TWP-ICE experiment and the ECMWF analysis and forecast data. In this chapter, we use the WRF tropical channel model with a high top to study gravity waves generated by convection for two opposite QBO phases.

A strong motivation for studying gravity waves generated by convection is to understand which portions of the wave spectrum contribute significantly to the forcing of the QBO. This question is still currently unresolved. Traditionally, GCMs have been used to study this issue. However many wave processes cannot be explicitly resolved by GCMs. This is in part because model grid resolution is insufficient to represent the waves and also because the models do not have an accurate representation of convective processes, which are the wave sources in the tropics.

The reanalysis data can provide a good picture of larger scale equatorial waves, but gravity waves will occur on time and space scales smaller than reanalysis data. Therefore gravity wave effects on the QBO are not well resolved in analysis data and their representation of the QBO depends crucially on the assimilation of wind measurements from radiosonde observations.

Here we propose an alternative approach to the QBO problem by using the WRF tropical channel model initialized with the ECMWF Reanalysis Interim (ERA-Interim) data. ERA-Interim consists of a set of global analyses describing the state of the atmosphere and land from 1989 to

present. The main advances in the ERA-Interim data assimilation are a better horizontal resolution, improved model physics and an improvement of precipitation and the stratospheric circulation.

As in the previous chapter, the WRF model has a horizontal grid spacing of 37 km and vertical grid spacing of 500 m and so, in principle, should be able to reproduce much of the tropical gravity wave spectrum. To a large extent, the equatorial waves (Kelvin, Rossby-Gravity and Rossby waves) that represent the low-frequency part of the wave spectrum will be a product of the initialization with the ERA-Interim data. The goal is to provide a new approach to the QBO problem that combines mesoscale model and GCM approaches.

The interaction between gravity waves and the QBO will be discussed. It will be considered whether the gravity waves generated in WRF are affected by the background flow in a way qualitatively consistent with the wave-mean flow interaction theory.

The QBO is also influenced in part by the tropical upwelling of the Brewer-Dobson circulation so an accurate model representation of the QBO requires an appropriate representation of the tropical upwelling. This will also be investigated in this chapter.

Recently, results of a high-resolution GCM simulation by Kawatani et al. (2010a) have indicated that gravity waves contribute at least 50% of the wave driving of the QBO in their model. They also showed that waves with horizontal wavelengths less than 1000 km provide the main westward forcing of the QBO. We will verify this aspect in the WRF simulations. To this aim, the acceleration of the QBO provided by simulated gravity waves will be quantified. We will consider different gravity wave types, i.e. intermediate and small scale gravity waves as well as long and short vertical wavelength waves.

The chapter is organized as follows. Section 5.1 presents the model configuration and data used in this chapter. Sections 5.2 and 5.3 present the mean state and precipitation characteristics of the simulations. Section 5.4 shows the simulated wave response by applying wavenumber-frequency spectral analysis to WRF outputs. Mean flow forcing in the stratosphere for two opposite QBO phases is analyzed in section 5.5. The spectral characteristics of the simulated gravity waves are presented in section 5.6. Finally, the ideas and results of this chapter are summarized in section

5.7.

5.1 Model and data description

WRF version 3.1 is used for this study. All simulations are performed using the Betts-Miller cumulus scheme. To resolve cloud processes the model uses the WRF Single Moment-5 class (WSM5) bulk microphysical parameterization (Hong et al., 2004). The scheme predicts mixing ratios of cloud water, rain, ice, snow and water vapor. No gravity wave parameterization was used in the simulations. The simulations are performed using a horizontal grid-spacing of 37 km. 88 vertical levels are used from the surface up to 0.1 hPa with a damping layer in the uppermost 20 km. We ran WRF for two periods during 2006 and 2007 to investigate the behavior of gravity waves under opposite phases of the QBO. The first simulation was initialized on January 8, 2006 and run for one month. The second simulation was initialized on December 28, 2006 and run until January 26, 2007. These two time periods also correspond to similar regimes of convection.

The ERA-Interim (ERA-I) data are used to provide the initial and boundary conditions. The ERA-I dataset, created by the European Centre for Medium-Range Weather Forecasts, comprises a large amount of reanalysis data covering years 1989-2008. In this study, we use the wind, vertical velocity and temperature fields from ERA-I. The data have been obtained from NCAR on a regular 512x256 Gaussian grid with resolution of $0.7^\circ \times 0.7^\circ$. The data are available 4 times per day on 61 model levels with a top at 0.1 hPa. The vertical grid-spacing varies from 1 km in the upper troposphere to 1.5 km in the lower stratosphere.

Evaluation of WRF model performance involved a comparison of the model results to the ERA-I reanalyses. For the wave analysis, we use WRF and ERA-I data on their original grid. We also use WRF and ERA-I outputs as a function of pressure p . The vertical pressure grid p is converted to a pressure-altitude coordinate z using a constant 7-km scale height, so that $z = -7 \ln(p/p_0)$ with $p_0 = 1000$ hPa. Then for constructing vertical profiles, the data are interpolated onto a vertical grid with a grid spacing of 500 m.

The observed rainfall data used in this study are the TRMM 3B42 rainfall estimates. This

dataset provides 3-hourly rainfall rate at a resolution of $0.25^\circ \times 0.25^\circ$. The TRMM data are further processed to match the WRF rainfall data temporal and spatial resolution. The WRF precipitation corresponding to 3-hourly accumulated rainfall amount from the microphysics and cumulus schemes are also used.

5.2 Mean state

Figure 5.1 shows a time-height cross section of ERA-I zonal mean zonal wind along the equator. This plot shows the evolution of the zonal wind from October 2005 to March 2007. In the stratosphere the QBO is observed between 20 and 40 km. The SAO dominates in the upper stratosphere above 40 km. The period October 2005-June 2006 corresponds to the westerly shear phase of the QBO (i.e $du/dz > 0$) whereas July 2006-March 2007 corresponds to the easterly shear phase of the QBO (i.e $du/dz < 0$). For both periods westerlies and easterlies initially develop at 35 km and then descend to 20 km. The westerlies descend faster than the easterlies. Stalling of the descent of the easterlies is present and starts in January 2007. The dashed lines indicate the periods of the WRF simulations. For both periods, the maximum speed of the westerlies is 10 m s^{-1} between 10 and 15 km.

The mean vertical profiles of zonal wind, temperature and buoyancy frequency squared averaged over the simulation periods are plotted on Figure 5.2. The simulated equatorial zonal winds are in agreement with the ERA-I wind data. In January 2006, the QBO is in its westerly shear phase with the 0 m s^{-1} line at 27 km, while in January 2007, the QBO is in its easterly shear phase with the 0 m s^{-1} line at 25 km. In January 2006, the maximum speed of the westerlies is 10 m s^{-1} at 30 km and the easterlies peak at 23 km with an amplitude of -26 m s^{-1} . In January 2007, between 25 and 35 km, easterly wind dominates with an easterly shear zone below: this corresponds to the transition from the end of the westerly phase to the beginning of the easterly phase of the QBO. In January 2006 the mean tropopause, defined as the cold point tropopause (CPT), was located at 17.5 km with a temperature of 189.1 K in the ERA-I temperature data. In 2006, the WRF model overestimates the CPT temperature by about 3 K and the CPT height is

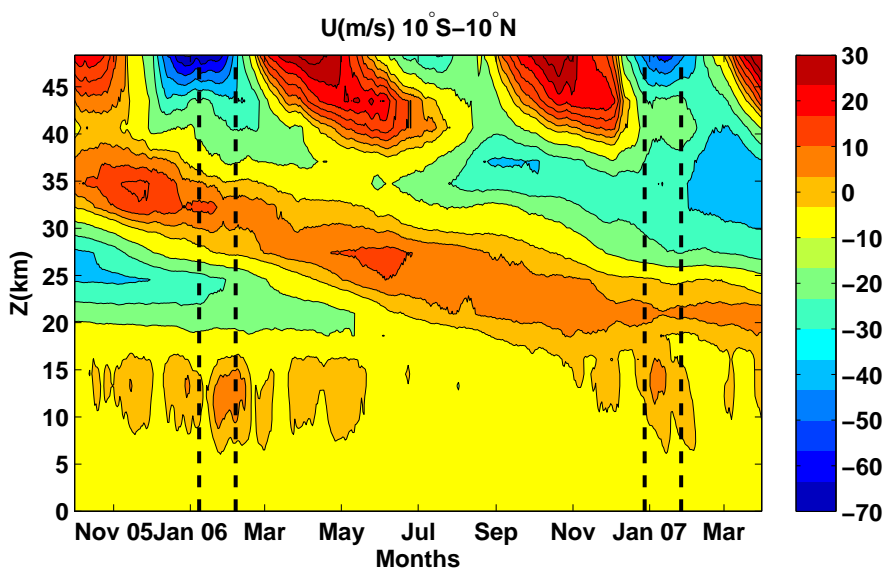


Figure 5.1: Time-height cross section of zonal wind averaged over 10°S-10°N from October 2005 to March 2007. The dashed lines delimit the two simulation periods.

16.8 km. In January 2007, the CPT temperature is 191 K in the ERA-I data versus 193.7 K in WRF. Both datasets indicate a CPT height around 16.5 km. For both years, WRF temperature between 20 and 32 km is colder than ERA-I temperature by about 2-3 K. The reasons for these model deficiencies are not yet clear. Additional comparisons with observational or other reanalysis data would be required to explain WRF representation of the upper tropospheric and stratospheric temperature distributions but this is beyond the scope of this study.

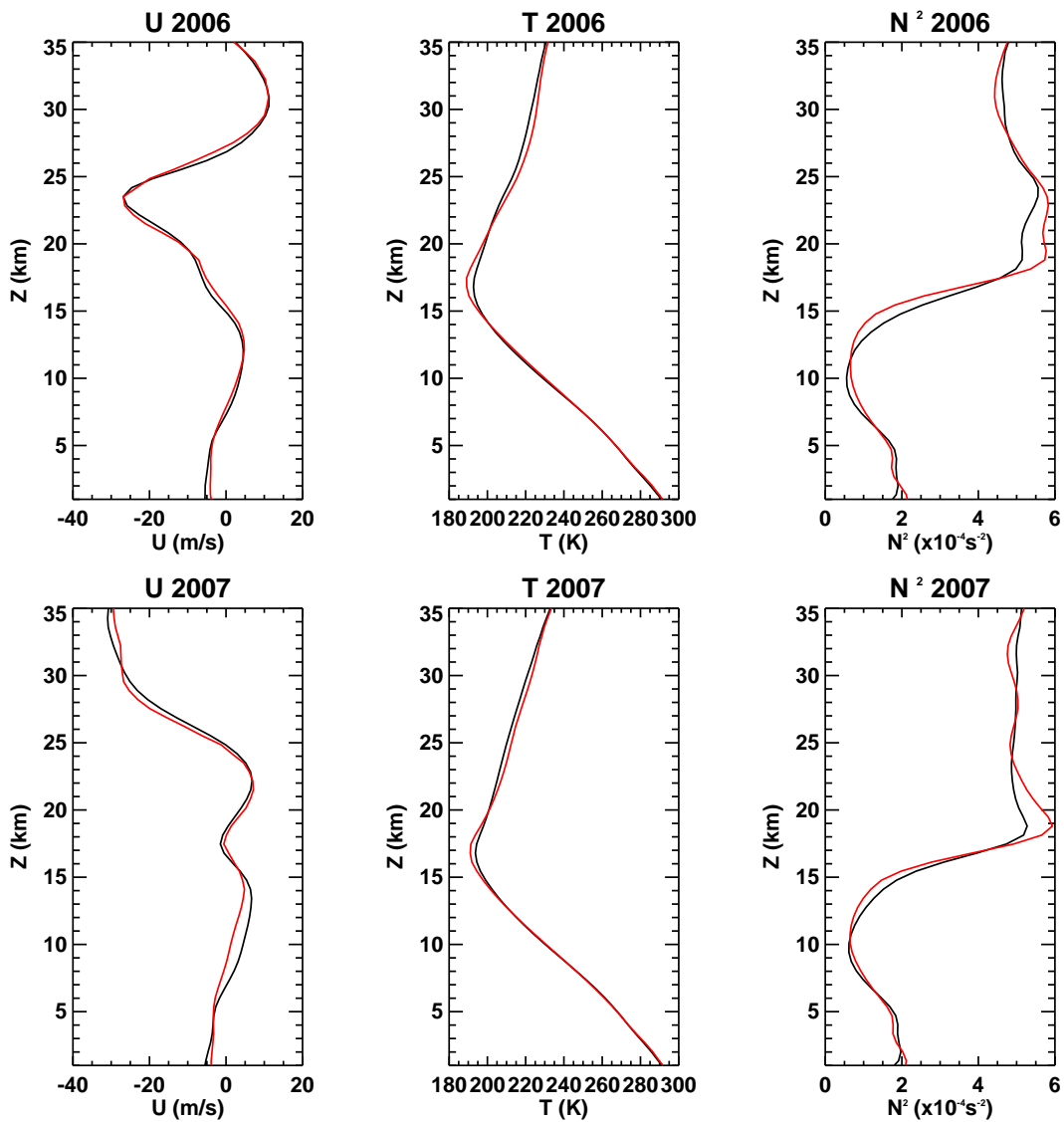


Figure 5.2: Mean vertical profiles of zonal wind (u), temperature (T) and buoyancy frequency squared (N^2) averaged over the tropics (10°S - 10°N). The red curves correspond to ERA-I and the black curves to WRF.

5.3 Precipitation characteristics

Figure 5.3 shows a distribution of model precipitation for January 2006 and January 2007. The observed TRMM precipitation are also shown for comparison. The observed and simulated rainfall show that WRF is able to capture the overall precipitation distribution in the tropics. For both years, deep convective regions are centered south of the equator with maximum precipitation over the Western Pacific and South America. However excess rainfall is simulated over these regions for both years. The Western Pacific region is characterized by considerable convective activity on a wide range of scales from localized thunderstorms up to global-scale intra-seasonal variability associated with the Madden Julian Oscillation (MJO). Accurate representation of precipitation over this part of the world remains a challenge for most GCMs and mesoscale models. It is apparent that the simulated precipitation is higher than observed across most of the Maritime Continent region and especially over the mountains. In this region, the TRMM data indicate that there is more rainfall above land during the evening. Over the Maritime Continent, convection is seen to propagate away from the islands and lead to a peak in convection during the day over the ocean (not shown). WRF captures the overall contrast of land/sea rainfall with a peak over the land during the evening. However over the mountains, the rain starts too early and lasts too long in WRF, especially over New-Guinea (not shown). Most of the islands of the Maritime Continent have mountains higher than 2000 m. With a resolution of 37 km the topography is not well represented in the WRF simulations. This can cause a misrepresentation of orographic precipitation as well as an inadequate representation of small-scale sea-breeze circulations (order tens of kilometers). This could explain in part the model misrepresentation of the organization and development of convection over this part of the world.

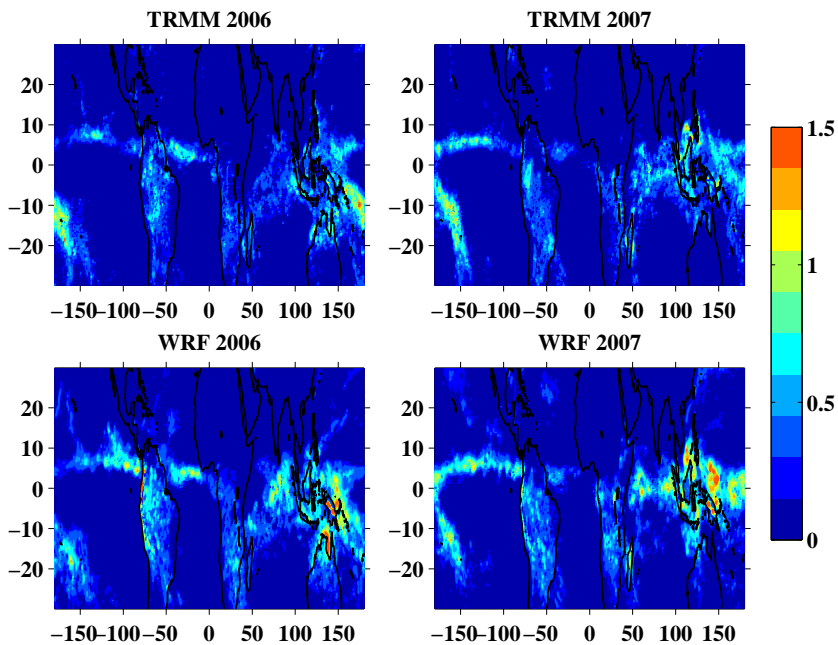


Figure 5.3: Distribution of hourly precipitation (mm hr^{-1}) averaged over the two simulation periods. The TRMM observations are shown on the top panel, the model values are on the bottom panel.

Figure 5.4 shows the zonal wavenumber-frequency spectra of the simulated and observed precipitation variance for January 2006 and 2007 averaged between 10°S and 10°N . The spectra of the TRMM data show that there is considerable variance for frequency less than 2 cpd. The same feature is observed for the WRF precipitation variance. The spectra show variance decreasing with both zonal wavenumber and frequency. WRF and TRMM display a similar decrease in frequency. The precipitation variance at the diurnal frequency is greater in the WRF simulations. Both spectra show enhanced power for spectral components corresponding to phase speed around 10 m s^{-1} . In 2006 most of the westward TRMM variance occurs in the range of -10 m s^{-1} to -20 m s^{-1} . Both spectra indicate enhanced power at westward wavenumbers, but the contrast between westward and eastward propagating components is more pronounced in WRF than in the observations.

Table 5.1 gives mean and variance of precipitation for TRMM and WRF over 10°S - 10°N . The model shows good accuracy in simulating the mean precipitation. Table 5.1 indicates that the BMJ cumulus scheme contributes significantly to the mean total precipitation and that the

temporal variability of tropical precipitation is dominated by the behavior of the microphysics scheme.

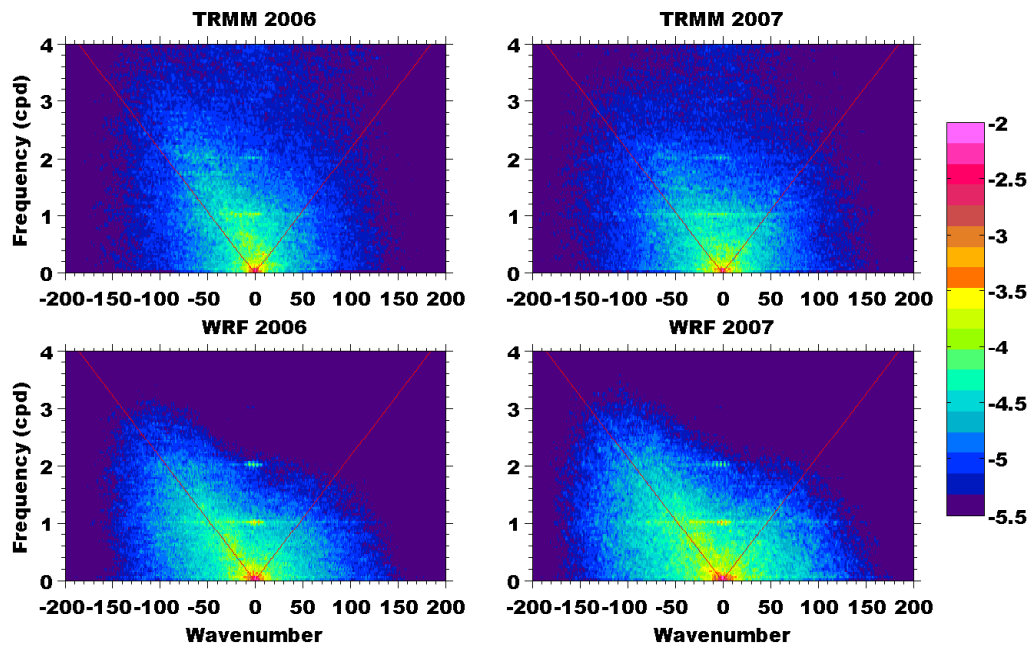


Figure 5.4: Zonal Wavenumber-frequency spectra of TRMM and WRF precipitation variance ($\text{mm}^2 \text{hr}^{-2}$) averaged from 10°S to 10°N . The red lines correspond to phase speed of 10 m s^{-1} .

Table 5.1: The cumulus (BMJ) and microphysics (MP) schemes mean (mm hr^{-1}) and variance ($\text{mm}^2 \text{hr}^{-2}$) of tropical precipitation (10°S - 10°N).

2006	TRMM	WRF total	WRF BMJ	WRF MP
Variance	0.52	0.47	0.19 ^a	0.28
Mean	0.18	0.21	0.13	0.08
2007	TRMM	WRF total	WRF BMJ	WRF MP
Variance	0.50	0.63	0.19	0.46
Mean	0.20	0.20	0.12	0.08

^a The precipitation variance is equal to $0.24 \text{ mm}^2 \text{hr}^{-2}$ in the simulations presented in Chapter 4 when the microphysics is turned-off.

Scinocca and McFarlane (2004) have shown a similar behavior of the Zhang-McFarlane (ZM) scheme used for deep convection in their GCM simulations. Their study indicated that the cumulus scheme and the resolved large-scale stratiform precipitation (LSP) scheme were sensitive to the

setting of the adjustment time scale within the ZM scheme. In the study of Scinocca and McFarlane, with an adjustment time scale of 2400 s, most of the mean tropical precipitation comes from the ZM scheme while most of its variance comes from the LSP scheme. In WRF, the BMJ scheme also uses an adjustment time scale of 2400 s.

Table 5.2 summarizes the values of tropical precipitation variance for different frequency ranges. The low-frequency part corresponds to frequencies less than 1 cpd and the high-frequency part to frequencies greater than 1 cpd. Also shown in the table are the contributions from the cumulus and microphysics schemes to the total precipitation variance. These values are computed by integrating the variance spectra shown on Figure 5.4 over wavenumbers for various frequency ranges. In 2006 the variability is well represented at low frequencies but is overestimated in 2007. For both years the total variance associated with the diurnal frequency exceeds the TRMM values. In 2006 high-frequency modeled precipitation variability is underestimated but is similar to that observed in 2007. The contribution from the microphysics scheme dominates at high frequencies.

Table 5.2: Precipitation variability ($\text{mm}^2 \text{hr}^{-2}$) in the WRF simulations. The values correspond to the TRMM and WRF total variance of precipitation, precipitation associated with the BMJ cumulus scheme and the microphysics (MP) for the frequency ranges $\omega < 1$ cpd (low-frequency), $\omega = 1$ cpd (diurnal) and $\omega > 1$ cpd (high-frequency).

2006	TRMM	WRF total	WRF BMJ	WRF MP
Low-frequency	0.23	0.28	0.12	0.15
Diurnal	0.009	0.012	0.008	0.006
High-frequency	0.28	0.18	0.06	0.12
2007	TRMM	WRF total	WRF BMJ	WRF MP
Low-frequency	0.23	0.38	0.11	0.27
Diurnal	0.008	0.016	0.009	0.009
High-frequency	0.26	0.23	0.07	0.18

5.4 Wave response

We use the Eliassen-Palm (EP) flux as a tool to diagnose the wave activity in the WRF simulations and ERA-I data. The EP theory provides a framework with which to understand the eddy-mean flow interaction. Following Andrews et al. (1987), we express the Eliassen-Palm vector and its divergence as:

$$\begin{aligned}
 F^{(\phi)} &= \rho_0 a \cos \phi \left(\overline{u_z} \frac{\overline{v'\theta'}}{\theta_z} - \overline{u'v'} \right) \\
 F^{(z)} &= \rho_0 a \cos \phi \left\{ [f - (a \cos \phi)^{-1} (\overline{u} \cos \phi)_\phi] \frac{\overline{v'\theta'}}{\theta_z} - \overline{u'w'} \right\} \\
 \nabla \cdot F &= (a \cos \phi)^{-1} \frac{\partial}{\partial \phi} (F^{(\phi)} \cos \phi) + \frac{\partial F^{(z)}}{\partial z}
 \end{aligned}$$

where $F^{(\phi)}$ and $F^{(z)}$ are the meridional and vertical components of the EP flux vector, ϕ the latitude, z is a log-pressure coordinate, ρ_0 the density, f the Coriolis parameter, a the mean radius of the earth. The overbar denotes the zonal average and prime the deviations from the zonal average. For WRF, the zonal mean momentum equation written in terms of the transformed eulerian mean (TEM) framework is:

$$\frac{\partial \overline{u}}{\partial t} = \overline{v^*} [f - (a \cos \phi)^{-1} (\overline{u} \cos \phi)_\phi] - \overline{w^*} \frac{\partial \overline{u}}{\partial z} + (\rho_0 a \cos \phi)^{-1} \nabla \cdot F$$

The TEM residual circulation $(\overline{v^*}, \overline{w^*})$ is an approximation of the Lagrangian mean meridional transport circulation. The total zonal momentum force is given by the sum of the advection terms and the wave forcing associated with the EP flux divergence. The EP flux divergence can be interpreted as the forcing due to waves resolved in the WRF model. EP flux divergence and convergence correspond respectively to eastward and westward accelerations of the zonal mean zonal wind. In the tropics, $F^{(z)}$ dominates $F^{(\phi)}$ and thus is a proxy of vertically propagating waves.

Figure 5.5 displays the zonal wavenumber-frequency distribution of $F^{(z)}$ magnitude averaged between 10°S and 10°N at 100 hPa, 65 hPa and 20 hPa during 2006 and 2007. The level 100 hPa is

selected to show the wave response near the tropopause above the convective source. 65 hPa is used to show the waves entering the stratosphere and 20 hPa corresponds approximately to the zero wind line for both years. In Figure 5.5, positive zonal wavenumbers correspond to eastward propagating waves while negative wavenumbers indicate westward wave propagation. On this plot we show $|F^{(z)}|$ but $F^{(z)}$ is positive at westward wavenumbers and negative at eastward wavenumbers.

The distributions $|F^{(z)}|$ at 100 hPa (~ 16 km) for 2006 and 2007 are fairly similar. $|F^{(z)}|$ is concentrated with phase speeds less than 60 m s^{-1} . The distribution of $|F^{(z)}|$ indicates that the moist processes of the model generate waves with a continuous phase-speed distribution. For eastward wavenumbers the wave response shows waves with frequencies up to ~ 3 cpd while at westward wavenumbers the response is more pronounced at higher frequency. The spectra at 100 hPa present an east-west asymmetry with $|F^{(z)}|$ associated with westward-propagating waves being larger than $|F^{(z)}|$ associated with eastward propagating waves. Previous numerical and observational studies have shown that this asymmetry depends primarily on the wind above the convective source and the source motion (Bergman and Salby, 1994; Beres et al., 2002). For both periods westerlies dominate between 10 and 15 km (see Figures 5.1) and the top of convection is around 12 km for most regions (not shown). This could explain in part the east-west asymmetry of $|F^{(z)}|$ at 100 hPa.

The evolution of $F^{(z)}$ from 100 to 20 hPa is influenced by the interaction of vertically propagating waves with the mean flow. In this process, as a wave approaches its critical level where $c = \bar{u}$, its vertical wavelength and group velocity will become small and the wave will become more susceptible to dissipation.

In 2006, waves with westward phase speeds slower than about -15 m s^{-1} have been absorbed at 65 hPa (~ 19 km). At this level $\bar{u} = -10 \text{ m s}^{-1}$ and the wave vertical group velocity can become small as a result of the buoyancy frequency increase near the tropopause. In 2007 the zonal mean zonal wind magnitude is 1 m s^{-1} at 65 hPa. However easterlies are present between 100 and 70 hPa in the Eastern Hemisphere with the strongest wind, about -10 m s^{-1} , above the Maritime Continent. Therefore the winds in this region will filter the slower westward propagating waves

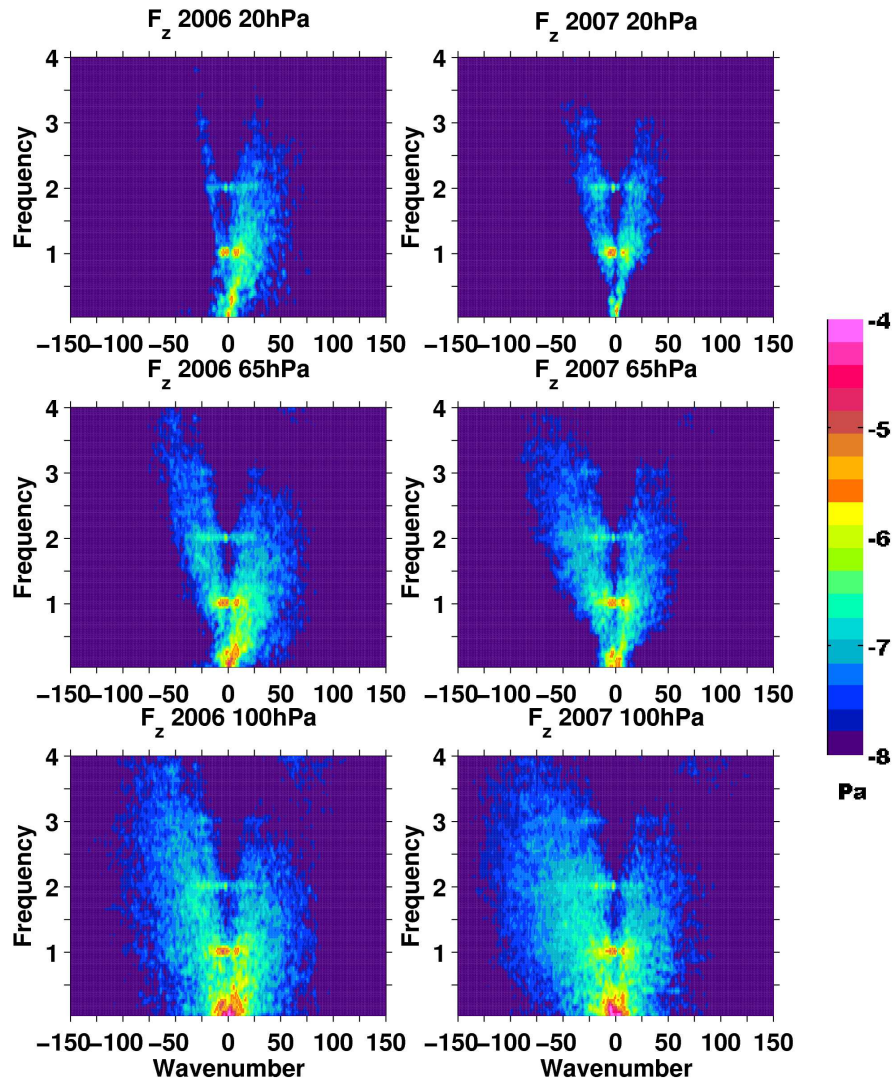


Figure 5.5: Zonal wavenumber-frequency spectra of $|F^{(z)}|$ (\log_{10} Pa) averaged from 10°S to 10°N . The distributions correspond to 2006 (left) and 2007 (right) at 100hPa (top), 65hPa (middle) and 20hPa (bottom).

in their upward propagation. In 2006, westward propagating waves are even more dissipated at 20 hPa (~ 27 km) as a result of the easterly wind speed of ~ -25 m s $^{-1}$ at 23 km. In the easterly shear phase year of 2007 there is less eastward propagating wave flux due to the westerlies between 20 and 25 km. From Figure 5.5, we can see that filtering of upward propagating waves by the zonal wind leads to the spectral distribution of $|F^{(z)}|$ in the stratosphere. The wave-mean flow interaction is well represented in the model for both QBO phases.

Figure 5.6 shows the frequency distribution of $|F^{(z)}|$ at 65 hPa. The frequency distribution is obtained by summing over zonal wavenumbers. The distribution is presented in area-preserving format, i.e. frequency times $|F^{(z)}|$ versus log of frequency so that the area under the curve for two frequencies is equal to $|F^{(z)}|$ in that interval. At negative frequencies the distribution of $|F^{(z)}|$ shows a large contribution from $|\omega| > 0.3$ cpd. Consistent with Figure 5.5 the lower frequency modes at 65 hPa have been filtered by the upper tropospheric winds. At positive frequencies the contribution from high-frequency waves is also important, although more $|F^{(z)}|$ is observed in 2006 at low frequencies. This is because the easterlies between 15 and 27 km are favorable to slow eastward propagating waves. The distribution of $|F^{(z)}|$ shown on Figure 5.6 is in agreement with previous studies which indicated a large contribution to $F^{(z)}$ from gravity waves in the stratosphere, particularly from westward waves (Horinouchi and Yoden, 1998; Hamilton et al., 2001; Kawatani et al., 2010a).

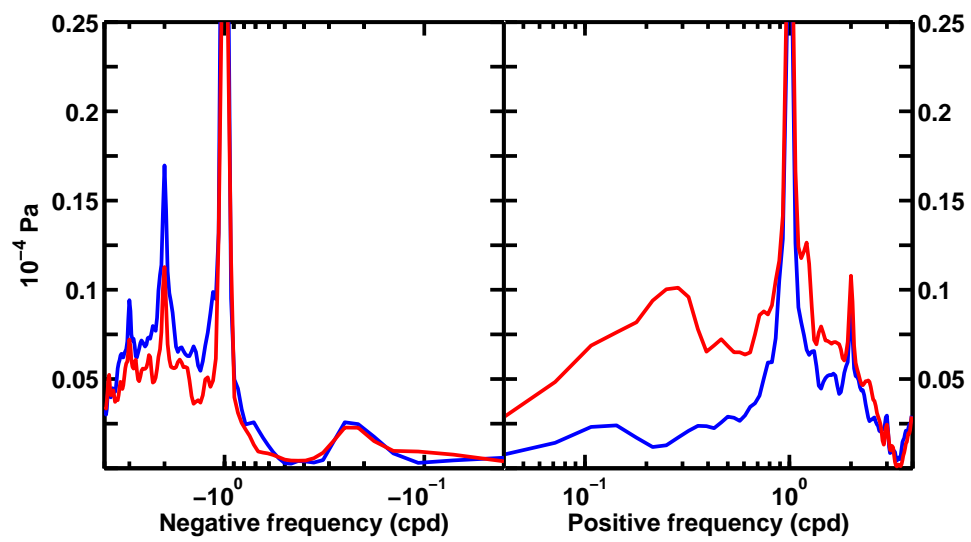


Figure 5.6: Vertical component of the EP flux $|F^{(z)}|$ (Pa) as a function of frequency at 65 hPa for 2006 (red) and 2007 (blue).

The contributions from low-frequency waves ($|\omega| < 0.3$ cpd) and high-frequency waves ($|\omega| \geq 0.3$ cpd) to $F^{(z)}$ at 100 and 65 hPa are listed in Table 5.3. The low-frequency modes would correspond to westward propagating Rossby waves and eastward propagating Kelvin waves. The low-frequency modes in the WRF simulations come from the ERA-I data used to initialize the model. The frequency band $|\omega| \geq 0.3$ cpd can be associated with gravity-waves which are generated in the WRF simulations. For the westerly shear phase of the QBO (2006) the total $|F^{(z)}|$ at 100 hPa is similar for low and high frequency modes. The west-east asymmetry indicated on Figure 5.6 is observed for both frequency bands with more $|F^{(z)}|$ for westward waves. At 65 hPa the slow westward-propagating modes have been strongly absorbed. The contribution from low-frequency eastward modes is smaller than $F^{(z)}$ associated with eastward propagating gravity waves. $|F^{(z)}|$ carried by gravity waves is equal to 0.98 mPa and accounts for 67% of $|F^{(z)}|$ due to all waves.

The same situation is observed for the easterly shear phase of the QBO (2007) although most of the low frequency modes have been absorbed at 65 hPa and only the contribution from gravity waves remains. $|F^{(z)}|$ from gravity waves at 65 hPa is weaker than that of 2006 but accounts for 82% of $|F^{(z)}|$ due to all waves.

Table 5.3: $F^{(z)}$ (mPa) at 65 and 100 hPa for 2006 and 2007

2006 (100hPa)	$F^{(z)}$ Westward	$F^{(z)}$ Eastward	Total $ F^{(z)} $
$ \omega < 0.3$ cpd	0.77	-0.61	1.38
$ \omega \geq 0.3$ cpd	0.85	-0.62	1.42
2006 (65hPa)	$F^{(z)}$ Westward	$F^{(z)}$ Eastward	Total $ F^{(z)} $
$ \omega < 0.3$ cpd	0.06	-0.41	0.47
$ \omega \geq 0.3$ cpd	0.42	-0.56	0.98
2007 (100hPa)	$F^{(z)}$ Westward	$F^{(z)}$ Eastward	Total $ F^{(z)} $
$ \omega < 0.3$ cpd	2	-0.96	2.96
$ \omega \geq 0.3$ cpd	1.1	-0.47	1.57
2007 (65hPa)	$F^{(z)}$ Westward	$F^{(z)}$ Eastward	Total $ F^{(z)} $
$ \omega < 0.3$ cpd	0.08	-0.09	0.17
$ \omega \geq 0.3$ cpd	0.45	-0.35	0.80

5.5 Wave forcing of the QBO.

5.5.1 Zonal wind evolution

The evolution of WRF and ERA-I mean zonal winds in 2006 and 2007 is shown on Figure 5.7. The black curves correspond to the beginning of the WRF simulations. The winds 15 days and 30 days later are shown in blue and red respectively.

In 2006 the westerly jet is initially at 32 km with an amplitude of $\sim 10 \text{ m s}^{-1}$ and descends at a rate of about 1.5 km/month in the WRF simulation. During the descent the peak jet speed is maintained in WRF but slight decreases in ERA-I. This reduction is consistent with the evolution of the zonal wind shown in Figure 5.1. Figure 5.1 indicates that the acceleration of the westerlies in ERA-I above 30 km mainly occurs from October 2005 to the middle January 2006 and is weaker after that. The descent of the jet speed in WRF indicates that there are enough eastward waves in the model to maintain the westerly shear phase of the QBO.

In 2007 easterly winds strengthen above 29 km in WRF and above 27 km in ERA-I. Above 30km the westward acceleration is stronger in WRF than ERA-I. The mean westward acceleration between 30 and 35 km is $-4.4 \text{ m s}^{-1}/\text{month}$ for WRF and $-2.9 \text{ m s}^{-1}/\text{month}$ for ERA-I. Figure 5.7 indicates that in January 2007 the WRF model has also sufficient westward waves to develop the easterlies.

Currently the representation of the QBO in analysis data depends crucially on the assimilation of wind measurements from radiosonde observations (Bengtsson et al., 2004). Therefore we also compare the evolution of WRF simulated QBO winds with vertical zonal wind profiles from Singapore (103.98°E, 1.36°N). Even if this dataset is from a single location it can be representative of the QBO in the equatorial belt since previous studies have shown that longitudinal differences in the phase of the QBO are small (Baldwin et al., 2001). This dataset provides monthly mean zonal wind profiles calculated from daily radiosonde observations at Singapore. The monthly mean zonal wind components are provided at 15 pressure levels between 100 and 10 hPa that we convert to pressure-height. This dataset is described in more details in Naujokat (1986). Figure 5.8 presents

monthly mean vertical profiles of zonal winds for January/February 2006 and 2007. In 2006 the maximum amplitude of the westerlies is $\sim 15 \text{ m s}^{-1}$ between 27 and 32 km. The easterlies between 20 and 25 km are stronger with an amplitude of $\sim -30 \text{ m s}^{-1}$. Between January and February 2006 the westerlies move down at a propagation rate of about 1.5 km/month. The peak of westerlies is conserved during the downward propagation and is consistent with the evolution of WRF and ERA-I zonal wind from January to February 2006.

In 2007 the easterlies accelerate above 28 km from -25 m s^{-1} to -31 m s^{-1} . The strengthening of the easterlies in WRF is thus in agreement with that observed in the Singapore data. The mean westward acceleration in WRF is close to the radiosonde estimate ($-4.4 \text{ m s}^{-1}/\text{month}$ for WRF versus $-6 \text{ m s}^{-1}/\text{month}$ for the radiosonde data).

Figure 5.7 and Figure 5.8 suggest that the QBO zonal wind evolution is fairly well represented in WRF. The simulated QBO winds will depend on the model representation of mean tropical upwelling $\overline{w^*}$ and wave forcing. Thus we examine both factors in the subsequent sections.

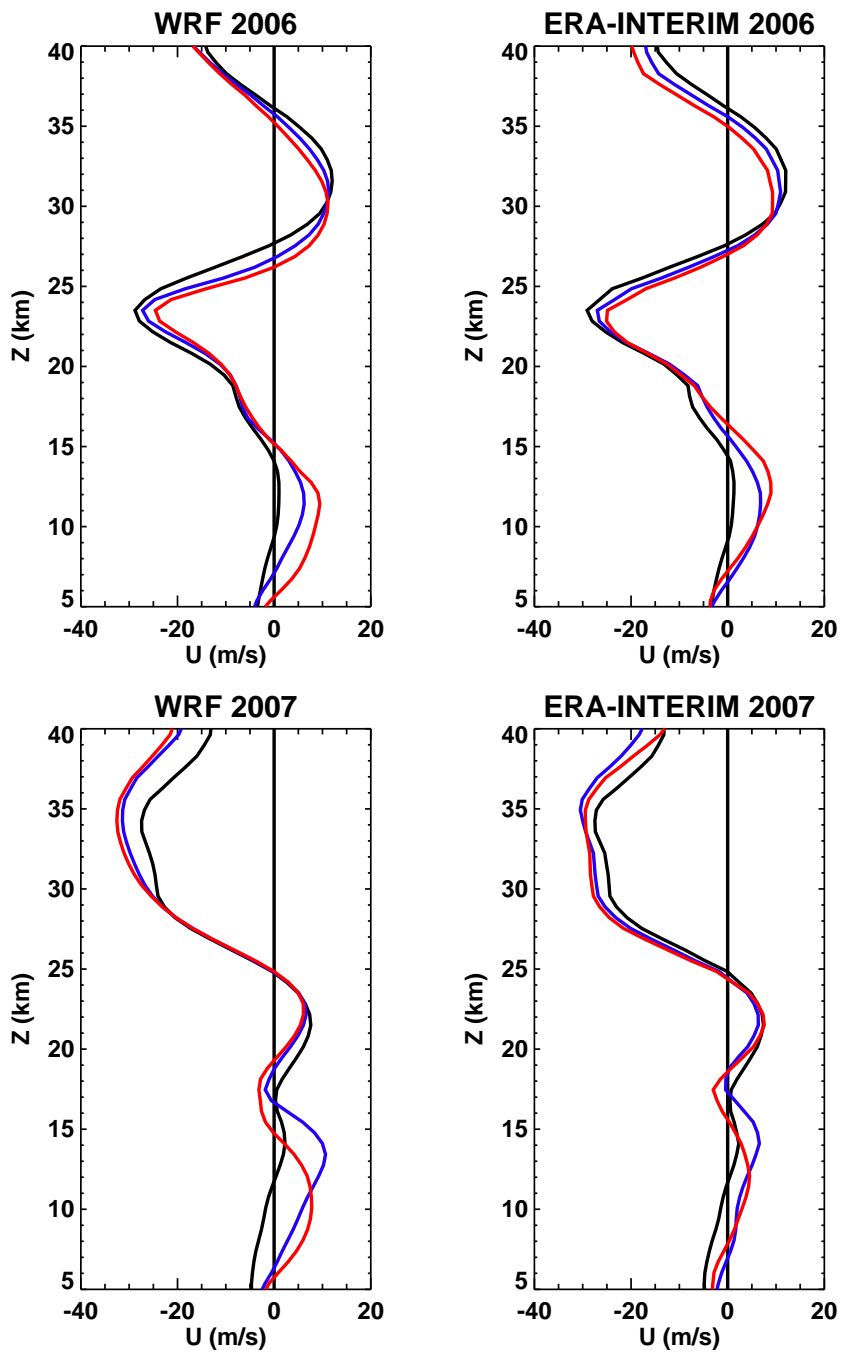


Figure 5.7: Evolution of WRF and ERA-I zonal mean zonal wind for the two simulation periods. The black curves indicate zonal wind vertical profiles at the beginning of the simulation, the blue profiles correspond to the middle of the simulation and the red curves to the end of the simulation.

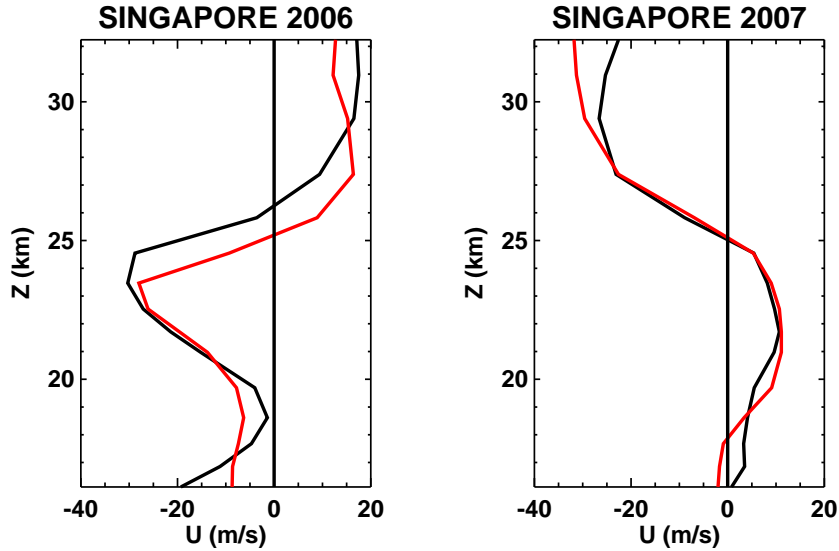


Figure 5.8: Monthly zonal wind profiles from daily radiosonde measurements at Singapore (103.98°E, 1.36°N) in 2006 (left) and 2007 (right). The black curves indicate monthly mean values for January and the red curves correspond to monthly means for February.

5.5.2 Upwelling

The mean tropical ascent of the Brewer-Dobson circulation acts to reduce the downward propagation of the QBO winds. To assess the effect of the tropical upwelling on the simulated QBO zonal wind evolution, we compute the mean tropical upwelling from WRF and ERA-I data. Following Andrews et al. [1987] the residual vertical velocity $\overline{w^*}$ is defined as :

$$\overline{w^*} = \overline{w} + (a \cos \phi)^{-1} \frac{\cos \phi \overline{v' \theta'}}{\overline{\theta_z}}$$

Figure 5.9 shows $\overline{w^*}$ over 10°S-10°N averaged over the simulation periods. On this plot the simulated tropical upwelling is compared to the ERA-I estimate for the same period. Some of the dominant mechanisms controlling the strength of the tropical upwelling, such as forcings from tropical planetary-scale waves or extratropical waves, are only partly represented in our monthly tropical channel simulations so some differences may be expected. Evaluating these differences is needed prior to the interpretation of TEM momentum budget (in 5.5.3).

In 2006 both vertical velocities are in reasonably good agreement. The largest difference is in the upper troposphere between 15 and 18 km where ERA-I estimate is much larger than WRF. In this region $\overline{w^*}$ is around 0.7 mm s^{-1} in WRF and 1.3 mm s^{-1} in ERA-I. Dima and Wallace (2007) estimated an annual mean vertical velocity of 0.55 mm s^{-1} at 100hPa ($\sim 16 \text{ km}$) from ERA-40 reanalysis.

Between 24 and 28 km $\overline{w^*}$ becomes slightly negative in ERA-I with a value of -0.08 mm s^{-1} while WRF simulated $\overline{w^*}$ is 0.06 mm s^{-1} . There is a QBO signal in temperature which is in thermal wind balance with the QBO signal in zonal winds. The QBO signal in temperature leads to a secondary meridional circulation. The QBO induced secondary meridional circulation corresponds to ascent during the easterly wind shear phase and descent during the westerly wind shear phase. The QBO induced descent in 2006 can explain the low values of $\overline{w^*}$ observed between 22 and 29km.

In 2007 there is an increase with height of $\overline{w^*}$ above 22 km. This increase is weak in the WRF data. Table 5.4 summarizes ERA-I and WRF values of $\overline{w^*}$ for the altitude ranges 15-18 km and 18-30 km. WRF simulations indicate $\overline{w^*}$ values of $0.28\text{-}0.34 \text{ mm s}^{-1}$ between 18 and 30 km which are consistent with the ERA-I estimates. Mote et al. (1996) estimated a vertical velocity between 16 and 32 km of $0.2\text{-}0.4 \text{ mm s}^{-1}$ from the tape recorder signal. Schoeberl et al. (2008) used stratospheric water vapor data from HALOE and MLS to estimate $\overline{w^*}$. Their study indicates $\overline{w^*}$ values of $\sim 0.4 \text{ mm s}^{-1}$ between 19 and 30 km. Therefore WRF estimates of $\overline{w^*}$ agree with the water vapor observations and ERA-I estimates, at least qualitatively.

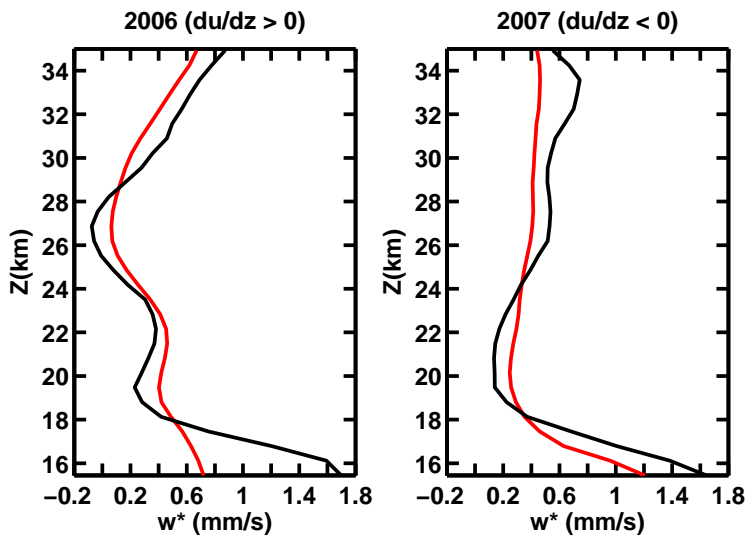


Figure 5.9: Vertical profiles of $\overline{w^*}$ averaged from 10°S to 10°N for the 2006 (left) and 2007 (right) simulations periods. The WRF estimates are shown in red and the ERA-I profiles are in black.

Table 5.4: Mean tropical upwelling $\overline{w^*}$ (mm s^{-1}) averaged over 10°S - 10°N

Data	15-18km	18-30km
WRF 2006	0.65	0.28
ERA-I 2006	1.31	0.19
WRF 2007	0.81	0.34
ERA-I 2007	1.18	0.35

To illustrate the differences in the QBO wind evolution between ERA-I and WRF, it can be instructive to look at the vertical advective acceleration in the QBO shear zone, i.e. the term $-\overline{w^* \frac{\partial \bar{u}}{\partial z}}$ of the TEM equation. From Figure 5.1, it can be seen that the QBO shear zones $du/dz > 0$ (in 2006) and $du/dz < 0$ (in 2007) are mainly between 23 and 32 km. WRF $|\frac{\partial \bar{u}}{\partial z}|$ is about $4 \times 10^{-3} \text{ s}^{-1}$ in this region for both QBO phases. ERA-I has a similar value for this height-range. Table 5.5 summarizes the values of $-\overline{w^* \frac{\partial \bar{u}}{\partial z}}$ and the simulated wind tendency $\frac{\partial \bar{u}}{\partial t}$ for this region for WRF and ERA-I.

During the westerly shear phase in 2006, the eastward wind tendency is stronger in WRF than in ERA-I by almost a factor of 2. The mean zonal wind acceleration is $0.17 \text{ m s}^{-1} \text{ day}^{-1}$ for WRF and $0.09 \text{ m s}^{-1} \text{ day}^{-1}$ for ERA-I. In comparison the mean acceleration between 23 and 32 km is equal to $0.19 \text{ m s}^{-1} \text{ day}^{-1}$ for the zonal wind profiles shown on Figure 5.8. Both ERA-I and WRF show a negative advective acceleration in the QBO shear zone. Between 23 and 32 km $-\overline{w^* \frac{\partial \bar{u}}{\partial z}}$ is equal to $-0.04 \text{ m s}^{-1} \text{ day}^{-1}$ for WRF and $-0.02 \text{ m s}^{-1} \text{ day}^{-1}$ for ERA-I. Both estimates are fairly weak and the absolute difference between the two terms which is $0.02 \text{ m s}^{-1} \text{ day}^{-1}$ accounts for 25% of the absolute difference between the wind tendency terms ($0.08 \text{ m s}^{-1} \text{ day}^{-1}$). Since the term $\overline{v^* [f - (a \cos \phi)^{-1} (\bar{u} \cos \phi)_\phi]}$ is negligible ($\sim 10^{-3} \text{ m s}^{-1} \text{ day}^{-1}$), it is unlikely that differences between WRF and ERA-I wind evolutions observed on Figure 5.7 can be explained only by differences between ERA-I and WRF vertical advective terms.

During the easterly shear phase in 2007, WRF and ERA-I show similar estimates of $-\overline{w^* \frac{\partial \bar{u}}{\partial z}}$. The ERA-I eastward wind tendency is stronger than that of WRF which shows almost no acceleration in this region. The WRF mean zonal wind tendency of $-0.03 \text{ m s}^{-1} \text{ day}^{-1}$ is in agreement with the mean zonal wind tendency of $-0.04 \text{ m s}^{-1} \text{ day}^{-1}$ between 23 and 32 km estimated from the wind profiles at Singapore shown on Figure 5.8. As $-\overline{w^* \frac{\partial \bar{u}}{\partial z}}$ is similar for both datasets, the differences between the wind tendency terms are certainly due to differences in wave forcings.

It should be emphasized that a thorough comparison of wave forcing from WRF and ERA-I is not possible as the ERA-I data available at NCAR have a temporal resolution of 6 hours and do not contain the wave forcing from gravity wave parameterization or the assimilation tendency terms.

As a result the EP flux calculation from ERA-I 6-hourly data which have a coarser resolution than WRF would include only part of the wave forcing.

Table 5.5: Mean acceleration terms $\partial\bar{u}/\partial t$ ($\text{m s}^{-1} \text{ day}^{-1}$) and $-\overline{w^*}\partial\bar{u}/\partial z$ ($\text{m s}^{-1} \text{ day}^{-1}$) for the height-range 23-32 km.

Terms	$\partial\bar{u}/\partial t$	$-\overline{w^*}\partial\bar{u}/\partial z$
WRF 2006	0.17	-0.04
ERA-I 2006	0.09	-0.02
WRF 2007	-0.03	0.14
ERA-I 2007	-0.12	0.15

Results from the previous section and this one suggest that the evolution of the QBO winds in WRF is relatively independent of the ERA-I boundary and initial conditions and that the waves generated by the model moist processes drive a large fraction of the evolution of the QBO winds in the equatorial belt. To understand the role of WRF resolved wave forcing we now compute the TEM momentum equation budget in the next section.

5.5.3 TEM momentum equation budget

Wave forcing of the QBO is considered by computing the different terms of the TEM momentum equation. Figure 5.10 shows the simulated zonal wind tendency, the EP flux divergence due to low ($\omega < 0.3$ cpd) and high ($\omega \geq 0.3$ cpd) frequency waves and the advective terms averaged over 10°S-10°N for the two QBO periods.

During January 2006, the tendency term is maximum near 26 km with an eastward acceleration of $0.55 \text{ m s}^{-1} \text{ day}^{-1}$. The total tendency due to EP flux divergence and advection has a peak of $0.4 \text{ m s}^{-1} \text{ day}^{-1}$ near 25.5 km. The eastward acceleration associated with gravity waves is larger than the forcing associated with low-frequency waves. The gravity wave forcing is maximum near 27 km with an acceleration of $0.38 \text{ m s}^{-1} \text{ day}^{-1}$. The maximum EP flux divergence due to low-frequency waves is $0.28 \text{ m s}^{-1} \text{ day}^{-1}$ at 25.5 km. The contributions of gravity waves and low-frequency account for 60% and 40% respectively to the total wave forcing. The advection term

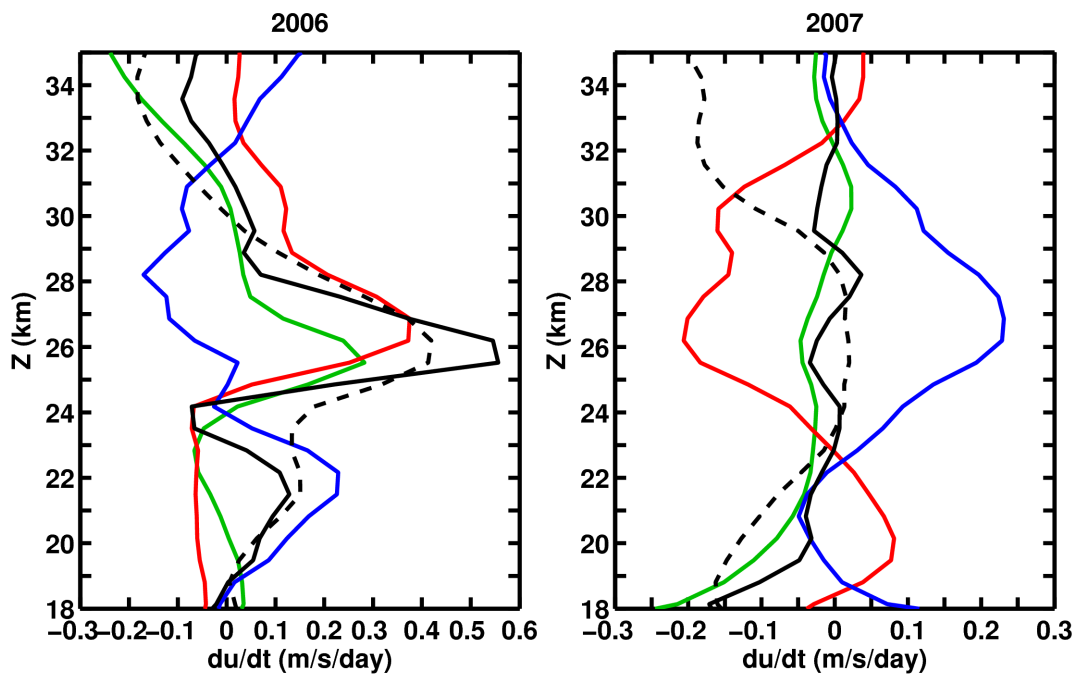


Figure 5.10: Vertical profiles of the zonal wind tendency (dashed black), the EP Flux divergence from low-frequency (green) and gravity waves (red), forcing due to the residual circulation (blue) and sum of EP Flux divergence and forcing due to the residual circulation (black). The forcing terms are averaged from 10°S to 10°N and over the two simulation periods.

represents a mean negative forcing of $-0.09 \text{ m s}^{-1} \text{ day}^{-1}$ between 25 and 32 km and thus reduces the eastward acceleration due to gravity waves in this region. During the westerly shear phase, low-frequency and gravity waves contribute roughly equally to the total net forcing and the effect of the mean residual circulation is small.

However during the easterly shear phase of the QBO in 2007, the contribution from low-frequency waves to the westward acceleration is small between 22 and 32 km and has a maximum of $-0.05 \text{ m s}^{-1} \text{ day}^{-1}$ at 26 km. Between 22 and 32 km the advection term compensates the westward forcing due to gravity waves and as a result the total forcing is small between 23 and 30 km. This is consistent with the stalling of the descent of the easterlies in January 2007 observed in Figure 5.1. In January 2007, the maximum westward acceleration associated with gravity waves is $-0.22 \text{ m s}^{-1} \text{ day}^{-1}$ at 26 km.

The wave forcing of the QBO described on Figure 5.10 is fairly similar to the study of Giorgetta et al. (2006). In particular Figure 5.10 can be compared to their Figure 10. They successfully simulated the QBO in a GCM with a triangular truncation of T42. Small-scale gravity waves are parameterized in their model. This study indicated that resolved large-scale waves contribute significantly to the QBO forcing during the westerly shear phase, while parameterized gravity waves are more important for the easterly shear phase. The results shown on Figure 5.10 may also be compared with the recent estimates of wave forcing obtained by Kawatani et al. (2010a). They investigated the contribution of equatorially trapped waves and inertia-gravity waves to the forcing of the QBO by using a high-resolution GCM. They estimated that gravity waves contribute around 50-75% of the eastward forcing during the westerly shear phase of the QBO and provide 70-80% of the westward forcing during the easterly shear phase of the QBO. Therefore our gravity wave estimates are roughly in agreement with their results although they study wave forcing of the QBO with a 3-year simulation.

5.6 Spatial characteristics of gravity waves

In this section we quantify which portions of the gravity wave spectrum make significant contributions to the gravity wave forcing shown on Figure 5.10. To investigate what horizontal scales of gravity waves contribute to the QBO forcing, we separate the EP flux divergences associated with zonal wavenumbers less than 42 (horizontal wavelengths $\lambda_x \geq 1000$ km) and zonal wavenumbers greater than 42 ($\lambda_x < 1000$ km). The band $\lambda_x \geq 1000$ km would correspond to the intermediate scale gravity waves which may be resolved by current GCMs/CCMs with a resolution $\sim 1\text{-}2^\circ$. The band $\lambda_x < 1000$ km would be the portion of the gravity wave spectrum which needs to be parameterized.

42 has also been the zonal wavenumber limit of the waves which can be resolved in previous numerical studies of the QBO (Horinouchi and Yoden, 1998; Giorgetta et al., 2006). In our study numerical diffusion, which is inherent to every numerical weather prediction model, results in waves with wavenumbers greater than about 150 to be strongly dissipated in the simulations. Therefore our present analysis will be restricted to the zonal wavenumber bands 1-42 and 43-150.

We further separate the contribution from short versus long vertical wavelength (λ_z) gravity waves to the forcing of the QBO. We use 10 km as the vertical scale separation between short and long vertical wavelength gravity waves. 10 km would be approximately the lower limit of vertical wavelength of gravity waves that current GCMs/CCMs with a vertical grid-spacing of ~ 1.5 to 2 km in the stratosphere can resolve. Short vertical wavelength gravity waves are obtained by applying a highpass filter to the full model vertical perturbations profiles (up to 0.1 hPa). The filter cut-off vertical wavelength is 10 km. The filter used is similar to the one described in chapter 3. We then compute the EP flux divergence associated with small vertical-scale gravity waves for the height-range 18 to 35 km.

Figure 5.11 shows the EP flux divergence profiles associated with different portions of the gravity wave spectrum for both simulation periods. On this plot, the different gravity wave categories all have $|\omega| > 0.3$ cpd.

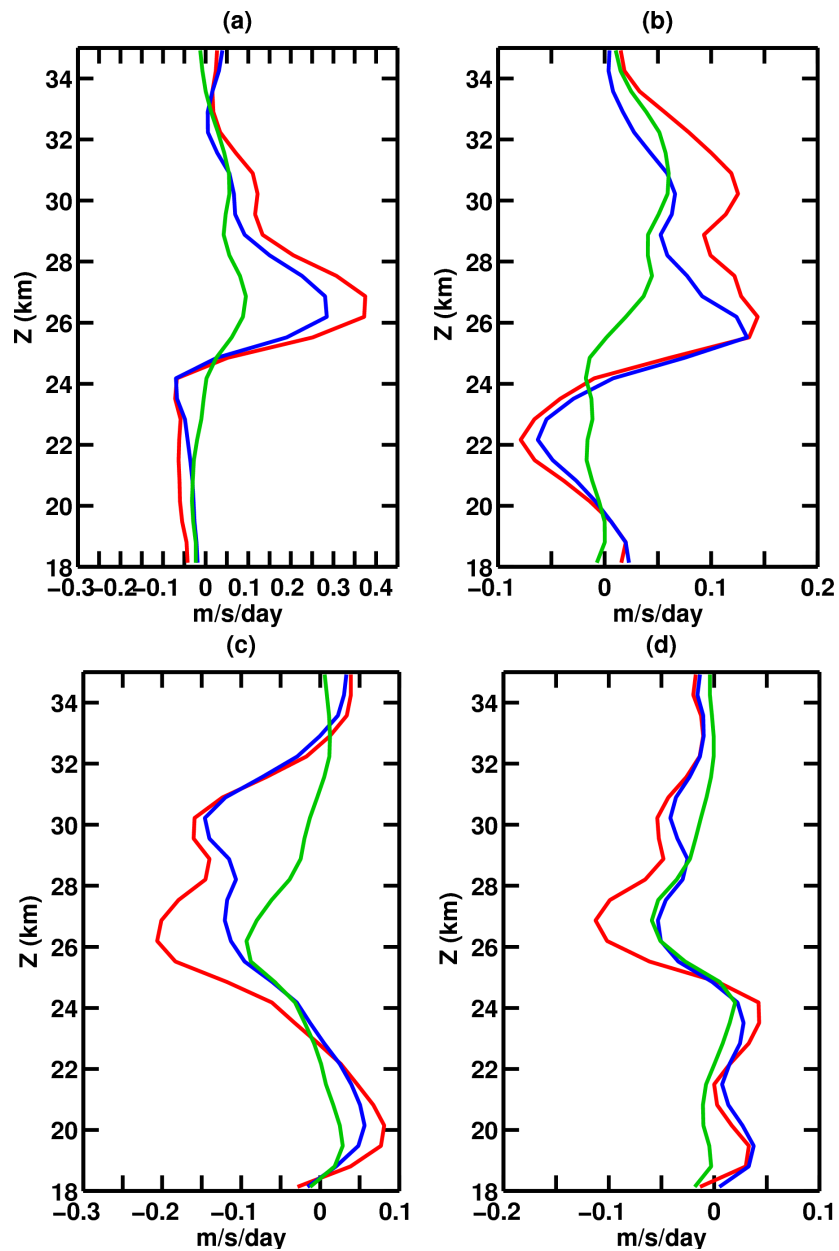


Figure 5.11: Vertical profiles of EP flux divergence associated with different gravity wave types. (a) 2006 total acceleration due to gravity waves (red), gravity waves with $\lambda_x \geq 1000$ km (blue) and gravity waves with $\lambda_x < 1000$ km (green). (b) Same profiles as (a) but for waves with $\lambda_z < 10$ km. (c) 2007 total acceleration due to gravity waves (red), gravity waves with $\lambda_x \geq 1000$ km (blue) and gravity waves with $\lambda_x < 1000$ km (green). (d) Same profiles as (c) but for waves with $\lambda_z < 10$ km.

During the westerly shear phase in 2006, Figure 5.11a indicates that intermediate scale gravity waves ($\lambda_x \geq 1000$ km) make a significant contribution to the total gravity wave eastward forcing and that the contribution from smaller scale gravity waves ($\lambda_x < 1000$ km) is weak. The same profiles on Figure 5.11b shows that the small vertical-scale gravity waves account roughly for 50% of the total gravity wave forcing.

During the easterly shear phase in 2007, Figure 5.11c indicates that both intermediate scale gravity waves and smaller scale gravity waves make an equal contribution to the westward gravity wave forcing between 23 and 26 km. The intermediate scale gravity waves make a larger contribution above 26 km. The profiles on Figure 5.11d show that the total gravity westward forcing due to small vertical-scale waves, is equally shared between intermediate scale and smaller-scale waves. These results are roughly consistent with the study of Kawatani et al. (2010a) which demonstrated that small-scale gravity waves play an important role during the easterly shear phase of the QBO in the lower stratosphere. It should be noted that Kawatani et al. (2010a) investigated the contribution of waves with zonal wavenumbers up to 213 to the forcing of the QBO while our analysis is restricted to wavenumbers smaller than ~ 150 .

Table 5.6 summarizes the peak accelerations associated with the different portions of the gravity wave spectrum. For both QBO phases, the small vertical-scale waves produce $\sim 50\%$ of the total gravity wave forcing. This suggests that small vertical-scale gravity waves can play an important role in forcing the QBO in the equatorial stratosphere.

During the westerly shear phase in 2006, values in Table 5.6 show that intermediate scale gravity waves account for $\sim 76\%$ of the total eastward gravity wave forcing and that the smaller-scale waves contribute $\sim 24\%$ of this forcing. About 36% of the intermediate scale gravity wave forcing is due to waves with short vertical wavelengths. This is in agreement with previous observational studies which indicated tropical inertia-gravity waves with horizontal wavelengths of thousands of kilometers and vertical wavelengths that vary from 3 to 6 km in the stratosphere (Wada et al., 1999; Ratnam et al., 2006; Evan and Alexander, 2008).

In 2007, both intermediate and smaller-scale waves are important for the westward QBO

Table 5.6: Peak accelerations ($\text{m s}^{-1} \text{ day}^{-1}$) associated with different gravity wave types for the height range 25-28 km.

2006 $du/dz > 0$	All waves	Total GW	GW ($\lambda_x \geq 1000$ km)	GW ($\lambda_x < 1000$ km)
Eastward forcing (all λ_z)	0.60	0.37	0.28	0.09
Eastward forcing ($\lambda_z < 10$ km)	0.23	0.14	0.11	0.03
2007 $du/dz < 0$	All waves	Total GW	GW ($\lambda_x \geq 1000$ km)	GW ($\lambda_x < 1000$ km)
Westward forcing (all λ_z)	-0.25	-0.20	-0.10	-0.10
Westward forcing ($\lambda_z < 10$ km)	-0.15	-0.11	-0.05	-0.06

forcing. In comparison to 2006 a larger portion (50%) of the intermediate-scale gravity waves have short vertical wavelengths.

Table 5.6 suggests that small-scale gravity waves are more important during the QBO easterly shear phase. However our estimates of small-scale gravity wave forcings are underestimated as they do not take into account the contributions from higher frequency waves ($|\omega| > 4$ cpd) and the very small-scale gravity waves ($\lambda_x < 270$ km). With this class of gravity waves taken in account, the forcing from small-scale waves may be more important for both QBO phases.

5.7 Summary and Discussion

It has been shown that the WRF model configured as a tropical channel can explicitly resolve a significant fraction of the gravity wave spectrum required to drive the QBO in the equatorial belt. The model was run for two periods in 2006 and 2007 corresponding to opposite QBO phases but associated with similar regimes of convection (i.e. Australian monsoon season).

Although the predictability for a forecast model drops significantly after two weeks, results from this study show that the WRF tropical channel model has the ability to capture the statistical characteristics of convection, such as location, strength and temporal evolution when compared to the TRMM 3-hourly precipitation data. We have analyzed the modeled tropical precipitation variability and showed that both simulations reproduced reasonably well precipitation variance up to ~ 3 cpd in comparison to that inferred from TRMM data. With an adjustment convective time

scale of 40 min, the temporal variability of tropical precipitation is dominated by the behavior of the microphysics scheme. This suggests that latent heating associated with the microphysics scheme may provide a dominant source of the gravity waves resolved in the simulations. However it should be noted that the lowest frequency modes (i.e. Kelvin and equatorial Rossby waves) are a product of the initialization with the ERA-Interim data.

As the precipitation variability is fairly well represented in the model, it should provide a reasonably complete picture of convectively generated gravity waves occurring in the QBO region (i.e. between ~ 19 and 35 km). The total vertical component of EP flux $|F^{(z)}|$ associated with westward and eastward propagating gravity waves at 65 hPa is 0.98 mPa for the January 2006 westerly shear phase and 0.80 mPa for the January 2007 easterly shear phase.

These values may be compared with determinations of $|F^{(z)}|$ obtained from radiosonde data at Singapore by Sato and Dunkerton (1997). Their study indicated values of $|F^{(z)}|$ of $20 \times 10^{-3} \text{ m}^{-2} \text{ s}^{-2}$ at 21 km for the westerly shear phase and in the range $7\text{-}30 \times 10^{-3} \text{ m}^{-2} \text{ s}^{-2}$ for the easterly shear phase. With a mean density of 0.08 at 21 km this yields values of $|F^{(z)}|$ around 1.6 mPa and 0.56-2.4 mPa respectively. Therefore our $|F^{(z)}|$ estimates due to gravity waves are in reasonably good agreement with the Sato and Dunkerton estimates. In our study, a significant portion of gravity waves contributing to $|F^{(z)}|$ have phase speeds $|c| < 35 \text{ m s}^{-1}$ and thus are likely to play a role in the stratospheric QBO.

This configuration of the WRF model was also able to reproduce fairly well the evolution of the QBO zonal winds in the equatorial belt in comparison to the Singapore observational data and ERA-I zonal wind. In addition, the tropical upwelling estimates for both simulations are consistent with the values obtained from ERA-I estimates and from previous studies.

It was shown that gravity waves account for $\sim 60\%$ of the total eastward forcing during the westerly shear phase and for $\sim 80\%$ of the total westward forcing during the easterly shear phase.

During the westerly shear phase, most of the gravity wave forcing is coming from intermediate scale gravity waves with $\lambda_x \geq 1000 \text{ km}$. During the easterly shear phase, smaller-scale gravity waves with $\lambda_x < 1000 \text{ km}$ represent 50% of the total gravity wave forcing. The contribution from smaller-

scale gravity waves may be underestimated in our simulations as we only take into account waves with frequencies up to 4 cpd and zonal wavenumbers up to 150. However our estimates are roughly similar to results from Giorgetta et al. (2006) and Kawatani et al. (2010a) although they used multiple year climate model simulations to evaluate gravity wave forcing of the QBO.

Current coarse-grid climate models and chemistry-climate models typically used a gravity wave parameterization to help the representation of the QBO in the stratosphere. However it is still unclear which portion of the gravity wave spectrum should be explicitly resolved and which fraction should be parameterized to obtain a realistic QBO. Our study may shed some light on this issue by using the results from table 5.6. In this table the intermediate scale waves with ($\lambda_x \geq 1000$ km) would correspond to the resolvable part of the gravity wave spectrum in climate models.

It should be emphasized that current climate models have a horizontal resolution of $\sim 1\text{-}2^\circ$ that might be sufficient to resolve the horizontal structure of intermediate-scale gravity waves, but they also have a coarse vertical grid-spacing in the stratosphere (~ 2 km) which will be inadequate to resolve the vertical structure of these waves. Hence current climate models may miss a substantial fraction of the intermediate-scale gravity wave spectrum associated with the waves with short vertical wavelengths.

During the westerly shear phase of 2006, gravity waves with $\lambda_x \geq 1000$ km and $\lambda_z < 10$ km produce an eastward acceleration of $0.11 \text{ m s}^{-1} \text{ day}^{-1}$ which accounts for $\sim 30\%$ of the total eastward gravity wave acceleration of $0.37 \text{ m s}^{-1} \text{ day}^{-1}$. Similarly, during the easterly shear phase of 2007, intermediate scale gravity waves with short vertical wavelengths produce a westward acceleration of $-0.05 \text{ m s}^{-1} \text{ day}^{-1}$ which corresponds to 25% of the total wave forcing of $-0.20 \text{ m s}^{-1} \text{ day}^{-1}$.

Therefore global models which do not have a high vertical resolution may miss about 30% of the gravity wave forcing of the QBO associated with intermediate-scale gravity waves with short vertical wavelengths. The effect of these waves on the QBO would need to be parameterized even if they have horizontal wavelengths that ought to be resolved. For both simulations intermediate-

scale gravity waves with short vertical wavelengths are associated with $|F^{(z)}|$ of 0.6 mPa at 65 hPa. The spectrum at this level presents an west-east asymmetry (not shown) which can be due to the wind direction above the convective source and the source motion.

From Table 5.6 we can estimate that during the westerly shear phase of 2006, waves with $\lambda_x \geq 1000\text{km}$ and $\lambda_z \geq 10\text{ km}$ produce an eastward acceleration of $0.17\text{ m s}^{-1}\text{ day}^{-1}$ which is equal to $\sim 50\%$ of the total gravity wave forcing of $0.37\text{ m s}^{-1}\text{ day}^{-1}$. Therefore 50% of the gravity wave spectrum could be explicitly resolved by coarse-grid GCMs. The remaining 50% part of the spectrum (waves with $\lambda_x \geq 1000\text{km}$ and $\lambda_z < 10\text{ km}$ or waves with $\lambda_x < 1000\text{ km}$) will then have to be parameterized. In contrast, during the easterly shear phase of 2007, up to 75% would need to be parameterized in coarse-grid GCMs.

In this study, we tried to quantify the gravity wave forcing of the QBO by using a configuration of the WRF model with a high top at 0.1 hPa and a grid-spacing of 37 km for the global tropics. One limitation of this study is that our estimates are based on monthly-simulations whereas previous studies of QBO have used multiple year simulations. However given the flexibility of this model configuration and the availability of the ERA-Interim data for several years, our results could be extended to several QBO periods.

This portion of the work is in preparation for the Journal of Geophysical Research.

Chapter 6

Summary and Conclusions

A broad spectrum of tropical waves is needed to drive the middle atmospheric circulation. A complete understanding of these waves is important for an accurate representation of the QBO in climate models. For intermediate-scale inertia-gravity waves, it is still unclear if this wave type contributes significantly to the driving of the QBO. Throughout the thesis, we tried to increase the current understanding of tropical inertia-gravity waves by answering three main questions. These are:

- What are the inertia-gravity wave properties from observations ?
- What is required for numerical models to have an accurate representation of tropical inertia-gravity waves ?
- Which gravity waves contribute to the QBO forcing ?

These questions have been considered using observational data and high-resolution numerical experiments which have been analyzed using wavelet and FFT techniques. We first used high-resolution soundings of horizontal wind and temperature taken the 2006 TWP-ICE experiment to study a 2-day stratospheric inertia-gravity wave which was observed in the campaign. A similar wave event was observed in the ECMWF data but with a different vertical structure. Subsequently we performed several WRF numerical experiments to understand the influence of vertical resolution on the 2-day wave represented in the ECMWF data. In addition, a ray tracing analysis and the WRF simulations were used to determine the physical mechanisms which led to the wave generation.

Finally, WRF simulations for opposite QBO phases were used to quantify the QBO forcing due to intermediate-scale inertia-gravity waves and to provide some guidance for constraining gravity wave parameterizations in coarse-grid climate models.

In the following sections, the main results of this thesis will be discussed in relation to the research questions proposed.

6.1 Tropical inertia-gravity wave properties and their representation in numerical models

Previous observational studies have indicated that tropical inertia-gravity waves have horizontal wavelengths ranging from a thousand to ten thousands kilometers. This wave type is also associated with periods ranging from 12 hours to 3 days and vertical wavelengths smaller than about 6 km. Observations of past experiments have also indicated intermediate-scale inertia-gravity waves with a propagation correlated to the phase of the QBO, i.e. eastward propagating waves are seen in westerly shear phases of the QBO, while westward propagating waves are seen in easterly shear phases (Baldwin, 2001).

Using the TWP-ICE radiosonde data we have shown that the properties of the 2-day period stratospheric inertia-gravity wave observed during the campaign are in agreement with these previous studies. The wave presents vertical and horizontal wavelength of around 6 km and 7220 km respectively. The wave was observed to propagate southeastward during the westerly shear phase of the QBO. The total vertical momentum flux associated with the 2-day wave is estimated to be 1 to $2.2 \times 10^{-3} \text{ m}^2 \text{ s}^{-2}$. This is of the same order of magnitude as previous observations of 4-10 day Kelvin waves in the lower stratosphere and provides some evidence for the importance of forcing of the QBO by inertia-gravity waves.

A similar wave event is observed in the ECMWF data. A comparison between the characteristics of the 2-day wave derived with the ECMWF data to the properties of the wave derived with the radiosonde data shows that the ECMWF data capture similar structure for this 2-day wave event but with a larger vertical wavelength. A reverse ray tracing method was used to localize

the source region. Using ECMWF data to define the atmospheric background conditions and wave properties observed in the soundings, it was found that the 2-day wave event originated from deep convection in the Indonesian region.

The WRF configured as a tropical channel model with a high top is used to assess the influence of vertical resolution, cumulus parameterizations and initial conditions on the wave structure. WRF is used with the same horizontal resolution as the operational ECMWF in 2006 ($\sim 40\text{km}$). In these WRF experiments we found several important factors relevant to the proper representation of inertia-gravity waves in numerical models and analysis data. One of the most important factors corresponds to the vertical resolution. We demonstrate that higher vertical resolution (grid-spacing less than 1 km) would be required for ECMWF to accurately resolve the vertical structure of intermediate-scale inertia-gravity waves and their effect on the middle-atmospheric circulation.

As computing power continues to increase, climate and forecast models are being constantly improved. In the past, increasing computer power has been used predominantly for increasing the horizontal resolution while the vertical resolution was not improved. However, as stated in Chapter 1, both high horizontal and vertical resolutions are needed to get an accurate representation of inertia-gravity waves and the QBO in numerical models. A more balanced choice of horizontal/vertical resolution could improve the representation of inertia-gravity wave effects on the tropical stratospheric. This is needed for climate models but also for forecast models which produce analyses. This effort is underway at ECMWF as in 2008 the vertical resolution was increased in the stratosphere (with a vertical grid-spacing less than 1km between 20 and 30km).

The results of the ray tracing analysis and the WRF experiments indicated that the 2-day wave was likely generated by the interaction between upper-tropospheric winds and the slow moving convection via the obstacle effect mechanism. This indicates that an accurate depiction of inertia-gravity wave generation by the obstacle effect in numerical models is sensitive to models' representation of vertical wind shear and the depth and propagation of convection.

The requirement of high vertical resolution is also applicable to the proper representation of vertical wind shear. The numerical experiments presented in Chapter 4 used a cumulus parame-

terization to represent the effects of deep convection. Among the two cumulus schemes used, only the scheme with a daily variability similar to the observed precipitation was able to generate the wave. This shows that the choice of cumulus parameterization will also affect the generation of tropical inertia-gravity waves in numerical models. The fact that the BMJ scheme in Chapter 4 can fairly well represent the diurnal cycle of precipitation seems to be in agreement with the results of Sassi and Garcia (1997) who suggested that diurnal convective forcing can be important for the generation of intermediate-scale inertia-gravity waves.

6.2 Gravity wave forcing of the QBO

In chapter 5 we used WRF simulation for opposite QBO phases to assess the wave forcing of the QBO. In this chapter, we combined mesoscale and global model approaches to address the QBO problem. It is widely accepted that a broad spectrum of waves is necessary to force the QBO in numerical models. In our simulations, the low-frequency part of the wave spectrum, which is associated with planetary waves (i.e Kelvin and Rossby waves), is a product of the WRF initialization with the ECWMF analyses. We showed that the model has a realistic representation of tropical precipitation variability when compared to observational data and so in principle should be able to produce most of the gravity wave spectrum. We also showed that the model has an adequate representation of the tropical upwelling, which is a crucial factor to the proper evaluation of wave forcing of the QBO.

Using the high-resolution model outputs, we computed the gravity wave forcing of the QBO. It was shown that gravity waves account for $\sim 60\%$ of the total eastward forcing during the westerly shear phase and for $\sim 80\%$ of the total westward forcing during the easterly shear phase. These estimates are in agreement with previous numerical studies of the QBO (Kawatani et al., 2010a; Giorgetta et al., 2006) which showed that gravity waves provide a significant forcing of the QBO.

Coarse-grid global models account for the effects of unresolved gravity waves with a physical parameterization. In numerical modeling, a physical parameterization aims to represent the effects of subgrid processes by using resolvable scale fields. Traditionally in climate models, the scale

separation for the wave spectrum is associated with the wave horizontal wavelength. However some climate models or global models can have a horizontal resolution that may be appropriate to resolve the horizontal structure of intermediate scale gravity waves, but they may have a vertical grid-spacing which will be inadequate to resolve the vertical structure of the waves. Hence these global models may miss a substantial fraction of the intermediate-scale gravity wave spectrum associated with short vertical wavelength waves. In the WRF simulations, this wave type represents $\sim 30\%$ of the total gravity wave forcing of the QBO.

Current coarse-grid climate models usually have a parameterization of small-scale gravity waves generated by convection. The results of chapter 5 indicate that these models should also include a parameterization of intermediate-scale inertia-gravity waves with short vertical wavelength for an accurate representation of the QBO. Recently, a parameterization of inertia-gravity waves (with horizontal wavelengths equal to 1000km) has been implemented in the tropics in the Whole Atmosphere Community Climate Model (WACCM). The parameterized inertia-gravity wave forcing was capable of generating a QBO (Dr H.-L. Liu, personal communication). An inertia-gravity wave parameterization requires wave spectral characteristics such as wave phase speed and wave momentum flux. In the simulations of Chapter 5, intermediate-scale gravity waves with short vertical wavelengths are associated with a total momentum flux of 0.6 mPa at 65 hPa. At this level, a significant part of the inertia-gravity wave spectrum has absolute phase speeds less than 35 m s^{-1} . The spectrum presents a west-east asymmetry which likely depends on the horizontal winds above the convective source and the source motion.

6.3 Perspectives

This thesis has provided insights into the properties and generation mechanisms of intermediate scale inertia-gravity waves in the tropics. It has also quantified the proportion of the QBO acceleration that can be explained by these waves. The properties of the 2-day stratospheric inertia-gravity wave observed during the TWP-ICE campaign are in agreement with previous studies. However it is difficult to say if short vertical wavelength inertia-gravity waves observed in

radiosonde data are representative of the whole inertia-gravity wave spectrum in the tropics. Additional observational data collected on a campaign basis would be needed to assess whether this wave type dominates the intermediate-scale wave spectrum in the tropics.

In this work, the properties of the 2-day wave present in the ECMWF data have been compared to the TWP-ICE observations. In addition, a ray tracing analysis and WRF simulations with varying initial conditions have been used to identify the wave generation mechanism. It would be interesting to conduct a similar study for intermediate-scale inertia-gravity waves which have been identified in previous observational data. In particular the 2-day wave observed during TWP-ICE presents some similarities with the inertia-gravity waves studied by Wada et al. (1999) and Ratnam et al. (2006). The methodology described in Chapter 4 could be applied to these case studies to assess whether the waves observed present generation mechanisms similar to the "obstacle effect" described in Chapter 4. This would provide useful information for the development of tropical inertia-gravity wave parameterization for climate models.

The intermediate-scale inertia-gravity wave spectrum presented in Chapter 5 corresponds to austral summer conditions (January-February). However given the flexibility of the WRF tropical channel model and the availability of the ECMWF or other modern reanalyses for several years, this work could be extended to several QBO periods and different convective regimes to have a better estimate of inertia-gravity wave forcing of the stratospheric circulation.

Bibliography

- Alexander, M. J. and C. Barnet, 2007: Using satellite observations to constrain parameterizations of gravity wave effects for global models. *J. Atmos. Sci.*, **64**, 1652–1665, doi:10.1175/JAS3897.1.
- Alexander, M. J. and J. R. Holton, 1997: A model study of zonal forcing in the equatorial stratosphere by convectively induced gravity waves. *J. Atmos. Sci.*, **54**, 408–419, doi:10.1175/1520-0469(1997)054<0408:AMSOZF>2.0.CO;2.
- Alexander, M. J., J. R. Holton, and D. R. Durran, 1995: The gravity wave response above deep convection in a squall line simulation. *J. Atmos. Sci.*, **52**, 2212–2226, doi:10.1175/1520-0469(1995)052<2212:TGWRAD>2.0.CO;2.
- Alexander, M. J., et al., 2008: Global estimates of gravity wave momentum flux from High Resolution Dynamics Limb Sounder observations. *J. Geophys. Res.*, **113**, D15S18, doi:10.1029/2007JD008807.
- Alexander, S. P. and T. Tsuda, 2008: Observations of the diurnal tide during seven intensive radiosonde campaigns in Australia and Indonesia. *J. Geophys. Res.*, **113**, D04109, doi:10.1029/2007JD0088717.
- Andrews, D. G., J. R. Holton, and C. B. Leovy, 1987: *Middle Atmospheric Dynamics*. Academic Press, 489 pp.
- Baldwin, M. P., et al., 2001: The Quasi-Biennial Oscillation. *Rev. Geophys.*, **39**, 179–229.
- Bengtsson, L., K. I. Hodges, and S. Hagemann, 2004: Sensitivity of the ERA40 reanalysis to the observing system: determination of the global atmospheric circulation from reduced observations. *Tellus A*, **56**, 456–471.
- Beres, J. H., 2004: Gravity wave generation by a three-dimensional thermal forcing. *J. Atmos. Sci.*, **61**, 1805–1815, doi:10.1175/1520-0469(2004)061<1805:GWGBAT>2.0.CO;2.
- Beres, J. H., M. J. Alexander, and J. R. Holton, 2002: Effects of tropospheric wind shear on the spectrum of convectively generated gravity waves. *J. Atmos. Sci.*, **59** (11), 1805–1824, doi:10.1175/1520-0469(2002)059<1805:EOTWSO>2.0.CO;2.
- Bergman, J. W. and M. L. Salby, 1994: Equatorial wave activity derived from fluctuations in observed convection. *J. Atmos. Sci.*, **51**, 3791–3806.
- Betts, A. K., 1986: A new convective adjustment scheme. Part I: Observational and theoretical basis. *Quart. J. Roy. Meteor. Soc.*, **112**, 677–691.

- Betts, A. K. and M. J. Miller, 1986: A new convective adjustment scheme. Part II: Single column tests using GATE wave, BOMEX and arctic air-mass data sets. *Quart. J. Roy. Meteor. Soc.*, **112**, 693–709.
- Boville, B. A. and W. J. Randel, 1992: Equatorial waves in a stratospheric GCM: Effects of vertical resolution. *J. Atmos. Sci.*, **49** (9), 785–801, doi:10.1175/1520-0469(1992)049<0785:EWIASG>2.0.CO;2.
- Cadet, D. and H. Teitelbaum, 1979: Observational evidence of internal inertia-gravity waves in the tropical stratosphere. *J. Atmos. Sci.*, **36** (5), 892–907, doi:10.1175/1520-0469(1979)036<0892:OEOIIG>2.0.CO;2.
- Chen, F. and J. Dudhia, 2001: Coupling an advanced land-surface/ hydrology model with the Penn State/ NCAR MM5 modeling system. Part I: Model description and implementation. *Mon. Wea. Rev.*, **129**, 569–585.
- Chou, M.-D. and M. J. Suarez, 1994: An efficient thermal infrared radiation parameterization for use in general circulation models. *NASA Tech. Memo*, **104606** (3), pp85.
- Dima, I. M. and J. M. Wallace, 2007: Structure of the annual-mean equatorial planetary waves in the ERA-40 reanalyses. *J. Atmos. Sci.*, **64**, 2862–2880, doi:10.1175/JAS3985.1.
- Dunkerton, T. J., 1997: The role of gravity waves in the Quasi-Biennial Oscillation. *J. Geophys. Res.*, **102**, 26 053–26 076.
- Ern, M., P. Preusse, M. J. Alexander, and C. D. Warner, 2004: Absolute values of gravity wave momentum flux derived from satellite data. *J. Geophys. Res.*, **109**, D20 103, doi: 10.1029/2004JD004752.
- Evan, S. and M. J. Alexander, 2008: Intermediatescale tropical inertia gravity waves observed during the TWPICE campaign. *J. Geophys. Res.*, **113**, D14 104, doi:10.1029/2007JD009289.
- Evan, S., M. J. Alexander, and J. Dudhia, 2011: Model study of intermediate-scale tropical inertia-gravity waves and comparison to TWP-ICE campaign observations. *J. Geophys. Res.*, doi:10.1175/JAS-D-11-051.1.
- Fels, S. B., 1982: A parameterization of scale-dependent radiative damping rates in the middle atmosphere. *J. Atmos. Sci.*, **39**, 1141–1152.
- Fovell, R., D. Durran, and J. R. Holton, 1992: Numerical simulations of convectively generated stratospheric gravity waves. *J. Atmos. Sci.*, **49**, 1427–1442, doi:10.1175/1520-0469(1992)049<1427:NSOCGS>2.0.CO;2.
- Fritts, D. C. and M. J. Alexander, 2003: Gravity wave dynamics and effects in the middle atmosphere. *Rev. Geophys.*, **41**, 1003, doi:10.1029/2001RG000106.
- Garcia, R., T. Dunkerton, R. Lieberman, and R. Vincent, 1997: Climatology of the semiannual oscillation of the tropical middle atmosphere. *J. Geophys. Res.*, **102(D22)**, 26 019–26 032.
- Gill, A. E., 1982: *Atmosphere-Ocean Dynamics*. Elsevier, New York, 662 pp.
- Giorgetta, M. A., E. Manzini, and E. Roeckner, 2002: Forcing of the Quasi-Biennial Oscillation from a broad spectrum of atmospheric waves. *Geophys. Res. Lett.*, **29** (8), 86–1 to 86–4.

- Giorgetta, M. A., E. Manzini, E. Roeckner, M. Esch, and L. Bengtsson, 2006: Climatology and forcing of the Quasi-Biennial Oscillation in the MAECHAM5 model. *J. Climate*, **19**, 3882–3901.
- Grimsdell, A. W., M. J. Alexander, P. T. May, and L. Hoffman, 2010: Model study of waves generated by convection with direct validation via satellite. *J. Atmos. Sci.*, **67**, 1617–1631, doi:10.1175/2009JAS3197.1.
- Hamilton, K., R. J. Wilson, and R. S. Hemler, 1999: Middle atmosphere simulated with high vertical and horizontal resolution versions of a GCM: Improvements in the cold pole bias and generation of a QBO-like oscillation in the tropics. *J. Atmos. Sci.*, **56** (22), 3829–3846, doi:10.1175/1520-0469(1999)056<3829:MASWHV>2.0.CO;2.
- Hamilton, K., R. J. Wilson, and R. S. Hemler, 2001: Spontaneous stratospheric QBO-like oscillations simulated by the GFDL SKYHI general circulation model. *J. Atmos. Sci.*, **58** (21), 3271–3292, doi:10.1175/1520-0469(2001)058<3271:SSQLOS>2.0.CO;2.
- Highwood, E. J. and B. J. Hoskins, 2001: The tropical tropopause. *Quart. J. Roy. Meteor. Soc.*, **124**, 1579–1604.
- Holton, J. R., M. J. Alexander, and M. T. Boehm, 2001: Evidence for short vertical wavelength Kelvin waves in the Department of Energy-Atmospheric Radiation Measurement Nauru99 radiosonde data. *J. Geophys. Res.*, **106**, 20 125–20 129, doi:10.1029/2001JD900108.
- Holton, J. R., J. H. Beres, and X. Zhou, 2002: On the vertical scale of gravity waves excited by localized thermal forcing. *J. Atmos. Sci.*, **59**, 2019–2023.
- Holton, J. R. and R. S. Lindzen, 1972: An updated theory for the quasi-biennial cycle of the tropical stratosphere. *J. Atmos. Sci.*, **29**, 1076–1080, doi:10.1175/1520-0469(1972)029<1076:AUTFTQ>2.0.CO;2.
- Hong, S.-Y., J. Dudhia, and S.-H. Chen, 2004: A revised approach to ice microphysical process for bulk parameterizations of clouds and precipitation. *Mon. Wea. Rev.*, **132**, 103–120.
- Horinouchi, T. and S. Yoden, 1998: Wave-mean flow interaction associated with a QBO-like oscillation simulated in a simplified GCM. *J. Atmos. Sci.*, **55** (22), 502–526, doi:10.1175/1520-0469(1998)055<0502:WMFIAW>2.0.CO;2.
- Horinouchi, T., et al., 2003: Tropical cumulus convection and upward-propagating waves in middle-atmospheric GCMs. *J. Atmos. Sci.*, **60** (22), 2765–2782, doi:10.1175/1520-0469(2003)060<2765:TCCA UW>2.0.CO;2.
- Inoue, T., M. Satoh, H. Miura, and B. Mapes, 2008: Characteristics of cloud size of deep convection simulated by a Global Cloud Resolving Model over the Western Tropical Pacific. *J. Meteor. Soc. Japan*, **86A**, 1–15.
- Janjic, Z. I., 1994: The step-mountain eta coordinate model: further developments of the convection, viscous sublayer and turbulence closure schemes. *Mon. Wea. Rev.*, **122**, 927–945.
- Janjic, Z. I., 2000: Comments on Development and evaluation of a convection scheme for use in climate models. *J. Atmos. Sci.*, **57**, 3686.

- Janjic, Z. I., 2002: Nonsingular implementation of the Mellor-Yamada level 2.5 scheme in the NCEP Meso model. *NCEP Office Note*, **No. 437**, 61 pp.
- Jensen, E. and L. Pfister, 2004: Transport and freeze-drying in the tropical tropopause layer. *J. Geophys. Res.*, **109 (D02207)**, doi:10.1029/2003JD004022.
- Kain, J. S. and J. M. Fritsch, 1990: A one-dimensional entraining/ detraining plume model and its application in convective parameterization. *J. Atmos. Sci.*, **47**, 2784–2802.
- Kawatani, Y., M. Takahashi, K. Sato, S. P. Alexander, and T. Tsuda, 2009: Global distribution of atmospheric waves in the equatorial upper troposphere and lower stratosphere: AGCM simulation of sources and propagation. *J. Geophys. Res.*, **114 (D01102)**, doi:10.1029/2008JD010374.
- Kawatani, Y., S. Watanabe, K. Sato, T. J. Dunkerton, S. Miyahara, and M. Takahashi, 2010a: The roles of equatorial trapped waves and internal inertia-gravity waves in driving the Quasi-Biennial oscillation. Part I: Zonal mean wave forcing. *J. Atmos. Sci.*, **67 (4)**, 963–980, doi:10.1175/2009JAS3222.1.
- Kawatani, Y., S. Watanabe, K. Sato, T. J. Dunkerton, S. Miyahara, and M. Takahashi, 2010b: The roles of equatorial trapped waves and internal inertia-gravity waves in driving the Quasi-Biennial oscillation. Part II: Three-dimensional distribution of wave forcing. *J. Atmos. Sci.*, **67 (4)**, 981–997, doi:10.1175/2009JAS3223.1.
- Kim, S., H. Chun, and D. L. Wu, 2009: A study on stratospheric gravity waves generated by typhoon Ewiniar: Numerical simulations and satellite observations. *J. Geophys. Res.*, **114**, D22 104, doi:10.1029/2009JD011971.
- Klemp, J. B., J. Dudhia, and A. D. Hassiotis, 2008: An upper gravity-wave absorbing layer for NWP applications. *Mon. Wea. Rev.*, **136**, 3987–4004, doi:10.1175/2008MWR2596.1.
- Kuester, M., M. Alexander, and E. Ray, 2008: A model study of gravity waves over Hurricane Humberto (2001). *J. Atmos. Sci.*, **65**, 3231–3246.
- Lane, T. P., M. J. Reeder, and T. L. Clark, 2001: Numerical modeling of gravity wave generation by deep tropical convection. *J. Atmos. Sci.*, **58**, 1249–1274.
- Le Sommer, J., H. Teitelbaum, and V. Zeitlin, 2006: Global estimates of equatorial inertia-gravity wave activity in the stratosphere inferred from ERA40 reanalysis. *Geophys. Res. Lett.*, **33**, L07 810, doi:10.1029/2005GL024873.
- Lindzen, R. S. and J. R. Holton, 1968: A theory of the Quasi-Biennial Oscillation. *J. Atmos. Sci.*, **25**, 1095–1107, doi:10.1175/1520-0469(1968)025<1095:ATOTQB>2.0.CO;2.
- Mahfouf, J.-f., Bauer, P., and V. Marcal, 2005: The assimilation of SSM/I and TMI rainfall rates in the ECMWF 4D-Var system. *Quart. J. Roy. Meteor. Soc.*, **131**, 437–458.
- Mapes, B. E. and R. A. Houze, 1993: Cloud clusters and superclusters over the oceanic warm pool. *Mon. Wea. Rev.*, **121**, 1398–1416.
- Marks, C. J. and S. D. Eckermann, 1995: A three-dimensional nonhydrostatic ray-tracing model for gravity waves: Formulation and preliminary results for the middle atmosphere. *J. Atmos. Sci.*, **52 (11)**, 1959–1984, doi:10.1175/1520-0469(1995)052<1959:ATDNRT>2.0.CO;2.

- May, P. T., J. H. Mather, G. Vaughan, K. N. Bower, C. Jakob, G. M. McFarquhar, and G. G. Mace, 2008: The Tropical Warm Pool International Cloud Experiment. *Bull. Amer. Meteor. Soc.*, **89** (5), 629–645, doi:10.1175/BAMS-89-5-629.
- McLandress, C. and J. F. Scinocca, 2005: The GCM response to current parameterizations of nonorographic gravity wave drag. *J. Atmos. Sci.*, **62**, 2394–2413, doi:10.1175/JAS3483.1.
- Mlawer, E. J., S. J. Taubman, P. D. Brown, M. J. Iacono, and S. A. Clough, 1997: Radiative transfer for inhomogeneous atmosphere: RRTM, a validated correlated-k model for the longwave. *J. Geophys. Res.*, **102** (D14), 16 663–16 682.
- Mote, P., et al., 1996: An atmospheric tape recorder: The imprint of tropical tropopause temperatures on stratospheric water vapor. *J. Geophys. Res.*, **101**, 3989–4006.
- Murthy, B. V. K., K. Satheesan, K. Parameswaran, M. N. Sasi, G. Ramkumar, Y. Bhavanikumar, K. Raghunath, and M. Krishniah, 2002: Equatorial waves in temperature in the altitude range 4 to 70 km. *Quart. J. Roy. Meteor. Soc.*, **128**(581), 819–837.
- Naujokat, B., 1986: An update of the observed quasi-biennial oscillation of the stratospheric winds over the tropics. *J. Atmos. Sci.*, **43**, 1873–1877, doi:10.1175/1520-0469(1986)043<1873:AUOTOQ>2.0.CO;2.
- Ortland, D. A., M. J. Alexander, and A. Grimsdell, 2011: On the wave spectrum generated by tropical heating. *J. Atmos. Sci.*, doi:10.1175/2011JAS3718.1.
- Pfister, L., et al., 1993: Gravity waves generated by a tropical cyclone during the STEP tropical field program: A case study. *J. Geophys. Res.*, **98**(D5), 8611–8638.
- Piani, C., D. Durran, M. J. Alexander, and J. R. Holton, 2000: A numerical study of three-dimensional gravity waves triggered by deep tropical convection and their role in the dynamics of the QBO. *J. Atmos. Sci.*, **57**, 3689–3702, doi:10.1175/1520-0469(2000)057<3689:ANSOTD>2.0.CO;2.
- Ratnam, M., T. Tsuda, Y. Shibagaki, T. Kozu, and S. Mori, 2006: Gravity wave characteristics over the equator observed during the CPEA campaign using simultaneous data from multiple stations. *J. Meteor. Soc. Japan.*, **84A**, 239–257.
- Salby, M. L. and R. R. Garcia, 1987: Transient response to localized episodic heating in the tropics. Part I: Excitation and short-time near-field behavior. *J. Atmos. Sci.*, **44** (2), 458–498, doi:10.1175/1520-0469(1987)044<0458:TRTLEH>2.0.CO;2.
- Sassi, F. and R. R. Garcia, 1997: The role of equatorial waves forced by convection in the tropical semiannual oscillation. *J. Atmos. Sci.*, **54**, 1925–1942.
- Sato, K. and T. Dunkerton, 1997: Estimate of momentum flux associated with equatorial Kelvin and gravity waves. *J. Geophys. Res.*, **102**, 26 247–26 261.
- Sato, K., T. Kumakura, and M. Takahashi, 1999: Gravity waves appearing in a high-resolution GCM simulation. *J. Atmos. Sci.*, **56** (8), 1005–1018, doi:10.1175/1520-0469(1999)056<1005:GWAI AH>2.0.CO;2.

- Sato, K., M. Yamamori, S. Ogino, N. Takahashi, Y. Tomikawa, and T. Yamanouchi, 2003: A meridional scan of the stratospheric gravity wave field over the ocean in 2001 (MeSSO2001). *J. Geophys. Res.*, **108** (4491), doi:10.1029/2002JD003219.
- Scaife, A. A., N. Butchart, C. D. Warner, D. Stainforth, W. Norton, and J. Austin, 2000: Realistic Quasi-Biennial Oscillations in a simulation of the global climate. *Geophys. Res. Lett.*, **27** (21), 3481–3484.
- Schoeberl, M. R., A. R. Douglass, R. S. Stolarski, S. Pawson, S. E. Strahan, and W. Read, 2008: Comparison of lower stratospheric tropical mean vertical velocities. *J. Geophys. Res.*, **113** (D24109), doi:10.1029/2008JD010221.
- Scinocca, J. F. and N. A. McFarlane, 2004: The variability of modeled tropical precipitation. *J. Atmos. Sci.*, **61**, 1993–2015, doi:10.1175/1520-0469(2004)061<1993:TVOMTP>2.0.CO;2.
- Shibata, K. and M. Deushi, 2005: Partitioning between resolved wave forcing and unresolved gravity wave forcing to the Quasi-Biennial Oscillation as revealed with a coupled chemistry-climate model. *Geophys. Res. Lett.*, **32** (L12820), doi:10.1029/2005GL022885.
- Skamarock, W. C., J. B. Klemp, J. Dudhia, D. O. Gill, D. M. Barker, W. Wang, and J. G. Powers, 2005: A description of the Advanced Research WRF version 2. *Technical Note TN-468+STR*, National Center for Atmospheric Research, Mesoscale and Microscale Meteorology Division.
- Stockwell, R. G., L. Mansinha, and R. P. Lowe, 1996: Localization of the complex spectrum: The S-transform. *IEEE Trans. Sig. Proc.*, **44** (4), 998–1001, doi:10.1109/78.492555.
- Takahashi, M., 1996: Simulation of the stratospheric Quasi-Biennial Oscillation using a general circulation model. *Geophys. Res. Lett.*, **23**(6), 661–664.
- Takahashi, M. and B. A. Boville, 1992: A three-dimensional simulation of the equatorial Quasi-Biennial Oscillation. *J. Atmos. Sci.*, **49**, 1020–1035, doi:10.1175/1520-0469(1992)049<1020:ATDSOT>2.0.CO;2.
- Tindall, J. C., J. Thuburn, and E. J. Highwood, 2006a: Equatorial waves in the lower stratosphere. I: A novel detection method. *Quart. J. Roy. Meteor. Soc.*, **132**, 177–194.
- Tindall, J. C., J. Thuburn, and E. J. Highwood, 2006b: Equatorial waves in the lower stratosphere. II: Annual and interannual variability. *Quart. J. Roy. Meteor. Soc.*, **132**, 195–212.
- Vincent, R. A., S. J. Allen, and S. D. Eckermann, 1997: *Gravity wave parameters in the lower stratosphere, in Gravity Wave Processes: Their parameterization in Global Climate Models*. edited by K. Hamilton, Springer, New York, pp7-25 pp.
- Wada, K., T. Nitta, and K. Sato, 1999: Equatorial inertia-gravity waves in the lower stratosphere revealed by TOGA-COARE IOP data. *J. Meteor. Soc. Japan.*, **77**(3), 721–736.
- Wallace, J. M. and V. E. Kousky, 1968: Observational evidence of Kelvin waves in the tropical stratosphere. *J. Atmos. Sci.*, **25**, 900–907, doi:10.1175/1520-0469(1968)025<0900:OEOKWI>2.0.CO;2.
- Wang, L., M. J. Alexander, T. P. Bui, and M. J. Mahoney, 2006: Small-scale gravity waves in ER-2 MMS/MTP wind and temperature measurements during CRYSTAL-FACE. *Atmos. Chem. Phys.*, **6**, 1091–1104.

- Xie, S., T. Hume, C. Jakob, S. A. Klein, R. B. McCoy, and M. Zhang, 2010: Observed large-scale structures and diabatic heating and drying profiles during TWP-ICE. *J. Climate*, **23** (1), 57–79, doi:10.1175/2009JCLI3071.1.
- Yamamori, M. and K. Sato, 2006: Characteristics of inertia gravity waves over the South Pacific as revealed by radiosonde observations. *J. Geophys. Res.*, **111** (D16110), doi:10.1029/2005JD006861.
- Yanai, M. and T. Maruyama, 1966: Stratospheric wave disturbances propagating in the equatorial Pacific. *J. Meteor. Soc. Japan*, **44**, 291–294.
- Žagar, N., N. Gustafsson, and E. Källén, 2004: Dynamical response of equatorial waves in four-dimensional variational data assimilation. *Tellus A*, **56**, 29–46, doi:10.1029/2004RG000158.